UNIVERSITY OF ROCHESTER
LABORATORY FOR LASER ENERGETICS

Volume 93
October–December 2002
DOE/SF/19460-478

LLE Review

Quarterly Report

About the Cover:

This issue features an article describing the recent implosion performance of direct-drive cryogenic targets on the 60-beam OMEGA laser. Once the target has reached cryogenic temperatures and formed a uniform D_2-ice layer, a high level of coordination is required among Experimental Systems personnel to promptly insert it into the OMEGA target chamber and align it for a laser shot. In the OMEGA Control Room, Senior Technical Associate Jeffrey DeWandel (foreground) and Scientist Douglas Jacobs-Perkins use headsets to communicate with other target alignment personnel operating the auxiliary support equipment. The inset shows the shadowgraph of a surrogate target that was used to significantly improve the alignment accuracy of spherical cryogenic targets, as described in the article beginning on p. 1.

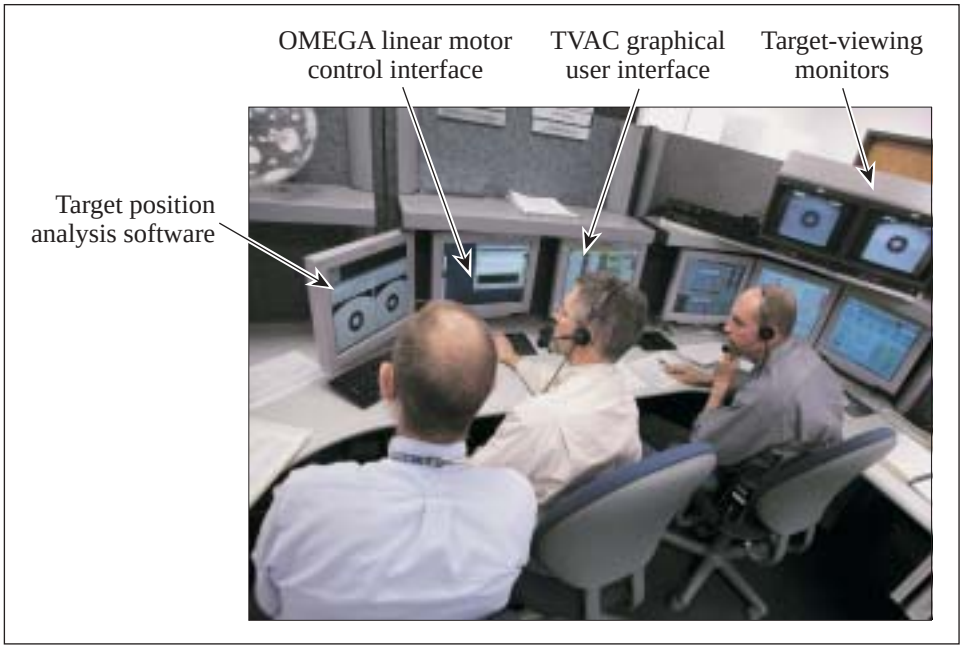

The Experimental Operations Station in the OMEGA Control Room contains computer interfaces to several critical monitoring and position control devices (shown in photo at the left).

This report was prepared as an account of work conducted by the Laboratory for Laser Energetics and sponsored by New York State Energy Research and Development Authority, the University of Rochester, the U.S. Department of Energy, and other agencies. Neither the above named sponsors, nor any of their employees, makes any warranty, expressed or implied, or assumes any legal liability or responsibility for the accuracy, completeness, or usefulness of any information, apparatus, product, or process disclosed, or represents that its use would not infringe privately owned rights. Reference herein to any specific commercial product, process, or service by trade name, mark, manufacturer, or otherwise, does not necessarily constitute or imply its endorsement, recommendation, or favoring by the United States Government or any agency thereof or any other sponsor. Results reported in the LLE Review should not be taken as necessarily final results as they represent active research. The views and opinions of authors expressed herein do not necessarily state or reflect those of any of the above sponsoring entities.

The work described in this volume includes current research at the Laboratory for Laser Energetics, which is supported by New York State Energy Research and Development Authority, the University of Rochester, the U.S. Department of Energy Office of Inertial Confinement Fusion under Cooperative Agreement No. DE-FC03-92SF19460, and other agencies.

Printed in the United States of America
Available from
National Technical Information Services
U.S. Department of Commerce
5285 Port Royal Road
Springfield, VA 22161

Price codes: Printed Copy A04
Microfiche A01

For questions or comments, contact Mark J. Guardalben, *Editor*, Laboratory for Laser Energetics, 250 East River Road, Rochester, NY 14623-1299, (585) 275-3418.

Worldwide-Web Home Page: http://www.lle.rochester.edu/

UNIVERSITY OF ROCHESTER
LABORATORY FOR LASER ENERGETICS

Volume 93
October–December 2002
DOE/SF/19460-478

LLE Review

Quarterly Report

UR LLE

Contents

In Brief iii

Direct-Drive Cryogenic Target Implosion Performance on OMEGA 1

Hydrodynamic Growth of Shell Modulations in the Deceleration Phase of Spherical Direct-Drive Implosions 11

Improved Performance of Direct-Drive ICF Target Designs with Adiabat Shaping Using an Intensity Picket 18

High-Conversion-Efficiency Optical Parametric Chirped-Pulse Amplification System Using Spatiotemporally Shaped Pump Pulses 33

Ultrafast Superconducting Single-Photon Optical Detectors and Their Applications 38

Very Fast Metal–Semiconductor–Metal Ultraviolet Photodiodes on GaN with Submicron Finger Width 46

Glassy Liquid Crystals for Tunable Reflective Coloration 50

High-Resolution Near-Field Raman Microscopy of Single-Walled Carbon Nanotubes 61

Publications and Conference Presentations

In Brief

This volume of the LLE Review, covering October–December 2002, features "Direct-Drive Cryogenic Target Implosion Performance on OMEGA" by T. C. Sangster, J. A. Delettrez, R. Epstein, V. Yu. Glebov, V. N. Goncharov, D. R. Harding, J. P. Knauer, R. L. Keck, J. D. Kilkenny, S. J. Loucks, L. D. Lund, R. L. McCrory, P. W. McKenty, F. J. Marshall, D. D. Meyerhofer, S. F. B. Morse, S. P. Regan, P. B. Radha, S. Roberts, W. Seka, S. Skupsky, V. A. Smalyuk, C. Sorce, J. M. Soures, C. Stoeckl, and K. Thorp, along with J. A. Frenje, C. K. Li, R. D. Petrasso, and F. H. Séguin of MIT, K. A. Fletcher, S. Padalino, and C. Freeman of SUNY Geneseo, and N. Izumi, J. A. Koch, R. A. Lerche, M. J. Moran, T. W. Phillips, and G. J. Schmid of LLNL (p. 1). This article describes progress toward validating the predicted performance of direct-drive capsules that are hydrodynamically equivalent to the baseline direct-drive ignition design for the National Ignition Facility (NIF). These experiments measure the sensitivity of the direct-drive implosion performance to parameters such as the inner-ice-surface roughness, the adiabat of the cryogenic fuel during the implosion, the laser power balance, and the single-beam nonuniformity. These capsules have been imploded using ~17 to 23 kJ of 351-nm laser light with a beam-to-beam rms energy imbalance of less than 5% and full beam smoothing (1-THz bandwidth, 2-D smoothing by spectral dispersion, and polarization smoothing). Near 1-D hydrocode performance has been measured with a high-adiabat drive pulse on a capsule containing a 100-μm-thick layer of D_2 ice, and near 2-D hydrocode performance has been measured on a similar capsule with a low-adiabat drive. Improvements in cryogenic target alignment that will lead to improved implosion symmetry are also described.

Additional highlights of research presented in this issue include the following:

- V. A. Smalyuk, J. A. Delettrez, S. B. Dumanis, V. Yu. Glebov, V. N. Goncharov, J. P. Knauer, F. J. Marshall, D. D. Meyerhofer, P. B. Radha, S. P. Regan, S. Roberts, T. C. Sangster, S. Skupsky, J. M. Soures, C. Stoeckl, R. P. J. Town, and B. Yaakobi along with J. A. Frenje, C. K. Li, R. D. Petrasso, and F. H. Séguin of MIT, D. L. McCrorey and R. C. Mancini of the University of Nevada, Reno, and J. Koch of LLNL (p. 11) describe the growth of inner-surface modulations near peak compression in deuterium–helium 3 (D^3He)-filled spherical targets imploded on OMEGA by using differential imaging of titanium-doped layers placed at various distances from the inner surface of the shell. Time histories of shell temperature and density were measured with titanium *K*-shell absorption spectroscopy, and the shell areal density was estimated using 14.7-MeV D^3He proton spectra. These experiments provide a better quantitative understanding of the evolution of inner-shell modulations that grow due to the Rayleigh–Taylor instability and Bell–Plesset convergence effects in the deceleration phase of a spherical direct-drive implosion.

- V. N. Goncharov, J. P. Knauer, P. W. McKenty, T. C. Sangster, S. Skupsky, R. Betti, R. L. McCrory, and D. D. Meyerhofer (p. 18) present an analytical description of improved target performance in direct-drive implosions using adiabat shaping with a high-intensity picket in front of the main-drive pulse. The picket is used to increase the entropy of only the outer portion of the shell, reducing the growth of hydrodynamic instabilities, while the inner portion of the shell maintains lower entropy to maximize shell compressibility. Experiments have demonstrated an improvement in target yields by a factor of up to 3 for the pulses with the picket compared to the pulses without the picket. Results of the theory and experiments with adiabat shaping are also extended to future OMEGA and NIF cryogenic target designs.

- L. J. Waxer, V. Bagnoud, I. A. Begishev, M. J. Guardalben, J. Puth, and J. D. Zuegel (p. 33) demonstrate a high-conversion-efficiency optical parametric chirped-pulse amplification (OPCPA) system using a spatiotemporally shaped pump pulse to maximize the conversion efficiency of the OPCPA process. Highly stable, 5-mJ pulses have been produced at a 5-Hz repetition rate with 29% overall pump-to-signal conversion efficiency. This system is a test bed for a similar OPCPA design that will be used for injection of a short-pulse, petawatt-class laser.

- R. Sobolewski, A. Verevkin, G. N. Gol'tsman, A. Lipatov, and K. Wilsher (p. 38) present a new class of ultrafast, superconducting single-photon detectors for counting both visible and infrared photons. The detection mechanism is based on photon-induced hotspot formation, which forces supercurrent redistribution and leads to the appearance of a transient resistive barrier across an ultrathin, submicrometer-width, superconducting stripe. Applications for these devices range from noncontact testing of semiconductor CMOS VLSI circuits to free-space quantum cryptography and communications.

- J. Li, W. R. Donaldson, and T. Y. Hsiang (p. 46) measure the temporal response characteristics of fast metal–semiconductor–metal ultraviolet photodiodes fabricated on GaN with finger width and pitch ranging from 0.3 μm to 5 μm. These detectors are attractive because they are relatively easy to fabricate and have no response in the visible region of the spectrum. A temporal response of less than 26 ps at low illumination is reported.

- S. H. Chen, P. H. M. Chen, D. Katsis, and J. C. Mastrangelo (p. 50) describe novel glassy liquid crystals with tunable spectral characteristics that have been developed for photonic applications. The authors also describe the molecular design of photoresponsive systems that combine reversible spectral tunability with superior fatigue resistance and thermal stability.

- A. Hartschuh (LLE), E. J. Sánchez (Portland State University), X. Sunney Xie (Harvard University), and L. Novotny (LLE) (p. 61) present near-field Raman spectroscopy and imaging of single-walled carbon nanotubes (SWNT) with unprecedented spatial resolution of less than 30 nm. This high-resolution capability is applied to resolve local variations in the Raman spectrum along a single SWNT that would be hidden in far-field measurements.

Mark J. Guardalben
Editor

Direct-Drive Cryogenic Target Implosion Performance on OMEGA

Introduction

In the direct-drive inertial confinement fusion (ICF)[1] concept, a spherical capsule containing thermonuclear fuel is imploded by the direct illumination of laser beams focused on the surface of the capsule in a near-uniform pattern. The capsule can also be mounted in a high-Z cavity, generally referred to as a hohlraum, which is then heated by the laser beams, producing a uniform radiation field of x rays. In this indirect-drive ICF concept,[2] the x rays, rather than the laser beams, ablate the outside of the capsule and drive the implosion. While the drive uniformity with x-ray (or indirect) drive may be currently superior to that of direct drive, it is possible to couple a significantly larger fraction of the laser energy into the hydrodynamic motion of the imploding fuel with direct drive. It is possible, therefore, with direct drive to achieve temperatures and densities that are comparable to indirect drive but with considerably less laser energy.

Within a decade or so, implosions of capsules containing cryogenic-DT-fuel layers are expected to ignite and burn at the National Ignition Facility (NIF)[3] currently under construction at the Lawrence Livermore National Laboratory. Independent of the drive scheme, the basic capsule concept for ignition on the NIF is a relatively thick, cryogenic-DT-fuel layer inside a thin, spherical ablator[2] or foam shell.[4] At peak compression, the high areal density (ρR) of the compressed cryogenic DT fuel can support a propagating thermonuclear burn wave due to the local bootstrap heating of the DT alpha-particle energy deposited in the fuel. Although this target concept has been under development for many years, only recently have implosions of appropriately scaled, layered, cryogenic D_2 capsules on the 60-beam, 30-kJ UV OMEGA laser system[5] at the Laboratory for Laser Energetics begun to provide important data for the validation of both direct- and indirect-drive ignition target designs for the NIF.

The OMEGA cryogenic capsules and laser-drive pulses are energy scaled from the direct-drive NIF ignition designs[4,6,7] to provide hydrodynamically equivalent implosions (e.g., matching implosion velocities, hot-spot convergence, and in-flight aspect ratios). The ignition design for the NIF is driven by a 1.5-MJ, high-contrast pulse shape that puts the fuel layer on an adiabat α, of approximately 3 ($\alpha \sim 3$), where α is defined as the ratio of the electron pressure in the shell to the Fermi-degenerate pressure. To achieve hydrodynamic equivalence on OMEGA, the energy absorbed by the capsule per unit mass must be approximately the same as the NIF design. Therefore, the energy scales as the volume of the capsule or (radius^3), the power scales as the surface area of the capsule or (radius^2), and the duration of the drive pulse scales as the capsule radius (the distance to be traveled by the shell). On the 30-kJ OMEGA laser, this leads to a cryogenic capsule radius of approximately 920 μm containing an ice layer that is approximately 100 μm thick.[6]

An analysis[7] of the relative performance of the NIF baseline direct-drive ignition target and the scaled OMEGA cryogenic capsule design using the 2-D hydrocode *ORCHID*[8] has shown that the performance of the two designs can be related using the stability parameter $\bar{\sigma}$, defined as

$$\bar{\sigma}^2 = 0.06 \times \sigma_\ell^2(\ell < 10) + \sigma_\ell^2(\ell \geq 10), \qquad (1)$$

where the σ_ℓ's are the modal rms amplitudes of the perturbations on the inner surface of the ice layer at the end of the acceleration phase. The normalized performance curves plotted as a function of the $\bar{\sigma}$ parameter for the scaled OMEGA (green circles) and the NIF (blue squares) ignition designs are shown in Fig. 93.1 for equivalent $\alpha \sim 3$ implosions. The performance curve for a similarly scaled OMEGA $\alpha \sim 4$ design is also shown (red triangles). Although the smaller OMEGA capsule is more severely disrupted due to the perturbations associated with a given value of $\bar{\sigma}$, the $\alpha \sim 3$ and $\alpha \sim 4$ curves can be used to establish performance requirements for cryogenic implosions on OMEGA that would (computationally) ensure direct-drive ignition on the NIF under equivalent uniformity conditions.

For example, the two dashed lines associated with the NIF $\alpha \sim 3$ and OMEGA $\alpha \sim 4$ curves represent equivalent implo-

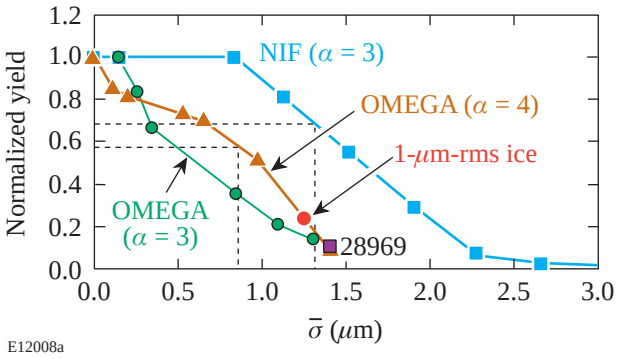

Figure 93.1
Normalized performance curves using the 2-D hydrocode *ORCHID* are shown as a function of the $\bar{\sigma}$ parameter for the scaled OMEGA (green circles) and the NIF (blue squares) ignition designs for equivalent $\alpha \sim 3$ implosions. The performance curve for a scaled OMEGA $\alpha \sim 4$ design is also shown (red triangles). The dashed lines on the $\bar{\sigma}$ axis represent implosions with equivalent uniformity on the NIF and on OMEGA. The point labeled as 28969 is the result of an $\alpha \sim 4$ cryogenic implosion and is discussed in the text. The value of $\bar{\sigma}$ for this implosion is based on a 2-D hydrocode calculation using the known laser and ice-surface nonuniformities, and the measured yield is used to determine the normalized yield. The point labeled as 1-μm-rms ice is based on the calculation for shot 28969 but assumes the NIF ignition specification for the inner-ice-layer-surface roughness.

sion conditions: the uniformity of the laser illumination and the outer and inner surfaces of the capsule are identical. Nonuniformities in the laser illumination and the outer surface of the capsule generate perturbation seeds that grow during the acceleration phase due to the Rayleigh–Taylor (RT) instability.[9,10] These perturbations feed through to the inner ice surface, combine with the original ice perturbations, and continue to grow during the deceleration phase. This phase of the perturbation growth leads to mixing of cryogenic fuel into the hot spot and a subsequent reduction in the performance of the implosion. Therefore, under equivalent uniformity conditions, a normalized yield of 55%–60% on OMEGA ($\alpha \sim 4$) would correspond to achieving a normalized yield of approximately 70% on the NIF ($\alpha \sim 3$). Much of the work on cryogenic implosions on OMEGA is focused on achieving uniformity conditions in both the laser and the surface of the cryogenic fuel that will correspond to ignition conditions expected on the NIF.

To help achieve these conditions, a standard capsule design has been adopted to minimize variations in the fabrication process (filling, layering, and characterization). A standard low-adiabat pulse shape was also adopted for ease of data comparison among implosions with differing levels of inner ice smoothness. The pulse shape was designed to put the cryogenic-fuel shell on an adiabat of approximately 4 (this capsule and drive pulse were used to generate the OMEGA $\alpha \sim 4$ curve shown in Fig. 93.1).

Details of the capsule design and pulse shape are discussed in the next section. The remaining three sections in this article (1) discuss experimental results from two different adiabat implosions and compare them with 1-D and 2-D hydrocode predictions; (2) discuss laser system and Cryogenic Target Handling System (CTHS) improvements that are expected to lead to ignition-equivalent implosions with cryogenic DT capsules in the near future; and (3) present conclusions.

Experimental

1. Cryogenic Target Design

The "standard" cryogenic capsule design and the low-adiabat pulse shape for the experiments reported in this article are shown in Fig. 93.2 along with the NIF direct-drive ignition point design. The shell material is either strong GDP (a high-strength plastic) or CD[11] and is typically 5.0±0.1 μm thick. When permeation filled with approximately 1200 atm of D_2 and then cooled to the triple point (18.73 K), the resulting ice-layer thickness is 100 μm. This shell is somewhat thicker than the capsule designs scaled from the baseline 1.5-MJ ignition design for the NIF and described in Ref. 12. The thicker shell was chosen to increase the laser absorption with the low-adiabat drive pulses (the average atomic number is higher for CH than for the D_2 ice and the thicker CH shell is ablated away later in the drive pulse) and to reduce the length of time required to fill and cool the capsules with D_2 fuel (a thicker shell is more robust). A corresponding thick-plastic-shell (17-μm) ignition design for the NIF has also been developed[13] to take advantage of the higher absorption. By tailoring the adiabat in the shell and fuel, the expected increase in imprint perturbation growth for such a thick shell is substantially reduced. Therefore, the higher absorption and hydrodynamic efficiency lead to improved ignition performance with the additional advantage of the superior mechanical properties of a much thicker shell.

While the relatively low stability of the OMEGA $\alpha \sim 3$ design in Fig. 93.1 would provide enhanced performance sensitivity to nonuniformities for parametric studies and comparison to implosion models, the current levels of laser system nonuniformity would dominate the performance of this capsule design. To enhance the performance margin of cryogenic implosions on OMEGA, a pulse shape was developed that puts the fuel layer of the standard capsule described above at $\alpha \gtrsim 4$. An analysis of the performance of this capsule and pulse

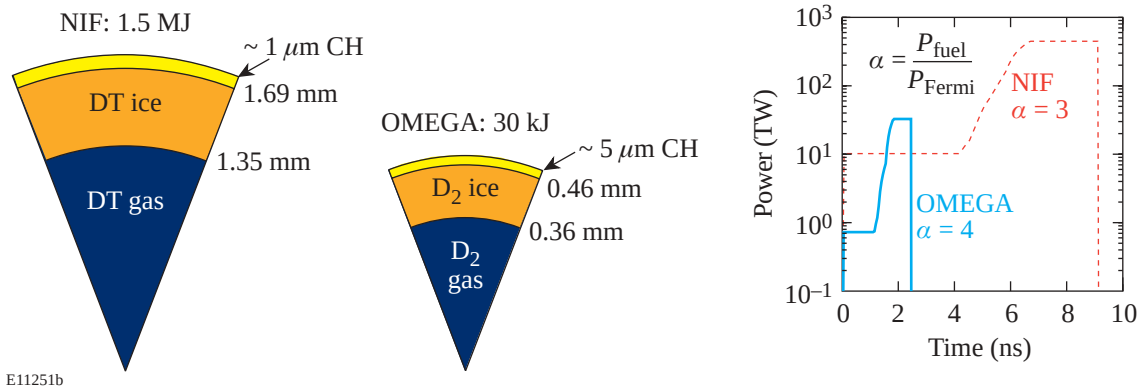

Figure 93.2
The baseline direct-drive ignition design for the NIF is shown along with the energy-scaled, hydrodynamically equivalent cryogenic design imploded on OMEGA and reported in this article. The right-hand panel shows the $\alpha \sim 3$ and $\alpha \sim 4$ pulse shapes for the NIF ignition design and the OMEGA cryogenic implosions, respectively.

shape with a stability postprocessor[14] indicates that the mix width at the end of the acceleration phase is approximately 40%, considerably smaller than the 60% estimated for the scaled $\alpha \sim 3$ OMEGA design. Here the mix width is simply the peak-to-valley of the RT-growth amplitudes, and the ratio of the mix width to the shell thickness is a measure of the shell stability. For equivalent uniformity, the $\alpha \sim 4$ design should perform significantly better than the $\alpha \sim 3$ design. This is demonstrated in Fig. 93.1: the equivalent scaling to ignition performance requires a normalized yield of 55%–60% for this design compared with only 30% for the scaled $\alpha \sim 3$ design. Since an $\alpha \sim 4$ pulse shape applied to the 1.5-MJ NIF baseline direct-drive design still leads to ignition,[4] the OMEGA $\alpha \sim 4$ design described above should be adequate to validate ignition-equivalent performance on OMEGA.

A thorough description of the layering and shadowgraphic characterization of cryogenic capsules is given in Ref. 12. Up to four thin-shell capsules are filled and cooled in the Fill/Transfer Station (FTS) and then individually loaded into moving cryostat transfer carts (MCTC's). These carts contain all of the necessary systems to create, manipulate, and maintain an ice layer inside the plastic capsule. The capsule is located inside a small layering sphere that has four viewing ports and an opening for a laser fiber to deliver up to 150 mW of 3.16-μm IR laser power to the inside surface of the layering sphere. This IR energy is preferentially absorbed in the D_2-ice layer, and low-pressure (~100-mTorr) helium exchange gas conducts heat from the capsule to the layering sphere, which is maintained at approximately 15 K. The settings for the exchange gas pressure, the layering sphere temperature, and the IR laser power control the layering rate of the ice. Thin sapphire windows on the viewing ports provide two orthogonal views of the capsule for shadowgraphic analysis of the layer quality and later alignment at target chamber center for implosion experiments. At shot time, the cryogenic assembly containing the layering sphere (the shroud) is rapidly removed, exposing the capsule, still mounted to the MCTC, to the laser beams. The delay between the shroud removal and laser interaction is approximately 50 ms.

While early 60-beam cryogenic capsule implosions (reported in Ref. 8) were characterized by a single shadowgraphic view,[12] recent improvements to the characterization station permit the capsule to be rotated ±180° to obtain multiple views of the inner-ice-surface quality. Although multiple views do not provide a true three-dimensional picture of the inner ice surface, an average over multiple views does provide a more accurate representation of the modal structure of the ice for 2-D simulations. For most targets, a layer is characterized by at least four views. Techniques are being developed to construct a 3-D representation of the ice layer from multiple (up to 12) 2-D shadowgraphic measurements.

A well-layered capsule is produced in approximately 24 h. Much of this time is spent searching for the triple-point isotherm in the capsule by slowly varying the IR power delivered to the layering sphere while the temperature of the layering sphere and pressure of the exchange gas are held constant. Once the settings for the triple point have been identified, a sub-10-μm-rms layer can usually be formed quickly and the modal structure will slowly anneal with time

(hours). Occasionally, a near-single-crystal layer can be grown, and these capsules generally have very smooth layers (the total rms of modes greater than 3 is about 1 μm). Figure 93.3 shows an example of two near-single-crystal-layer capsules and their multiview-averaged power spectra. Both of these capsules were imploded on the OMEGA laser system.

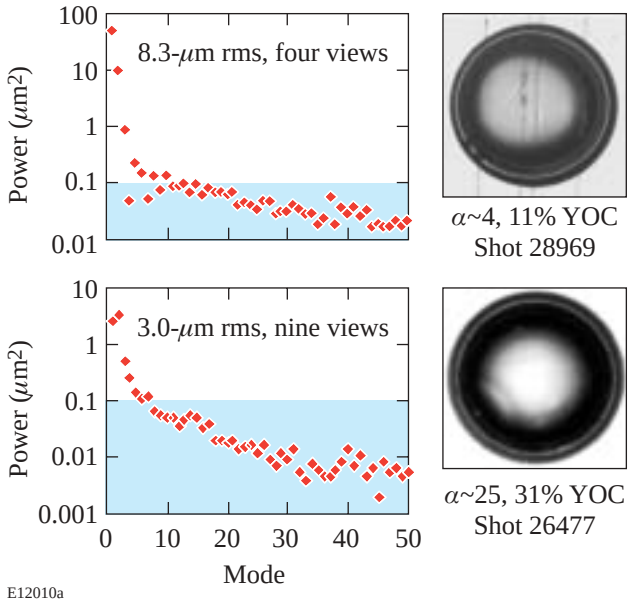

Figure 93.3
Shadowgraphs of two layered and fully characterized cryogenic D_2 capsules prior to being imploded on OMEGA. The average power spectra for the modal structure of the inner ice surface just prior to the implosions are also shown.

2. Laser-Drive Pulses

Cryogenic capsules have been imploded using two pulse shapes: a high-adiabat (α ~ 25), 23-kJ, 1-ns square pulse (~0.5-TW peak intensity) and a low-adiabat (α ~ 4), 17-kJ, 2.5-ns shaped pulse. The α ~ 4 pulse shape is shown in Fig. 93.2. Full single-beam smoothing was applied during all pulses by using distributed phase plates (DPP's),[15] polarization smoothing (PS) with birefringent wedges,[16] and 2-D, single-color-cycle, 1-THz smoothing by spectral dispersion (SSD).[17] Perturbations seeded by single-beam nonuniformities experience RT growth during the acceleration phase, initiated by the arrival of the rarefaction wave (traveling outward from the inner ice surface) at the ablation surface. Since the rarefaction wave does not reach the ablation surface before the end of the high-adiabat pulse (1-ns square), the implosion performance is not particularly sensitive to the acceleration-phase perturbations introduced by laser system imprint (i.e., the acceleration phase is short). The resulting higher performance generally leads to improved diagnostic measurements for comparison to 1-D and 2-D hydrocodes. Implosion performance with the low-adiabat, α ~ 4 pulse is considerably more sensitive to imprint. There is less stabilization during the foot of the pulse (see Fig. 93.2) due to the lower ablation velocity. This leads to greater perturbation amplitudes at the end of the acceleration phase that feed through to the inner ice surface and continue to grow during the deceleration phase.

3. Target Alignment

The cryogenic capsules are suspended on a web of spider silks across a "C"-style mount.[18] The C is designed to avoid intercepting the beams, and the use of spider silk minimizes both mass perturbations on the capsule surface that might affect implosion performance and thermal perturbations that might affect the D_2-ice-layering process. Cryogenic capsule alignment inside the OMEGA target chamber utilizes the Target Viewing System (TVS). Each of the two orthogonal TVS lines of sight views the capsule through six independently mounted sapphire windows. These windows provide the only optical access to the layering sphere through the various thermal barriers. The alignment accuracy of the TVS to target chamber center (TCC) is better than 5 μm for noncryogenic, stalk-mounted targets. The alignment accuracy for cryogenic capsules, however, is limited due to focal blurring through the sapphire windows; for cryogenic capsules, the alignment accuracy is estimated to be approximately 10 μm.

In addition to blurring the capsule images in the TVS, it was found that the target optical offset (the difference between the capsule location viewed through the sapphire windows and the actual location of the capsule) established at room temperature, <5 μm, during the assembly of the MCTC was significantly different once the cryogenic systems were cooled. An analysis of chamber-mounted x-ray pinhole camera (XPHC) images taken during the implosions showed that virtually every cryogenic implosion prior to the identification of a target alignment problem had been offset from TCC by 60 to 120 μm. Using up to five fixed XPHC images on each shot, the magnitude and direction of the capsule offsets were determined with high accuracy. The influence of this offset on the cryogenic implosion performance is presented in the **Discussion** section.

To accurately align cryogenic capsules to TCC, a calibration procedure was developed to generate offset alignment reticles for the TVS. A stalk-mounted surrogate capsule is loaded into the MCTC, the system is cooled to the nominal operating temperature, and the surrogate capsule is inserted

into the target chamber. The capsule is aligned to the TCC using the TVS and then the shroud is removed, exposing the capsule. TVS images of the "bare" capsule are then acquired, and the optical offset caused by the sapphire windows in the shroud is calculated. This offset is then used to generate a unique alignment reticle for each MCTC.

4. Experimental Setup and Diagnostics

The primary diagnostics for cryogenic implosions include the fixed XPHC's mentioned above,[19] x-ray framing cameras,[20] high-resolution Kirkpatrick–Baez (KB) microscopes,[21] primary and secondary neutron yield,[22] secondary proton yield,[23] the ion temperature,[24] and the neutron reaction history.[25] The energy loss of the secondary protons is used to infer the total areal density.[26] The XPHC's provide a low-resolution, time-integrated x-ray image of the capsule shell and core. The framing cameras provide sequential, time-gated core images from just before fusion burn until well after stagnation. These images can be used to assess time-dependent, low-mode asymmetries during the assembly of the core. The high-resolution (~5-μm), time-integrated KB microscopes offer the best images of the core at peak x-ray emission. Asymmetries in the core are related to both laser system nonuniformities and low-mode inner-ice-surface structure. The primary and secondary fusion yields are the most direct measure of the capsule performance and are most sensitive to mix and ion temperature. The reaction history provides crucial validation for hydrocode performance and laser absorption, while the total areal density is perhaps the most important measure of the hydrodynamic performance of the implosion: an areal density of at least 300 mg/cm^2 is required to absorb the full energy of the DT alpha in an ignition target.

Results

As described above, most of the recent cryogenic targets have been significantly offset from TCC at the beginning of the laser pulse. Distributed phase plates (DPP's) on each of the 60 OMEGA beams are used to define the focal-spot distribution of the beams on the target. The minimum spot size of each individual beam is nominally 920 μm, and the intensity distribution is a super-Gaussian of the order of 2.2. Although the effective *f* number of each beam with the DPP is large, the near-Gaussian intensity distribution imposes a large intensity perturbation on the surface of the capsule when the capsule is offset from the nominal best focus of all 60 beams (each of the beams is independently pointed to an alignment surrogate at TCC with an rms deviation of less than 20 μm). This laser-intensity perturbation causes the fuel shell to converge asymmetrically, significantly degrading the performance of the implosion. For example, the peak-to-valley intensity variation on the surface of a 920-μm-diam capsule offset by 50 μm from TCC is approximately ±40% and climbs to nearly ±70% for a 100-μm offset with the standard OMEGA power balance. The effect of this offset on implosion performance is similar to a large $\ell = 1$ mode in the ice (i.e., the ice is thicker on one side of the capsule than on the other; see the capsule shadowgraph of shot 28969 in Fig. 93.3). Not only is the capsule imploded asymmetrically, but the capsule center shifts during the implosion under the influence of the greater pressure generated by the higher laser intensity on the side of the capsule closest to TCC. A higher-order, super-Gaussian, single-beam intensity profile would reduce the effect of an alignment offset and is being pursued in parallel with improvements in the target alignment procedures. Similarly, a larger focal-spot size relative to the target diameter would somewhat mitigate the alignment sensitivity but at the expense of energy loss around the target.

After developing the target alignment procedure described above, several implosions were performed with the capsule less than 25 μm from TCC at the start of the laser pulse. The performance of these implosions can be simulated using the 2-D hydrocode *DRACO*.[27] A comparison will be made between the performance of two cryogenic target implosions (shots 28900 and 28969) and *DRACO* simulations. Shot 28900 imploded a 100-μm-thick D_2-ice layer with a 6.5-μm-rms inner ice layer (pre-shot characterization) using a high-adiabat ($\alpha \sim 25$), 1-ns square pulse with a UV energy on target of 23.3 kJ and an rms energy variation among the 60 OMEGA beams of 2.9%. Shot 28969 imploded a 100-μm-thick D_2-ice layer with an 8.3-μm-rms inner ice layer dominated by the $\ell = 1$ component (see Fig. 93.3 and the modal spectrum for this capsule); the measured rms energy variation of the beams was 3.4% and the low-adiabat $\alpha \sim 4$ pulse shape delivered 16.6 kJ to the target. Analysis of the PHC data showed that both capsules were offset from TCC by less than 20 μm at the beginning of the laser pulse. Although the effect of this small offset on the implosion performance is not negligible (especially for the low-adiabat drive pulse), it does not dominate the performance. The 2-D *DRACO* simulations neglect the offset, and the predicted performance is based entirely on the laser system power balance and the quality of the inner surface of the ice layer.

Figures 93.4 and 93.5 show the 2-D *DRACO* predictions for the fuel-density contours [panel (a)] and a polar lineout of the total areal density [panel (b)] for the two implosions. It is immediately apparent that both cores have been offset by the

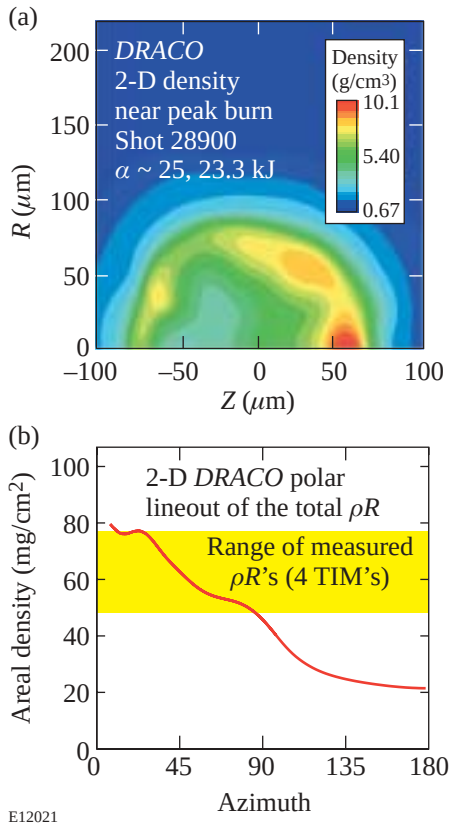

Figure 93.4
(a) A plot of the fuel-density contours at peak burn for shot 28900 ($\alpha \sim 25$, 23.3 kJ) from the 2-D hydrocode *DRACO*. (b) Polar lineout of the total areal density from the center of the core derived from the density contours shown in (a). The yellow region shows the range of the individual areal-density measurements inferred from the average energy loss of secondary protons.

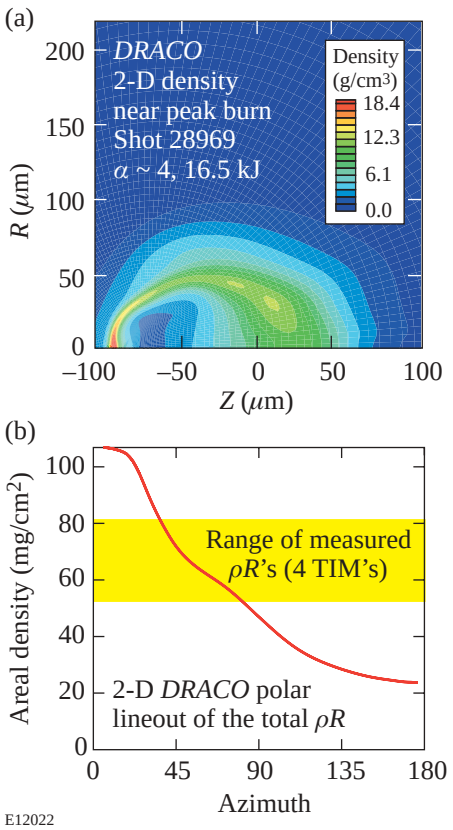

Figure 93.5
(a) A plot of the fuel-density contours at peak burn for shot 28969 ($\alpha \sim 4$, 16.5 kJ) from the 2-D hydrocode *DRACO*. (b) Polar lineout of the total areal density from the center of the core derived from the density contours shown in (a). The yellow region shows the range of the individual areal-density measurements inferred from the average energy loss of the secondary protons.

influence of the low-mode nonuniformity of the ice layers. The effect of the large $\ell = 1$ mode on the inner ice surface in shot 28969 is especially apparent in Fig. 93.5(a). The core offsets lead to a significant asymmetry in the predicted areal density. The areal densities predicted by the 2-D simulations agree well with the measured values, which fall within the yellow regions in Figs. 93.4(b) and 93.5(b). It is not currently possible to correlate the polar angles of the areal-density lineouts from either shot with the orientation of the experimental measurements. However, the roughly factor-of-5 variation in the 2-D areal density for shot 28969 (and the factor-of-4 variation for shot 28900) is consistent with some of the experimental variations measured on other implosions in which the capsule was significantly offset from TCC. The extreme values of areal density are not likely to be observed on most shots with only a limited number of individual measurements (typically four per shot) available.

Table 93.I gives a comparison between experimentally measured or inferred quantities and the 1-D *LILAC*[28] and 2-D *DRACO* predictions. The 1-D yield from shot 28900 ($\alpha \sim 25$) is considerably higher than the 2-D *DRACO* yield (57% of the 1-D value) and virtually identical to the measured yield. This suggests that the at-shot state of the capsule may have been different from the pre-shot characterization used in the 1-D and 2-D hydrocodes. Assuming that the temperature of the capsule might have changed prior to the shot (evidence for this is discussed in the following section), a series of 1-D *LILAC* calculations were performed in which the temperature of the capsule was varied above and below the nominal value from the pre-shot characterization (typically 100 mK below the triple point). These simulations did not provide a satisfactory explanation for the high performance of the capsule relative to the 2-D predictions (the yield was nearly a factor of 4 higher than any previous $\alpha \sim 25$ implosion with ~100 μm of ice; the

Table 93.I: A comparison of the experimental measurements with the 1-D and 2-D hydrocode predictions. The hydrocode predictions are given as the ratio of the experimental measurement to the predicted value (in percent).

Measurement	Shot 28900	Experimental/ 1-D *LILAC* (%)	Experimental/ 2-D *DRACO* (%)	Shot 28969	Experimental/ 1-D *LILAC* (%)	Experimental/ 2-D *DRACO* (%)
Primary neutron yield	1.27×10^{11}	96	171	5.95×10^{9}	11	112
Secondary neutron yield	1.17×10^{9}	84	132	6.75×10^{7}	9.7	107
Secondary proton yield	2.03×10^{8}	112		7.14×10^{6}	11	
$<\rho R>$ mg/cm^2	61	133	120	67.00	84	115
T_{ion} (keV)	3.6	157	139	2.5	145	125
Y_{2n}/Y_{1n}	0.0092	85	77	0.0113	91	95
Y_{2p}/Y_{1p}	0.0016	114		0.0012	104	
Offset (μm)	14			11		

primary difference from previous shots is the small TCC offset). A further series of calculations were performed in which the flux limiter[29] was increased from 0.060 to 0.068. This increased the 1-D yield by a factor of 2, lowering the yield-over-clean (YOC) to approximately 50% and bringing the predicted neutron bang time into agreement with the measured value. A similar treatment within *DRACO* would have a comparable result and bring the 2-D yield prediction into agreement with the experimental measurement. While a higher value of the flux limiter for this shot is suggested by the bang-time measurement, a change in the flux limiter is not supported by recent absorption measurements on CH at OMEGA. In contrast to shot 28900, the 2-D yield for shot 28969 ($\alpha \sim 4$) is in very good agreement with the experimental measurement. Both are approximately 10% of the 1-D yield. Indeed, all of the 2-D predictions are reasonably close to the experimental measurements for this shot. This is a very encouraging result given the large amplitude of the low-mode nonuniformity on the inner ice surface layer.

Figure 93.6 shows the primary neutron YOC and the average total areal density as a function of the measured capsule offset and the pre-shot characterization of the D_2 inner-ice-surface rms for all of the cryogenic implosions to date in which the ice layer appears to have been intact at shot time. Based on the analysis shown in Fig. 93.1, the primary yield is expected to increase with increasing smoothness of the inner ice layer [Fig. 93.6(a)]. For most of the shots, the influence of the ice-surface perturbations on the implosion performance is obscured by the gross low-mode nonuniformity caused by the capsule offset [Fig. 93.6(b)]. With no capsule characterization in the target chamber prior to the shot, there is also uncertainty in the inner-ice-surface roughness at shot time. In Fig. 93.6(b), there is evidence with the high-adiabat implosions that the capsule performance is significantly degraded due to the capsule offset. As expected, the average total areal density for the high-adiabat implosions does not appear to depend on the ice-layer quality [Fig. 93.6(c)]; however, there appears to be a correlation for increasing total areal density with decreasing ice roughness for the low-adiabat ($\alpha \sim 4$) implosions, where the convergence ratio at stagnation is expected to be somewhat larger. As a function of decreasing capsule offset from TCC, there is a general trend of increasing areal density for both the low- and high-adiabat implosions [Fig. 93.6(d)]. This also correlates with the observation that the asymmetry in the individual areal-density measurements (the spread divided by the mean) decreases with decreasing target offset.

The measured ion temperatures in all of the cryogenic implosions exceed the 1-D hydrocode predictions. In the absence of a significant shock yield (there is no evidence for a shock yield from the neutron temporal diagnostic), this is usually understood as a phenomenon associated with the mixing of cold fuel into the hot spot. The measured yield preferentially samples the small hot-spot volume, which is surrounded by a steep, mix-induced temperature gradient. The yield from this mix region is considerably less than the ratio of the fuel

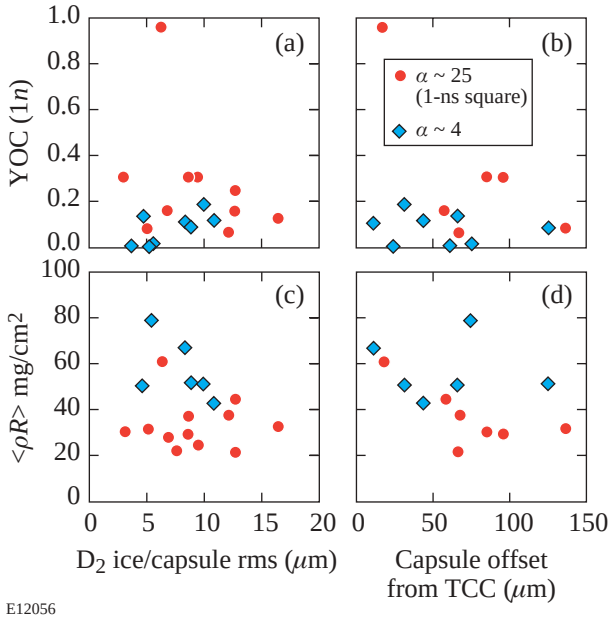

Figure 93.6
(a) The ratio of the primary neutron yield to the predicted yield from the 1-D hydrocode *LILAC* [the yield-over-clean (YOC)] as a function of the pre-shot D_2-ice roughness. (b) The same YOC values plotted as a function of the capsule offset from TCC [for some of the points shown in panel (a), the offset was not measured] at the start of the laser pulse. (c) The average areal density as a function of the pre-shot D_2-ice roughness. Increasing areal density appears to be correlated with a reduction in the inner-ice-surface roughness for the low-adiabat implosions. Such a correlation does not exist for the high-adiabat implosions that are expected to be much less sensitive to laser imprint and acceleration-phase perturbation growth. (d) The average areal density as a function of the capsule offset from TCC. For both low- and high-adiabat implosions, the areal density increases with decreasing capsule offset.

volumes (hot spot and mix regions). However, the large offsets and uncertainties in the layer quality at shot time make it difficult to interpret the ion temperature data. For example, the average ion temperature measured for implosions where other experimental evidence (e.g., reaction histories and core images) suggests that the ice layer was compromised prior to the shot is 4.4 keV and only 2.7 keV for implosions in which the experimental evidence suggests an intact layer. In Table 93.I, the measured ion temperatures for the two implosions suggest some degree of mix when compared with the hydrocode predictions.

Finally, secondary proton production in shots 28900 and 28969 indicate a hot-spot areal density between 10 and 12 mg/cm^2 according to the uniform density model of Azechi and Cable.[30] The hot-spot areal density inferred from shot 28900 ($\alpha \sim 25$) is somewhat larger than that inferred for the lower-adiabat implosion. These hot-spot areal densities are about a factor of 2 larger than those reported in Ref. 12 and are at or near the saturation limit of the model for the measured ion temperatures.

Discussion

The rms amplitudes of the inner-ice-surface roughness at the end of the acceleration phase in the 2-D *DRACO* simulation of shot 28969 ($\alpha \sim 4$) can be used to calculate the value of the $\bar{\sigma}$ parameter used by McKenty[7] to define the scaling performance of cryogenic implosions on OMEGA and the NIF. This point falls very close to the OMEGA $\alpha \sim 4$ curve in Fig. 93.1 and should be compared with the point labeled as 1-μm-rms ice. The 1-μm-rms ice point represents an identical 2-D simulation (i.e., current laser system nonuniformity on OMEGA) assuming the NIF specification for ice smoothness (total rms of 1 μm). This comparison clearly shows that scaled ignition performance on OMEGA will require improvements in the OMEGA laser system uniformity as well as improvements to the inner-ice-layer smoothness. Achieving ignition-equivalent performance on OMEGA (e.g., a normalized 2-D yield of approximately 60%) will require a laser system nonuniformity of 1% or less and an rms inner-ice-surface roughness of approximately 1 μm.

Although outstanding inner-ice-layer smoothness has been achieved (approximately 3-μm rms including contributions from the thin plastic shell; see also Fig. 93.2), the stability of the IR laser used to layer the D_2 ice and the fiber-optic transport used to deliver IR power to the layering sphere does not appear to be adequate to produce and maintain high-surface-quality layers (sub-3-μm rms). An IR power feedback control system based on the measured power into the layering sphere is currently being implemented to establish the triple point to the required accuracy (a high-quality layer requires single-crystal growth within approximately 1 mK of the triple point). The goal of the feedback system is to regulate the power in the layering sphere to 0.1%.

As described in the previous section, improvements to the laser system uniformity include the development of new distributed phase plates (DPP's) with tight tolerances on spot size, ellipticity, and order; new techniques for enhanced power balance[31] and target alignment; and new specifications for beam pointing. Based on measurements of the prototype DPP, an analysis of the potential improvements to the overall laser system nonuniformity suggests that the requirement for <1% rms will be achieved in the near future. Low-adiabat drive pulses that include a picket to tailor the adiabat across the

cryogenic fuel shell are expected to significantly reduce the imprint and subsequent growth rates from single-beam nonuniformities.[13] By tailoring the adiabat with a picket pulse, the ablation velocity can be increased without significantly raising the internal pressure of the capsule. This helps to minimize the growth of imprint perturbations during the acceleration phase. A future study of cryogenic capsule performance with and without these pickets is one of the highest priorities within the direct-drive program at LLE.

Conclusions

The performance of hydrodynamically scaled cryogenic ignition capsules with both low- and high-adiabat pulse shapes has been reported. The primary goal of these experiments is to demonstrate equivalent direct-drive ignition performance using pulse shapes and capsule designs scaled from the baseline ignition design for the NIF. Near 1-D hydrocode performance has been measured with a high-adiabat ($\alpha \sim 25$) drive pulse on a capsule containing a 100-μm-thick layer of cryogenic D_2, and near 2-D hydrocode performance has been measured on a similar capsule with a low-adiabat ($\alpha \sim 4$) drive. The fabrication and the characterization of layered cryogenic capsules with inner-ice-surface roughness of between 3- and 12-μm rms are now routine (see Fig. 93.3). A new cryogenic target characterization diagnostic is under development to provide a single view of the inner ice surface within 50 ms of the shot. A feedback system is being developed to stabilize the IR laser power in the layering sphere. These upgrades will significantly improve implosion performance in future cryogenic experiments. Additionally, improvements to the overall laser system uniformity are being pursued. These include the development of a new distributed phase plate with a high-order super-Gaussian intensity profile and much tighter tolerances on plate-to-plate spot size and ellipticity. These new DPP's will immediately reduce the overall laser system power imbalance. Coupled with more-accurate UV energy transport measurements and tighter tolerances on beam pointing, the overall laser system nonuniformity should approach 1% rms. With this level of laser system uniformity and continued improvements in the inner-ice-surface smoothness, it will be possible to validate the performance of direct-drive ignition capsule designs on OMEGA.

ACKNOWLEDGMENT

The authors are grateful to the staff of the Laboratory for Laser Energetics for their tireless dedication to the cryogenic implosion program and the operation of the OMEGA laser system. In particular, the authors would like to acknowledge the efforts of the Cryogenic Target Fabrication Group for the production of layered and characterized capsules on a regular schedule. This work was supported by the U. S. Department of Energy Office of Inertial Confinement Fusion under Cooperative Agreement No. DE-FC03-92SF19460, the University of Rochester, and the New York State Energy Research and Development Authority. The support of DOE does not constitute an endorsement by DOE of the views expressed in this article.

REFERENCES

1. J. Nuckolls *et al.*, Nature **239**, 139 (1972).
2. J. D. Lindl, *Inertial Confinement Fusion: The Quest for Ignition and Energy Gain Using Indirect Drive* (Springer-Verlag, New York, 1998).
3. W. J. Hogan, E. I. Moses, B. E. Warner, M. S. Sorem, and J. M. Soures, Nucl. Fusion **41**, 567 (2001).
4. S. E. Bodner, D. G. Colombant, J. H. Gardner, R. H. Lehmberg, S. P. Obenschain, L. Phillips, A. J. Schmitt, J. D. Sethian, R. L. McCrory, W. Seka, C. P. Verdon, J. P. Knauer, B. B. Afeyan, and H. T. Powell, Phys. Plasmas **5**, 1901 (1998).
5. T. R. Boehly, D. L. Brown, R. S. Craxton, R. L. Keck, J. P. Knauer, J. H. Kelly, T. J. Kessler, S. A. Kumpan, S. J. Loucks, S. A. Letzring, F. J. Marshall, R. L. McCrory, S. F. B. Morse, W. Seka, J. M. Soures, and C. P. Verdon, Opt. Commun. **133**, 495 (1997).
6. Laboratory for Laser Energetics LLE Review **79**, 121, NTIS document No. DOE/SF/19460-317 (1999). Copies may be obtained from the National Technical Information Service, Springfield, VA 22161.
7. P. W. McKenty, V. N. Goncharov, R. P. J. Town, S. Skupsky, R. Betti, and R. L. McCrory, Phys. Plasmas **8**, 2315 (2001).
8. R. L. McCrory and C. P. Verdon, in *Inertial Confinement Fusion*, edited by A. Caruso and E. Sindoni (Editrice Compositori, Bologna, Italy, 1989), pp. 83–124.
9. Lord Rayleigh, Proc. London Math Soc. **XIV**, 170 (1883).
10. G. Taylor, Proc. R. Soc. London Ser. A **201**, 192 (1950).
11. A. Nikroo *et al.*, Fusion Sci. Technol. **41**, 214 (2002).
12. C. Stoeckl, C. Chiritescu, J. A. Delettrez, R. Epstein, V. Yu. Glebov, D. R. Harding, R. L. Keck, S. J. Loucks, L. D. Lund, R. L. McCrory, P. W. McKenty, F. J. Marshall, D. D. Meyerhofer, S. F. B. Morse, S. P. Regan, P. B. Radha, S. Roberts, T. C. Sangster, W. Seka, S. Skupsky, V. A. Smalyuk, C. Sorce, J. M. Soures, R. P. J. Town, J. A. Frenje, C. K. Li, R. D. Petrasso, F. H. Séguin, K. Fletcher, S. Padalino, C. Freeman, N. Izumi, R. Lerche, and T. W. Phillips, Phys. Plasmas **9**, 2195 (2002).
13. V. N. Goncharov, "Improved Performance of Direct-Drive ICF Target Designs with Adiabat Shaping Using an Intensity Picket," to be published in Physics of Plasmas; see also this issue of the LLE Review, p. 18.
14. V. N. Goncharov, P. McKenty, S. Skupsky, R. Betti, R. L. McCrory, and C. Cherfils-Clérouin, Phys. Plasmas **7**, 5118 (2000).
15. T. J. Kessler, Y. Lin, J. J. Armstrong, and B. Velazquez, in *Laser Coherence Control: Technology and Applications*, edited by H. T. Powell and T. J. Kessler (SPIE, Bellingham, WA, 1993), Vol. 1870, pp. 95–104.

16. T. R. Boehly, V. A. Smalyuk, D. D. Meyerhofer, J. P. Knauer, D. K. Bradley, R. S. Craxton, M. J. Guardalben, S. Skupsky, and T. J. Kessler, J. Appl. Phys. **85**, 3444 (1999).

17. S. Skupsky, R. W. Short, T. Kessler, R. S. Craxton, S. Letzring, and J. M. Soures, J. Appl. Phys. **66**, 3456 (1989).

18. Laboratory for Laser Energetics LLE Review **81**, 21, NTIS document No. DOE/SF/19460-335 (1999). Copies may be obtained from the National Technical Information Service, Springfield, VA 22161.

19. F. J. Marshall, T. Ohki, D. McInnis, Z. Ninkov, and J. Carbone, Rev. Sci. Instrum. **72**, 713 (2001).

20. D. K. Bradley *et al.*, Rev. Sci. Instrum. **66**, 716 (1995).

21. F. J. Marshall and J. A. Oertel, Rev. Sci. Instrum. **68**, 735 (1997); F. J. Marshall, M. M. Allen, J. P. Knauer, J. A. Oertel, and T. Archuleta, Phys. Plasmas **5**, 1118 (1998).

22. V. Yu. Glebov, D. D. Meyerhofer, C. Stoeckl, and J. D. Zuegel, Rev. Sci. Instrum. **72**, 824 (2001); M. D. Cable and M. B. Nelson, Rev. Sci. Instrum. **59**, 1738 (1988).

23. F. H. Séguin, C. K. Li, D. G. Hicks, J. A. Frenje, K. M. Green, R. D. Petrasso, J. M. Soures, D. D. Meyerhofer, V. Yu. Glebov, C. Stoeckl, P. B. Radha, S. Roberts, C. Sorce, T. C. Sangster, M. D. Cable, S. Padalino, and K. Fletcher, Phys. Plasmas **9**, 2725 (2002).

24. T. J. Murphy, R. E. Chrien, and K. A. Klare, Rev. Sci. Instrum. **68**, 610 (1997); R. A. Lerche *et al.*, Appl. Phys. Lett. **31**, 645 (1977).

25. C. Stoeckl, V. Yu. Glebov, S. Roberts, T. C. Sangster, R. A. Lerche, R. L. Griffith, and C. Sorce, to be published in the Review of Scientific Instruments; see also Laboratory for Laser Energetics LLE Review **92**, 156, NTIS document No. DOE/SF/19460-465 (2002). Copies may be obtained from the National Technical Information Service, Springfield, VA 22161.

26. F. H. Séguin, C. K. Li, J. A. Frenje, S. Kurebayashi, R. D. Petrasso, F. J. Marshall, D. D. Meyerhofer, J. M. Soures, T. C. Sangster, C. Stoeckl, J. A. Delettrez, P. B. Radha, V. A. Smalyuk, and S. Roberts, Phys. Plasmas **9**, 3558 (2002).

27. P. B. Radha, V. N. Goncharov, T. J. B. Collins, J. A. Delettrez, and P. W. McKenty, "Multidimensional Effects in Plastic Shell Implosions on the OMEGA Laser," to be submitted to Physics of Plasmas.

28. M. C. Richardson, P. W. McKenty, F. J. Marshall, C. P. Verdon, J. M. Soures, R. L. McCrory, O. Barnouin, R. S. Craxton, J. Delettrez, R. L. Hutchison, P. A. Jaanimagi, R. Keck, T. Kessler, H. Kim, S. A. Letzring, D. M. Roback, W. Seka, S. Skupsky, B. Yaakobi, S. M. Lane, and S. Prussin, in *Laser Interaction and Related Plasma Phenomena*, edited by H. Hora and G. H. Miley (Plenum Publishing, New York, 1986), Vol. 7, pp. 421–448.

29. R. C. Malone, R. L. McCrory, and R. L. Morse, Phys. Rev. Lett. **34**, 721 (1975).

30. H. Azechi, M. D. Cable, and R. O. Stapf, Laser Part. Beams **9**, 119 (1991); M. D. Cable and S. P. Hatchett, J. Appl. Phys. **62**, 2233 (1987).

31. Laboratory for Laser Energetics LLE Review **91**, 116, NTIS document No. DOE/SF/19460-458 (2002). Copies may be obtained from the National Technical Information Service, Springfield, VA 22161.

Hydrodynamic Growth of Shell Modulations in the Deceleration Phase of Spherical Direct-Drive Implosions

Introduction

The goal of inertial confinement fusion (ICF)[1,2] is to implode a spherical target to achieve fuel densities and temperatures adequate to sustain thermonuclear burn. In a spherical implosion the target is driven either by direct illumination with laser beams (direct drive)[1] or by x rays produced in a high-Z enclosure (hohlraum) containing the target (x-ray drive).[2] The unstable growth of target nonuniformities is the most significant factor disrupting the symmetry of implosions, reducing the target compression and fusion yield.[2] A direct-drive implosion begins with an acceleration phase when the laser beams ablate the shell surface directly and the capsule starts to converge. At this stage, outer-shell nonuniformities, both existing imperfections in the shell surface and imprinted due to nonuniformities in the laser drive, grow due to the acceleration-phase Rayleigh–Taylor (RT) instability.[3–16] As the shell accelerates, these front-surface perturbations feed through the shell, seeding perturbations on the inner surface. After the laser is turned off, the ablation front becomes stable and the shell starts to decelerate while continuing to converge. At stagnation, the shell stops (peak compression) and then rebounds. During the deceleration phase, the inner surface of the shell is subject to RT instability.[17–22] In addition, the modulations grow due to Bell–Plesset (BP) convergent effects[23] throughout the compression.

Experimentally, the hydrodynamic growth of target perturbations has been extensively studied using both x-ray[2–7] and direct[8–16] drive mostly in planar geometry. Both classical[3–5] and ablative[3–5,8–10] RT-instability linear growth rates have been measured using single-mode perturbations. Multimode[6,7] and broadband[16] perturbations were used to measure nonlinear saturation[24–26] and mode-coupling effects. The highly nonlinear, turbulent mixing regime of the RT-instability relevant to ICF conditions has been studied using planar geometry.[27–31] Experiments in both cylindrical[32,33] and spherical geometries[34,35] were used to measure acceleration-phase hydrodynamic growth including BP convergent effects. Small-scale mix of the highly nonlinear classical RT instability has been inferred in both x-ray[36,37] and direct-drive[38–40] spherical implosions. The deceleration-phase RT growth has been measured in spherical implosions using shell radiography by the x rays coming from the hot core emitted near peak compression.[41–43] This article presents the status of deceleration-phase hydrodynamic growth measurements and discusses future experiments.

Experimental Conditions

The modulation evolution measurements are based on differential imaging[41–43] of shells with diagnostic titanium-doped layers. Near peak compression of a spherical target implosion, when the maximum density and temperature occur, the hot, compressed core and inner surface of the shell produce strong x-ray emission. This emission can be used as a backlighter to probe the outer, colder shell. The experiments use shells with titanium-doped layers and imaging at photon energies above and below the titanium K edge. Core images at photon energies below the K edge (not absorbed by the shell) provide the spatial shape of the backlighter, while core images at photon energies above the K edge (highly absorbed by the shell's titanium) contain information about the structure of shell-areal-density modulations in the titanium-doped layer. The modulations in the cold, or absorbing, part of the shell areal density $\delta[\rho d](\mathbf{r},t)$ at time t ($\mathbf{r}$ is the spatial coordinate) are proportional to the modulation in the logarithm of the ratio of intensities of the two images at photon energies above (highly absorbing by the shell) and below (weakly absorbing by the shell) the titanium K edge.[41–43]

Figure 93.7(a) shows a schematic of a spherical target and the position of the diagnostic titanium layer used in these experiments. The targets with ~450-μm initial radii and 20-μm-thick shells, filled with 4 or 18 atm of D^3He gas, were imploded by 351-nm laser light using the 60-beam OMEGA laser system[44] with a 1-ns square pulse shape at a total energy of ~23 kJ. All shots were taken with laser beams smoothed by distributed phase plates (DPP's);[45] 1-THz, two-dimensional smoothing by spectral dispersion (2-D SSD);[46] and polarization smoothing (PS)[47] using birefringent wedges. The average beam-to-beam energy imbalance was ~3% in all

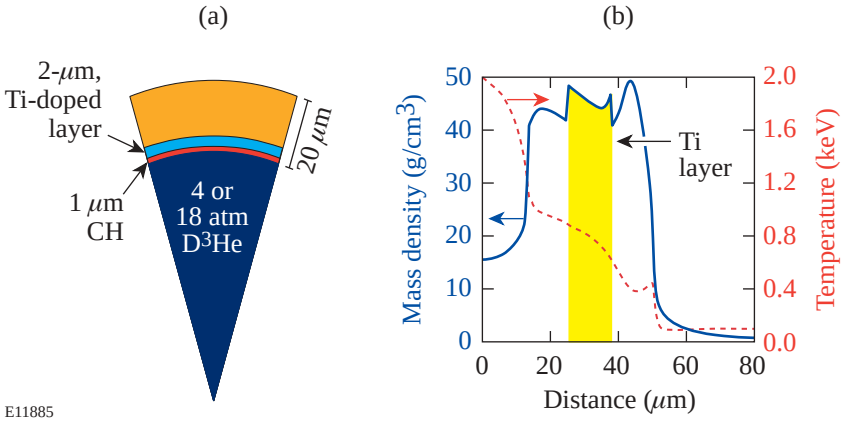

Figure 93.7
Schematic of spherical targets: (a) a 20-μm-thick shell filled with 4 or 18 atm of D^3He gas. (b) Simulated profiles of target density (solid line) and temperature (dashed line) at peak compression for the 18-atm target. The position of a diagnostic titanium-doped layer is shown by the yellow region.

implosions. Targets with 20-μm-thick shells filled with 4 or 18 atm of D^3He gas exhibit similar behavior during their laser-driven acceleration phases and therefore have similar perturbations at the beginning of the deceleration phase. Because of their differing gas-fill pressures (4 or 18 atm), these targets experience different deceleration-phase growth near peak compression.

The ~2-μm-thick, titanium-doped (~6% by atom) CH layers were offset from the inner surface by ~1 μm of pure CH. These layers were expected to be located at the unstable RT interface near peak compression. Figure 93.7(b) shows the temperature and density profiles of one of the targets [shown in Fig. 93.7(a)] with a 20-μm-thick shell filled with 18 atm of gas, calculated at peak compression by the 1-D code *LILAC*.[48] The diagnostic titanium layer (shown by the yellow region) is located on the slope of the density profile of the inner shell, where the unstable surface is located. The measured evolution of titanium-doped layer uniformity around peak compression is used to quantify the deceleration RT growth in these implosions.

The areal-density modulations in the titanium layer have been measured with differential imaging[41–43,49,50] using a framing camera. Simultaneously, the spectral evolution of core emission was captured on an x-ray streak camera. The relative areal-density modulations $\delta[\rho d]/\rho d$ in the titanium-doped layers—a measure of the shell integrity—have been obtained by normalizing the framing camera images of areal-density modulations $\delta[\rho d](\mathbf{r},t)$ to the average areal density $[\rho d](t)$ measured with the streak camera. Figure 93.8 presents images of measured areal-density modulations $\delta[\rho d](\mathbf{r},t)$ for a shot with a 20-μm-thick shell and 4 atm of D^3He fill around peak compression. The average titanium areal density $[\rho d](t)$ is not an accurate measure of compression in the layer because the amount of titanium atoms and ions available for absorption can be modified by the rapidly changing core radiation and the increasing temperature in the shell around peak compression. The shell integrity $\delta[\rho d]/\rho d$ is not affected by these effects; however, an understanding of the implosion hydrodynamics requires measurements of shell-areal-density evolution along with that of the modulations.

The temporal history of the shell areal density has been inferred[51] from the spectra of primary protons from the D^3He fusion reaction and the evolution of the primary neutrons from the simultaneous DD reaction. The emitted primary 14.7-MeV, D^3He protons are slowed down by the relatively low-density fuel and the high-density shell while exiting the target. The time-integrated proton energy spectrum contains information about the target-areal-density evolution. When the measured proton energy spectrum is coupled with the neutron production history, the areal-density evolution can be inferred during the time of particle production.[51] Figure 93.9 shows the inferred temporal history of total target areal density (thick blue line) compared to a 1-D *LILAC* prediction (thin black line) in the shot with a 20-μm-thick shell and 4 atm of D^3He fill. The

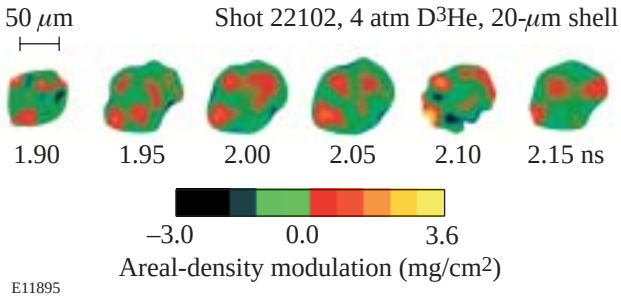

Figure 93.8
Images of areal-density modulations for a target with a 20-μm-thick shell filled with 4 atm of D^3He gas taken at times 1.90, 1.95, 2.00, 2.05, 2.10, and 2.15 ns.

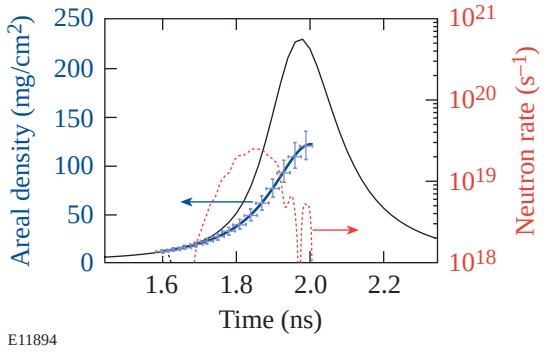

Figure 93.9
Inferred (thick blue line) and simulated (thin black line) target-areal-density evolutions for a 4-atm implosion. The measured (dotted line) neutron production history for the 4-atm implosion is from Ref. 51.

neutron-production history is shown by the dotted line for comparison. The total target areal density shown in Fig. 93.9 consists of the shell areal density (about 90% to 95%) and the gas fuel areal density (about 5% to 10%). The target (and shell) areal density grows by a factor of ~1.5 from the time of peak neutron production at ~1.9 ns to the time of peak compression at ~2.0 ns. This growth will be used below to estimate the BP contribution in the total modulation growth.

Experimental Results

Figure 93.10 shows the modulation growth inferred for two shots with 20-μm-thick shells and 4 atm of D^3He fill around peak compression. The σ_{rms} of the relative areal-density modulations $\delta[\rho d]/\rho d$ grows by a factor of ~10 during the ~200 ps around peak compression. The modulation levels are ~20% at peak neutron production (~1.9 ns) and ~50% at peak compression (~2.0 ns). Figure 93.11 shows a comparison of the nonuniformity spectra taken at peak compression for targets with 20-μm-thick shells filled with 18 atm and 4 atm of D^3He, respectively. These targets exhibit similar behavior during their laser-driven acceleration phases and therefore have similar perturbations at the beginning of the deceleration phase. Because of the different gas-fill pressures (4 or 18 atm), however, these targets experience different deceleration growths near peak compression. The power per mode of relative modulation levels $\delta[\rho d]/\rho d$ as a function of spatial frequency is shown in Fig. 93.11(a) for the more-stable 18-atm and in Fig. 93.11(b) for the more-unstable 4-atm-D^3He fills. The measured areal-density modulation levels are 23±5% and 53±11% for shots with 18-atm- and 4-atm-D^3He fills, respectively. In both spectra, measured perturbations have the highest amplitudes at spatial frequencies of about 20 to 25 mm^{-1} corresponding to spatial wavelengths of 40 to 50 μm (or a mode number of $\ell \sim 6$), with the smallest detectable features having wavelengths of about 15 to 20 μm.

Discussion

The shell's inner-surface modulations grow due to the RT instability during the deceleration phase since the higher-density shell is slowed down by the lower-density gas of the

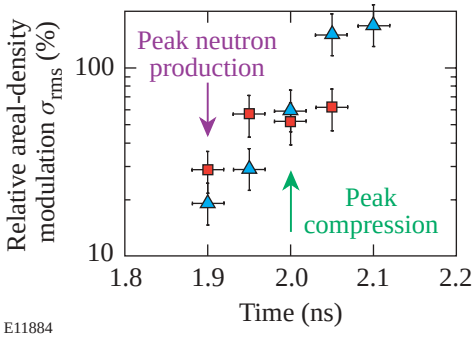

Figure 93.10
The evolution of inner-shell relative areal-density modulation σ_{rms} as a function of time for two shots [shown by triangles (shot 22102) and squares (shot 22103)] with 20-μm-thick shells filled with 4 atm of D^3He gas.

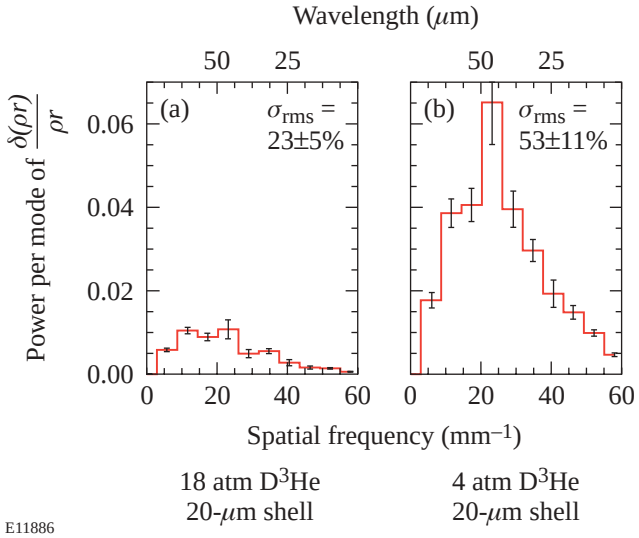

Figure 93.11
Power-per-mode spectra of relative areal-density modulations as a function of spatial frequency for 20-μm-thick shells filled with (a) 18 atm and (b) 4 atm of D^3He gas taken at peak compression and averaged over two or three shots per condition.

target core.[25–30] Unlike the acceleration-phase RT instability, where the outer-surface modulation growth is stabilized by mass ablation, the deceleration-phase RT instability is classical, with no ablative stabilization for these targets. In the linear regime of the classical RT instability, the modulation amplitude δr_1 for mode number ℓ [$\ell = kR$, where k is a modulation wave number and $R(t)$ is the radius, or position of the unstable surface] grows exponentially in time:[2]

$$\delta r_1 = \delta r_0 \exp\left[\sqrt{A_T(\ell/R)gt^2}\right], \tag{1}$$

where A_T is the Atwood number, δr_0 is the initial perturbation amplitude, g is the deceleration, and t is time. The characteristic of the classical RT instability is the rapid growth of short-scale perturbation that quickly enters the highly nonlinear regime causing shell-density perturbations $\delta\rho$ in addition to shell-amplitude perturbations δr and shell–fuel mix. The growth of longer-wavelength perturbations can be modified by the presence of mix because the mix increases the core pressure by supplying additional material into the core. As a result, the deceleration g increases and the Atwood number A_T decreases, modifying the shell trajectory and the modulation growth.

The other factor contributing to perturbation growth is Bell–Plesset (BP) convergent effects. As the shell converges from radius R_0 (with thickness d_0 and density ρ_0) to radius R_1 (with thickness d_1 and density ρ_1), the shell modulation δr_1 grows due to BP effects[23] as

$$\delta r_1 = \delta r_0 \left(\rho_0 R_0^2\right)\Big/\left(\rho_1 R_1^2\right) = \delta r_0 d_1/d_0 .$$

The shell modulation due to BP growth is proportional to shell thickness: $\delta r \sim d$. Note that the modulation growth of shell integrity, $\delta[\rho d]/\rho d$ does not explicitly include BP effects {$\delta[\rho d]/\rho d$ due to BP effects is constant because $\delta(\rho d) \sim (\rho d)$}; however, the convergent effects constantly modify the RT instability, which is responsible for the modulation growth.

Figure 93.12 presents schematically a physical picture of the implosions to explain the experimental data. One-dimensional *LILAC* predictions of the implosion trajectories with 4 (thin) and 18 atm (thick) of D^3He are shown in Fig. 93.12(a). The solid lines show the trajectories of the shell–fuel interfaces, $R(t) = R_0 - vt + gt^2/2$, for both implosions, and the dashed lines show the free-fall trajectories of these interfaces,

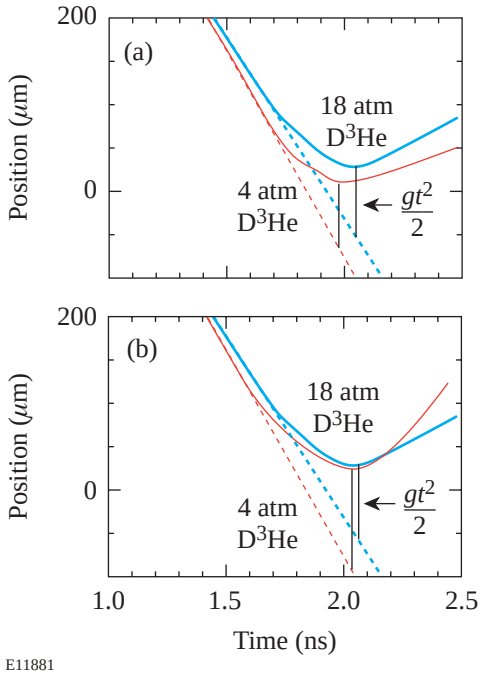

Figure 93.12
(a) *LILAC*-simulated inner-surface trajectories (solid lines) and free-fall trajectories (dashed lines) as a function of time for 20-μm-thick shells filled with 18 atm (thick) and 4 atm (thin) of D^3He gas. (b) The same trajectories as inferred from the experimental data.

$R_{ff}(t) = R_0 - vt$, where R_0 is the radius and v is the velocity of the inner-shell surface at the beginning of the deceleration phase. The shell velocity v is higher in the 4-atm implosion compared to the 18-atm implosion because the pressure difference between the shell and the gas is higher in the 4-atm case. The RT-growth rate of the unstable modulations in the deceleration phase of the implosion are related to the difference between inner surface and free-fall trajectories, $R(t) - R_{ff}(t) = gt^2/2$. For any mode number ℓ, the growth factor is higher in an implosion with a 4-atm fill compared to an 18-atm fill of D^3He because the $R(t)$ is smaller in the 4-atm implosion, and factors $gt^2/2$ are similar for both implosions at peak compression. In the experiment the expected trajectory for an 18-atm implosion is close to the 1-D *LILAC* prediction because the measured evolution of target areal density is close to 1-D. In the 4-atm implosion, however, the measured target-areal-density evolution is much lower than the 1-D prediction (as shown in Fig. 93.9) and only about 10% higher than for the 18-atm implosion.[51] The trajectories inferred from the experimental observations are shown schematically in Fig. 93.12(b) for both implosions. At peak compression the trajectories $R(t)$ are similar but the factor $gt^2/2$ is higher in the implosion with a 4-atm fill than in the 18-atm case. The

higher fuel–shell mix is responsible for the higher deceleration in the 4-atm implosion because the core pressure is increased by the addition of shell material from the mix.[38–40,52]

In the experiments, the relative areal-density modulations with spatial wavelengths ranging from about 15 to 60 μm, $\delta[\rho d]/\rho d$, grow by a factor of ~2.5 during the ~100 ps from peak neutron production (~1.9 ns) to peak compression (~2.0 ns) in the 4-atm implosion (see Fig. 93.10). The shell areal density [ρd] grows by a factor of 1.5 for the same period (see Fig. 93.9) due to the growth of both the density ρ and the thickness d; therefore, the shell modulations ($\delta r \sim d$) should grow by up to a factor of 1.5 due to BP convergent effects. The BP effects do not contribute directly to the growth of shell integrity, $\delta[\rho d]/\rho d$ therefore, the measured growth of relative areal-density modulation should be entirely due to the RT instability. In addition, the modulation growth modifies the shell trajectories leading to lower compression than predicted by 1-D in the more-unstable 4-atm implosion. At peak compression, the measured areal-density modulation levels are 23±5% and 53±11% for shots with 18-atm- and 4-atm-D^3He fills, respectively.

Future Experiments

The RT instability and BP growth are defined by the growth of amplitude modulations δr. In future experiments it will be necessary to measure the evolution of density along with average areal density and areal-density modulations in the titanium-doped layers to infer the evolution of amplitude modulations δr from the relative areal-density modulations $\delta[\rho d]/\rho d$. The x-ray spectrum in the titanium 1s–2p absorption region is sensitive to the density, areal density, and temperature of the layer. The time-resolved titanium absorption spectroscopy will provide the required information to better understand the unstable growth. In addition, the absorption in the titanium 1s–2p spectral region is higher by a factor of ~10 than in the region above the titanium K edge; therefore, differential imaging of shell modulations using 1s–2p absorption will be more sensitive than the results presented here.

As an example, preliminary, time-integrated shell-integrity experiments[53] based on titanium 1s–2p absorption were conducted with 20-μm-thick plastic CH shells filled with 18 atm of D^3He gas. The diagnostic was a 1-μm-thick, titanium-doped (~2% by atom) CH layer offset from the inner surface by ~1, 5, 7, or 9 μm of pure CH. These layers infer the shell-areal-density modulations at the inner, central, and outer parts of the shell at peak compression. Figure 93.13(a) shows the temperature and density profiles at peak compression of a representative target calculated by the 1-D code *LILAC*. At peak compression, the diagnostic titanium layer offset by 1 μm is located on the slope of the density profile at the inner shell, where the unstable surface is located. Titanium layers offset by 5 μm and 7 μm sample the central part of the shell, and the layer offset by 9 μm represents the outer part of the shell at peak compression.

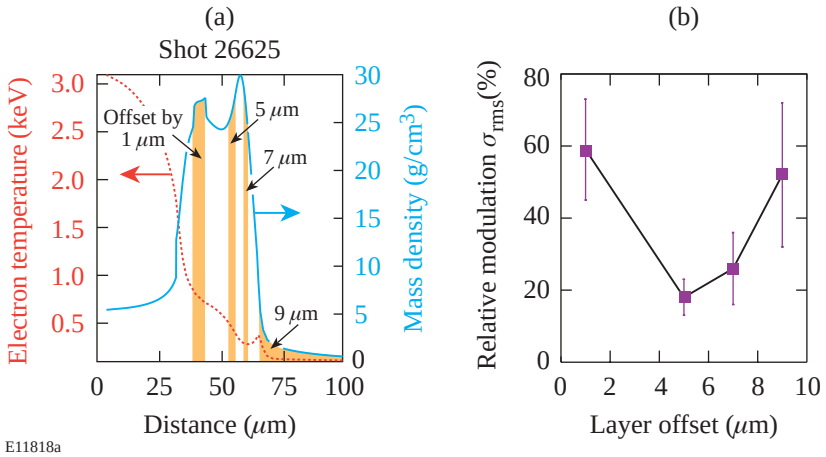

Figure 93.13
(a) *LILAC*-simulated profiles of target density and temperature at peak compression for the implosion of a 20-μm-thick shell filled with 18 atm of D^3He gas. The locations of titanium-doped (2% by atom) layers offset by 1, 5, 7, and 9 μm of pure CH from the inner surface are shown by the gold areas. (b) Peak-compression, relative areal-density modulation σ_{rms} as a function of the layer offset.

At peak compression, time-integrated areal-density modulations were measured using the ratios of monochromatic core images taken inside and outside of the titanium 1*s*–2*p* absorption spectral region. The relative areal-density modulation $\sigma_{\rm rms}$ was 59±14%, 18±5%, 26±10%, and 52±20% in the layers offset by 1, 5, 7, and 9 μm, respectively, as shown in Fig. 93.13(b). The modulations are highest at the inner surface (in the 1-μm-offset layer), which is unstable during the deceleration phase of the implosion near peak compression. As expected, the modulations decrease in the bulk of the shell (in the 5- and 7-μm-offset layers) but then increase at the outer surface (in the 9-μm-offset layer), which is unstable during the acceleration phase of the implosion. Time-resolved experiments based on differential imaging using the titanium 1*s*–2*p* absorption region will be conducted to study the evolution of shell nonuniformities in different parts of the shell.

As discussed in the previous section, the modulation growth of longer spatial wavelengths is modified by the presence of fuel–shell mix, which comes from the growth of shorter spatial wavelengths in the highly nonlinear phase of the classical deceleration-phase RT instability. Direct measurements of mix evolution are essential not only to quantify the short-wavelength RT growth but also to explain the observed reduction of shell compression and the modification of the longer-wavelength RT growth.

Conclusions

Shell modulation growth has been measured on targets with titanium-doped layers using differential imaging near peak compression of spherical implosions with 20-μm-thick plastic CH shells filled with 4 atm of D^3He gas. The measured perturbations have the highest amplitudes at spatial wavelengths of about 40 to 50 μm (corresponding to a mode number $\ell \sim 6$), with the shortest detectable features corresponding to wavelengths of about 15 to 20 μm. At peak neutron production, the relative areal-density modulation level $\delta[\rho d]/\rho d$ is ~20% and grows to ~50% at peak compression 100 ps later due to RT instability. For the same time period, the shell modulations grow up to about 1.5 times due to BP convergent effects. At peak compression the inner part of the shell has a higher modulation level than the bulk of the shell.

ACKNOWLEDGMENT

This work was supported by the U.S. Department of Energy Office of Inertial Confinement Fusion under Cooperative Agreement No. DE-FC03-92SF19460, the University of Rochester, and the New York State Energy Research and Development Authority. The support of DOE does not constitute an endorsement by DOE of the views expressed in this article.

REFERENCES

1. J. Nuckolls *et al.*, Nature **239**, 139 (1972).
2. J. D. Lindl, *Inertial Confinement Fusion: The Quest for Ignition and Energy Gain Using Indirect Drive* (Springer-Verlag, New York, 1998), Chap. 6, pp. 61–82.
3. S. G. Glendinning, S. N. Dixit, B. A. Hammel, D. H. Kalantar, M. H. Key, J. D. Kilkenny, J. P. Knauer, D. M. Pennington, B. A. Remington, R. J. Wallace, and S. V. Weber, Phys. Rev. Lett. **78**, 3318 (1997).
4. K. S. Budil *et al.* Phys. Rev. Lett. **76**, 4536 (1996).
5. K. S. Budil *et al.*, Phys. Plasmas **8**, 2344 (2001).
6. B. A. Remington *et al.*, Phys. Rev. Lett. **73**, 545 (1994).
7. M. M. Marinak *et al.*, Phys. Rev. Lett. **80**, 4426 (1998).
8. J. Grun *et al.*, Phys. Rev. Lett. **58**, 2672 (1987).
9. K. Shigemori *et al.*, Phys. Rev. Lett. **78**, 250 (1997).
10. J. P. Knauer, R. Betti, D. K. Bradley, T. R. Boehly, T. J. B. Collins, V. N. Goncharov, P. W. McKenty, D. D. Meyerhofer, V. A. Smalyuk, C. P. Verdon, S. G. Glendinning, D. H. Kalantar, and R. G. Watt, Phys. Plasmas **7**, 338 (2000).
11. R. J. Taylor *et al.*, Phys. Rev. Lett. **76**, 1643 (1996).
12. D. H. Kalantar, M. H. Key, L. B. Da Silva, S. G. Glendinning, B. A. Remington, J. E. Rothenberg, F. Weber, S. V. Weber, E. Wolfrum, N. S. Kim, D. Neely, J. Zhang, J. S. Wark, A. Demir, J. Lin, R. Smith, G. J. Tallents, C. L. S. Lewis, A. MacPhee, J. Warwick, and J. P. Knauer, Phys. Plasmas **4**, 1985 (1997).
13. H. Azechi *et al.*, Phys. Plasmas **4**, 4079 (1997).
14. C. J. Pawley *et al.*, Phys. Plasmas **6**, 565 (1999).
15. T. R. Boehly, V. N. Goncharov, O. Gotchev, J. P. Knauer, D. D. Meyerhofer, D. Oron, S. P. Regan, Y. Srebro, W. Seka, D. Shvarts, S. Skupsky, and V. A. Smalyuk, Phys. Plasmas **8**, 2331 (2001).
16. V. A. Smalyuk, T. R. Boehly, D. K. Bradley, V. N. Goncharov, J. A. Delettrez, J. P. Knauer, D. D. Meyerhofer, D. Oron, and D. Shvarts, Phys. Rev. Lett. **81**, 5342 (1998).
17. H. Sakagami and K. Nishihara, Phys. Rev. Lett. **65**, 432 (1990).
18. R. P. J. Town and A. R. Bell, Phys. Rev. Lett. **67**, 1863 (1991).
19. M. M. Marinak *et al.*, Phys. Plasmas **3**, 2070 (1996).
20. V. Lobatchev and R. Betti, Phys. Rev. Lett. **85**, 4522 (2000).
21. M. C. Herrmann, M. Tabak, and J. D. Lindl, Phys. Plasmas **8**, 2296 (2001).
22. R. Betti, K. Anderson, V. N. Goncharov, R. L. McCrory, D. D. Meyerhofer, S. Skupsky, and R. P. J. Town, Phys. Plasmas **9**, 2277 (2002).

23. M. S. Plesset and T. P. Mitchell, Q. Appl. Math. **13**, 419 (1956).

24. S. W. Haan, Phys. Rev. A **39**, 5812 (1989).

25. S. W. Haan, Phys. Fluids B **3**, 2349 (1991).

26. M. J. Dunning and S. W. Haan, Phys. Plasmas **2**, 1669 (1995).

27. D. L. Youngs, Physica D **37**, 270 (1989).

28. K. I. Read, Physica **12D**, 45 (1984).

29. G. Dimonte and M. Schneider, Phys. Rev. E **54**, 3740 (1996).

30. G. Dimonte, Phys. Plasmas **6**, 2009 (1999).

31. M. B. Schneider, G. Dimonte, and B. Remington, Phys. Rev. Lett. **80**, 3507 (1998).

32. W. W. Hsing *et al.*, Phys. Plasmas **4**, 1832 (1997).

33. D. L. Tubbs, C. W. Barnes, J. B. Beck, N. M. Hoffman, J. A. Oertel, R. G. Watt, T. Boehly, D. Bradley, P. Jaanimagi, and J. Knauer, Phys. Plasmas **6**, 2095 (1999).

34. C. Cherfils *et al.*, Phys. Rev. Lett. **83**, 5507 (1999).

35. S. G. Glendinning *et al.*, Phys. Plasmas **7**, 2033 (2000).

36. T. R. Dittrich *et al.*, Phys. Rev. Lett. **73**, 2324 (1994).

37. M. D. Cable *et al.*, Phys. Rev. Lett. **73**, 2316 (1994).

38. D. D. Meyerhofer, J. A. Delettrez, R. Epstein, V. Yu. Glebov, V. N. Goncharov, R. L. Keck, R. L. McCrory, P. W. McKenty, F. J. Marshall, P. B. Radha, S. P. Regan, S. Roberts, W. Seka, S. Skupsky, V. A. Smalyuk, C. Sorce, C. Stoeckl, J. M. Soures, R. P. J. Town, B. Yaakobi, J. D. Zuegel, J. Frenje, C. K. Li, R. D. Petrasso, D. G. Hicks, F. H. Séguin, K. Fletcher, S. Padalino, M. R. Freeman, N. Izumi, R. Lerche, T. W. Phillips, and T. C. Sangster, Phys. Plasmas **8**, 2251 (2001).

39. P. B. Radha, J. Delettrez, R. Epstein, V. Yu. Glebov, R. Keck, R. L. McCrory, P. McKenty, D. D. Meyerhofer, F. Marshall, S. P. Regan, S. Roberts, T. C. Sangster, W. Seka, S. Skupsky, V. Smalyuk, C. Sorce, C. Stoeckl, J. Soures, R. P. J. Town, B. Yaakobi, J. Frenje, C. K. Li, R. Petrasso, F. Séguin, K. Fletcher, S. Padalino, C. Freeman, N. Izumi, R. Lerche, and T. W. Phillips, Phys. Plasmas **9**, 2208 (2002).

40. S. P. Regan, J. A. Delettrez, F. J. Marshall, J. M. Soures, V. A. Smalyuk, B. Yaakobi, V. Yu. Glebov, P. A. Jaanimagi, D. D. Meyerhofer, P. B. Radha, W. Seka, S. Skupsky, C. Stoeckl, R. P. J. Town, D. A. Haynes, Jr., I. E. Golovkin, C. F. Hooper, Jr., J. A. Frenje, C. K. Li, R. D. Petrasso, and F. H. Séguin, Phys. Rev. Lett. **89**, 085003 (2002).

41. B. Yaakobi, V. A. Smalyuk, J. A. Delettrez, F. J. Marshall, D. D. Meyerhofer, and W. Seka, Phys. Plasmas **7**, 3727 (2000).

42. V. A. Smalyuk, V. N. Goncharov, J. A. Delettrez, F. J. Marshall, D. D. Meyerhofer, S. P. Regan, and B. Yaakobi, Phys. Rev. Lett. **87**, 155002 (2001).

43. V. A. Smalyuk, J. A. Delettrez, V. N. Goncharov, F. J. Marshall, D. D. Meyerhofer, S. P. Regan, T. C. Sangster, R. P. J. Town, and B. Yaakobi, Phys. Plasmas **9**, 2738 (2002).

44. T. R. Boehly, D. L. Brown, R. S. Craxton, R. L. Keck, J. P. Knauer, J. H. Kelly, T. J. Kessler, S. A. Kumpan, S. J. Loucks, S. A. Letzring, F. J. Marshall, R. L. McCrory, S. F. B. Morse, W. Seka, J. M. Soures, and C. P. Verdon, Opt. Commun. **133**, 495 (1997).

45. Y. Lin, T. J. Kessler, and G. N. Lawrence, Opt. Lett. **20**, 764 (1995).

46. S. P. Regan, J. A. Marozas, J. H. Kelly, T. R. Boehly, W. R. Donaldson, P. A. Jaanimagi, R. L. Keck, T. J. Kessler, D. D. Meyerhofer, W. Seka, S. Skupsky, and V. A. Smalyuk, J. Opt. Soc. Am. B **17**, 1483 (2000).

47. T. R. Boehly, V. A. Smalyuk, D. D. Meyerhofer, J. P. Knauer, D. K. Bradley, R. S. Craxton, M. J. Guardalben, S. Skupsky, and T. J. Kessler, J. Appl. Phys. **85**, 3444 (1999).

48. J. Delettrez, R. Epstein, M. C. Richardson, P. A. Jaanimagi, and B. L. Henke, Phys. Rev. A **36**, 3926 (1987).

49. V. A. Smalyuk, T. R. Boehly, L. S. Iwan, T. J. Kessler, J. P. Knauer, F. J. Marshall, D. D. Meyerhofer, C. Stoeckl, B. Yaakobi, and D. K. Bradley, Rev. Sci. Instrum. **72**, 635 (2001).

50. V. A. Smalyuk, B. Yaakobi, J. A. Delettrez, F. J. Marshall, and D. D. Meyerhofer, Phys. Plasmas **8**, 2872 (2001).

51. V. A. Smalyuk, P. B. Radha, J. A. Delettrez, V. Yu. Glebov, V. N. Goncharov, D. D. Meyerhofer, S. P. Regan, S. Roberts, T. C. Sangster, J. M. Soures, C. Stoeckl, J. A. Frenje, C. K. Li, R. D. Petrasso, and F. H. Séguin, "Time-Resolved Areal-Density Measurements with Proton Spectroscopy in Spherical Implosions," to be published in Physical Review Letters.

52. C. K. Li, F. H. Séguin, J. A. Frenje, S. Kurebayashi, R. D. Petrasso, D. D. Meyerhofer, J. M. Soures, J. A. Delettrez, V. Yu. Glebov, P. B. Radha, F. J. Marshall, S. P. Regan, S. Roberts, T. C. Sangster, and C. Stoeckl, Phys. Rev. Lett. **89**, 165002 (2002).

53. V. A. Smalyuk, S. B. Dumanis, F. J. Marshall, J. A. Delettrez, D. D. Meyerhofer, S. P. Regan, T. C. Sangster, B. Yaakobi, and J. A. Koch, to be published in Physics of Plasmas.

Improved Performance of Direct-Drive ICF Target Designs with Adiabat Shaping Using an Intensity Picket

Introduction

Hydrodynamic instabilities put severe constraints on target designs for inertial confinement fusion (ICF) experiments.[1,2] A large number of papers published over the last 30 years have been dedicated to the study of the seeding and subsequent growth of the hydrodynamic instabilities that develop during the shell implosion.[3] A particularly large effort (both theoretical and experimental) has been directed to understanding the growth rate of the dominant hydrodynamic instability—the Rayleigh–Taylor (RT) instability.[4] The RT instability inevitably occurs in systems where the heavier fluid is accelerated by the lighter fluid. Such conditions arise during the shell compression in ICF implosions, where the heavier shell material is accelerated by the lighter blowoff plasma.[1] The RT-instability growth amplifies the shell distortions seeded by initial surface roughness and laser nonuniformities (laser "imprint"). Grown to substantial amplitudes, the shell nonuniformities reduce the shell ρR and the neutron yield. Fortunately for ICF implosions, the thermal conduction that drives the ablation process creates several stabilizing effects that reduce both the nonuniformity seeding and the RT-growth rates.[3] Indeed, seeding due to the laser nonuniformity is determined by how quickly the plasma atmosphere is created around the imploding shell. The laser radiation is absorbed at some distance from the cold shell. The larger this distance (the conduction zone), the larger the smoothing effect[5] of the thermal conductivity within the conduction zone and the smaller the laser imprint. The stabilization of the RT modes is also due to the thermal conductivity that drives the mass ablation of the shell material. The ablation process is characterized by the ablation velocity V_a, which is defined as the ratio of the mass ablation rate to the shell density, $V_a = \dot{m}/\rho_{\mathrm{sh}}$. The larger the value of the ablation velocity, the larger the ablative stabilization.[3] Taking thermal smoothing and ablative stabilization into account, one can make a general statement that the higher the initial intensity of the drive laser pulse, the smaller the nonuniformities and the more stable the implosion. Indeed, the higher intensity tends to create the conduction zone in shorter time, reducing the laser imprint. In addition, the initial shock launched by the higher-intensity pulse is stronger, resulting in larger shock preheat. This reduces the shell density, increasing the ablation velocity. Furthermore, a lower density leads to an increase in the shell thickness and a reduction in the perturbation feedthrough from the ablation front to the shell's rear surface (which becomes unstable during the deceleration phase of the implosion). There is a price to pay, however, for the greater stability. As the stronger shock propagates through the shell, it increases the shell entropy. A parameter (commonly used in the ICF community[1,2]) that characterizes the shell entropy during the implosion is the shell adiabat α. The adiabat is defined as the ratio of the shell pressure to the Fermi-degenerate pressure calculated at the shell density. Since the shell compressibility is reduced by an increase in the adiabat, the final compression ratio and the target neutron yield are also reduced. A common practice in designing direct-drive targets is to find the delicate balance between reduction in the target performance due to an increase in the adiabat and the increase in shell stability.

In optimizing the target design, one can take into consideration that the RT modes are surface modes peaked at the ablation surface of the shell. Therefore, to reduce the instability growth, it is sufficient to raise the adiabat only at the outer region of the shell, which ablates during the implosion. If the inner portion of the shell is kept on a lower adiabat, the shell and vapor compressibility will not be reduced during the final stage of implosion, and the neutron yields will be unaffected by this selective adiabat increase (adiabat shaping). New direct-drive designs proposed in the current work use adiabat shaping to improve the performance of the imploding shells. The idea of adiabat shaping using radiation preheat has already been implemented in an ignition target presented in Ref. 2. The designs described in this article use a different approach. The shell adiabat is shaped by launching a shock whose strength decreases as it propagates through the shell. This places an adiabat gradient directed toward the ablation front. Time variation in the shock strength is imposed by using an intensity picket in front of the main-drive pulse. The picket launches a strong shock that propagates through the shell. As the laser intensity drops at the end of the picket, the shocked material starts to expand and a rarefaction wave is launched toward

the shock. After the rarefaction and the shock coalesce, the shock strength decays, reducing the adiabat of the shock-compressed material.

The picket pulse shapes for the direct-drive (DD) ignition target designs were first proposed in Ref. 6. The main motivation for such pulses was to replace a continuous shell acceleration with an impulsive acceleration. The impulsive acceleration leads to a linear-in-time growth, replacing the exponential RT growth.

It would be premature, however, to make a conclusion about the shell stability based only on an analysis of the ablation velocity. A careful account of all additional sources of the perturbation growth prior to and during the shell acceleration is required. The analysis reported in this article reveals that introducing an adiabat gradient creates conditions for an additional instability. In the shaped-adiabat designs, the gradient in the entropy has the same sign as the effective acceleration, which excites the convective instability.[7] It is well known,[7] however, that the convective instability modes are internal modes (the eigenmode maximum is localized inside the shell), and the instability growth rates are lower than those of the classical RT instability. Although our analytical calculations and numerical simulations show that such an instability makes no significant contribution to the overall shell nonuniformity balance in the designs described here, care must be taken to control the seeding and the growth of the internal convective modes. In addition, the analysis reveals an "early time" RT growth (prior to the acceleration RT growth) at the ablator/main fuel interface during the transitional phase between the picket and the main drive pulse. Such a growth leads to a modification in the mode structure prior to the acceleration phase.

This article identifies the main advantages and possible disadvantages in using adiabat shaping in ICF target designs. The following sections (1) derive a time history of the material flow in a decaying shock configuration; (2) describe new DD designs for the OMEGA[8] and the National Ignition Facility's[9] laser systems and present the results of stability analysis of such designs; and (3) summarize the results of the experiments performed with the shaped-adiabat warm plastic targets.[10]

Propagation of a Decaying Shock

As described in the **Introduction**, new target designs are proposed using an intensity picket to shape the adiabat inside the shell. In this section we determine the adiabat profile by solving a simplified problem of shock propagation in the case of an impulsive applied pressure. We assume that a finite pressure p_p is applied during a time interval $0 < t < t_p$. At $t > t_p$ the applied pressure goes to zero. During the picket duration, a strong shock is launched into the shell. As the external pressure goes to zero, the shocked material starts to expand, launching a rarefaction wave in the direction of the initial shock. At $t = t_p + t_{rw}$ the rarefaction wave catches up with the shock, and the shock strength starts to decay. Therefore, by the time the shock breaks out at the rear surface, the adiabat at the shell's rear surface will be lower than the adiabat at the front surface. The problem of shock propagation in the case of the impulsive load has been considered previously,[11,12] and the solution was obtained using a self-similar analysis.[11] Such an analysis, however, is only valid asymptotically ($t >> t_p$). Since there is a finite decrease in the entropy prior to the time when the solutions of Ref. 11 become valid, the self-similar treatment cannot predict the total entropy variation across the shell, so we must use a different approach to determine the adiabat profile.

Assuming that in the laboratory frame of reference the shock moves in the negative x direction with the velocity $U_s = \sqrt{(\gamma+1)p_s/(2\rho_0)}$, the hydrodynamic conservation equations can be combined to determine the time evolution of the pressure p_s at the shock front:

$$\frac{dp_s}{dt} = \frac{\gamma-1}{2\gamma-1} U_s \left(\partial_x p\right)_s, \tag{1}$$

where γ is the ratio of specific heats and ρ_0 is the initial shell density. In writing Eq. (1) we used a strong-shock limit $p_s/p_0 >> 1$, where p_0 is the initial shell pressure. Next, we must calculate the pressure gradient at the shock front. We accomplish this by considering a physically equivalent problem: instead of a decaying shock propagating through a uniform density (first problem), we consider a rarefaction wave propagating along the hydrodynamic profiles with finite density, pressure, and entropy gradients (second problem). These two problems will be equivalent if the hydrodynamic profiles of the second problem will satisfy the Hugoniot relations[7] at the shock position in the first problem. If the shock remains strong at all times, the compressed density right after the shock front remains constant, $\rho_s = (\gamma+1)/(\gamma-1)\rho_0$. Therefore, the Hugoniot relations must be satisfied in the second problem at the point where the local density is equal to ρ_s. To simplify the solution of the second problem near the shock front, we order $L_s^{-1} = \partial_x s/s << \gamma\partial_x \rho/\rho = \gamma L_\rho^{-1}$ (the large γ limit), where s is the shell entropy. This leads to an intro-

duction of the long-scale variables $T = t\delta$ and $X = x\delta$, where $\delta \sim L_\rho/(\gamma L_s) << 1$. Next, we expand the mass and momentum equations and all hydrodynamic functions in powers of δ and perform a multiscale analysis. Keeping only the zero-order terms in δ in the conservation equations yields the system $(v-\xi)\partial_\xi \rho + \rho\partial_\xi v = 0$, $(v-\xi)\partial_\xi v + c_s^2 \partial_\xi \rho/\rho = 0$, where $\xi = x/(t-t_p)$ [the rarefaction wave is launched at $t = t_p$]. Solving the last system gives $(v-\xi)^2 = c_s^2$, where $c_s = \sqrt{\gamma p/\rho}$. For the rarefaction wave propagating in the negative x direction, we obtain $v = \xi + c_s$. Then, the pressure profile inside the rarefaction wave becomes

$$p = p_p\left(s_p/s\right)^{1/(\gamma-1)}\left[2c(X,T)/c_p(\gamma+1)\right.$$

$$\left.-(\gamma-1)/(\gamma+1)\xi/c_p\right]^{2\gamma/(\gamma-1)},$$

where $c_p = \sqrt{\gamma p_p/\rho_s}$, $s_p = p_p/\rho_s^\gamma$, and $c(X,T)$ is an undefined function of the long-scale variables. Taking the spatial derivative of pressure at the shock front, $\partial_x p \simeq \partial_\xi p/(t-t_p)$, yields

$$\partial_x \frac{p_s}{p_p} \simeq -\sqrt{\frac{p_s}{p_p}}\frac{2\gamma}{\gamma+1}\frac{1}{c_p(t-t_p)}. \qquad (2)$$

Observe that the gradient does not explicitly depend on the unknown function $c(X,T)$; this significantly simplifies the analysis. Substituting Eq. (2) back into Eq. (1) gives $dp_s/dt = -\beta p_s/(t-t_p)$ and $\beta = \sqrt{2\gamma(\gamma-1)}/(2\gamma-1)$, which leads to

$$\frac{p_s}{p_p} = \frac{\alpha_s}{\alpha_f} = \left(\frac{t-t_p}{t_{\rm rw}}\right)^{-\beta}, \qquad (3)$$

where $t_{\rm rw}$ is the rarefaction wave's propagation time from the outer surface of the foil to the shock front and α_f and α_s are the adiabat[1] at the front surface of the shell and shock front, respectively. It can be shown that the corrections to Eq. (3) due to the long-scale variations are small when $\gamma > 1.2$. Figure 93.14 compares Eq. (3) (dashed curve) with the results of numerical simulation (solid curve) using the one-dimensional Lagrangian code *LILAC*.[13] The figure shows evolution of the pressure at the shock front calculated for a 200-μm-thick DT foil driven by a 300-ps, 3.3×10^{14} W/cm^2 laser pulse ($t_p + t_{\rm rw}$ = 440 ps in this case). A good agreement between theoretical predictions and numerical results confirms the accuracy of Eq. (3). Figure 93.14 also plots the results obtained using the self-similar solution of Ref. 11 (β = 0.78) (dotted curve). Although the self-similar solution accurately predicts the shock pressure's decaying rate after t = 1 ns, the absolute value of the pressure (and the adiabat) is ~40% lower than the value obtained in the simulation.

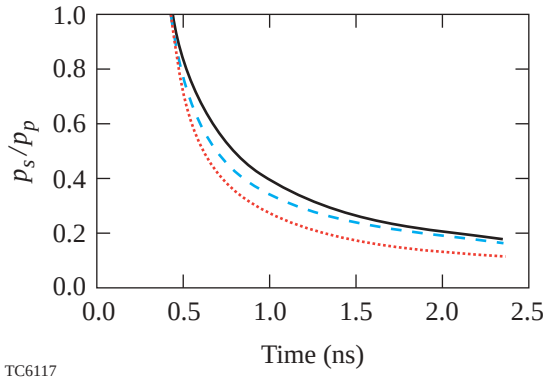

Figure 93.14
Pressure at the shock front calculated using Eq. (3) (dashed curve), results of one-dimensional code *LILAC* (solid curve), and the self-similar solution of Ref. 11 (dotted curve). Calculations are performed for a 200-μm-thick DT foil driven by a 300-ps intensity picket.

Next, using Eq. (3) we calculate the entropy distribution inside the shell in terms of the mass coordinate. First, we introduce the mass m^* per unit area compressed by the shock during time interval $t = t_{\rm rw} + t_p$, $m^* = \rho_0 U_s^p(t_p + t_{\rm rw})$, where $U_s^p = \sqrt{(\gamma+1)p_p/(2\rho_0)}$. The rarefaction-wave propagation time $t_{\rm rw}$ can be related to the picket duration time t_p by equating the distance traveled by the shock (in the frame of reference of the compressed material) $d_s = (t_p + t_{\rm rw})U_{\rm sh}^p(\gamma-1)/(\gamma+1)$ to the distance traveled by the rarefaction wave $d_s = c_p t_{\rm rw}$. This gives $t_p/t_{\rm rw} = \sqrt{2\gamma/(\gamma-1)} - 1$. The fraction of mass dm overtaken by the shock during time dt is $dm = \rho_0 U_s dt$. This gives $dm/dt = (m^*/t_{\rm rw})\sqrt{\alpha_s/\alpha_f}/(1 + t_p/t_{\rm rw})$. With the help of Eq. (3), the solution of the last equation becomes

$$\alpha(m) = \alpha_f\left[\frac{2-\beta}{2}\sqrt{\frac{2\gamma}{\gamma-1}}\left(\frac{m}{m^*}-1\right)+1\right]^{-2\beta/(2-\beta)}. \qquad (4)$$

For a practical application, it is important to determine the duration t_p and the height p_p of the picket that gives the maximum adiabat ratio α/α_b at the beginning of the shell

acceleration (the onset of the RT-instability growth), where $\alpha_b = \alpha(m_{sh})$ is the adiabat at the shell's rear surface and m_{sh} is the total shell mass. The target starts to accelerate soon after the shock breakout at the shell's rear surface. Therefore, to calculate the adiabat at the position of the ablation front at the beginning of the shell acceleration, we must calculate the fraction of the shell material ablated during the shock transit. For a constant applied pressure p_p, the shock transit time across the shell of thickness Δ_0 is $t_{shock} = \Delta_0 \Big/ \sqrt{(\gamma+1)p_p/(2\rho_0)}$. Then, using the scaling of the mass ablation rate

$$\dot{m}\left(g/\mathrm{cm}^2/s\right) = 1.05\times 10^6\, I_{15}^{1/3}$$

and the ablation pressure[1] $p_p(\mathrm{Mbar}) = 80.5\, I_{15}^{2/3}$, we obtain the ablated DT mass during the shock propagation, $\Delta m = 0.2\, m_{sh}$. Here, I_{15} is the laser intensity in units of 10^{15} W/cm^2. Observe that since Δm does not depend on the applied pressure, we can use the derived ablated fraction also in the case of the picket pulse. Substituting $m = \Delta m$ into Eq. (4) we obtain the ablation-front adiabat α_{abl} at the beginning of shell acceleration:

$$\frac{\alpha_{abl}}{\alpha_b} = \left[\frac{(1-\beta/2)\sqrt{2\gamma/(\gamma-1)}\left(m_{sh}/m^* - 1\right)+1}{(1-\beta/2)\sqrt{2\gamma/(\gamma-1)}\left(0.2\, m_{sh}/m^* - 1\right)+1}\right]^{2\beta/(2-\beta)}. \quad (5)$$

Observe that α_{abl} is a monotonically growing function of m^*. Equation (4), however, is valid only for $m \geq m^*$, thus α_{abl} reaches the maximum value at $m^* = 0.2\, m_{sh}$,

$$\max(\alpha_{abl}) = \alpha_b\left[2(2-\beta)\sqrt{\frac{2\gamma}{\gamma-1}}+1\right]^{2\beta/(2-\beta)} = 6.3\,\alpha_b$$

for $\gamma = 5/3$. This shows that at the onset of the RT instability, the maximum ratio of the ablation front and rear-surface adiabat that can be achieved with a single picket pulse is 6. Taking into account that $V_a \sim \alpha^{3/5}$, this gives an increase in the ablation velocity by a factor of 3 at the beginning of the shell acceleration. The ablation velocity, however, decays in time since the ablation front moves into a region with a lower adiabat. Using

$$m^* = \rho_0 U_{sh}^p t_{rw}\sqrt{2\gamma/(\gamma-1)} = 0.2\, m_{sh} = 0.2\rho_0\Delta_0$$

leads to a relation between the applied impulsive pressure p_p, duration of the picket t_p, and the shell thickness Δ_0, $p_p t_p^2 \simeq 9\times 10^{-3}\rho_0\Delta_0^2$. For DT shells, $\rho_0 = 0.25$ g/cm^3, and the picket pressure is $p_p = 6.3\, p_b$, where $p_b(\mathrm{Mbar}) = 2.14\rho_s^{5/3}\alpha_b$ is the pressure at the shell's rear surface. Therefore, the optimum pulse duration becomes $t_p(\mathrm{ns}) \sim 10^{-3}\Delta_0(\mu\mathrm{m})/\sqrt{\alpha_b}$. For a typical OMEGA cryo design $\Delta_0 \sim 80$ μm, and the optimum picket duration for $\alpha_b = 3$ is $t_p \simeq 50$ ps. For the NIF DD designs with $\Delta_0 \simeq 350$ μm, $t_p \simeq 200$ ps. This estimate shows that the new target designs require short picket pulses to optimize the adiabat shape inside the shell. In the next section we study the effect of adiabat shaping on the perturbation growth in the OMEGA and NIF cryogenic target designs.

NIF and OMEGA Target Designs with Adiabat Shaping

Adiabat shaping is expected to reduce the growth rates of the RT-instability modes. The final mode amplitudes, however, depend not only on the growth rates but also on the initial seeds. Such seeds are determined by the surface roughness and the laser imprint amplified/reduced by the perturbation evolution during the early stage of the implosion when the first shock launched at the beginning of the laser pulse propagates through the shell. The perturbation amplification factor at the early stage depends on the details of a particular target design. In this section we study the effects of adiabat tailoring (in both the seeding and the RT-growth rates) in the cryogenic $\alpha = 3$ targets designed for the OMEGA and the NIF laser facilities. Here, α stands for the adiabat at the back of the shell. To avoid confusion, we refer to the OMEGA and NIF $\alpha = 3$ designs previously described in Ref. 14 as the standard designs. The designs presented in the current work will be referred to as picket designs. The standard designs have a very thin (1 μm for the OMEGA shells and 3 μm for the NIF shells) plastic overcoat required for DT-shell fabrication. These targets are driven by a laser pulse that consists of a constant-intensity foot ($I \sim 10^{13}$ W/cm^2) followed by the main drive pulse with $I_{max} \sim 10^{15}$ W/cm^2. The requirement for the very thin overcoat layers comes from the minimization of the early-stage perturbation growth factors. Such a growth is due to an impedance mismatch between plastic and DT ice that leads to an additional perturbation growth by a factor[15] $\sim e^{1.5\sqrt{kd_{CH}}}$, where k is the perturbation wave number and d_{CH} is the overcoat thickness. In the picket designs, such a requirement, as shown later, can be relaxed, and a thicker polymer overcoat is used to facilitate shell manufacturing and to increase the laser absorption. The overcoat thickness is determined by the requirement that the plastic layer be ablated by the beginning of the acceleration phase. This is done to take advantage of the higher ablation velocity of the lower-density DT ice. There is a negative side,

however, in an increased overcoat thickness: when the DT ice becomes the ablator, radiation from the plastic present in the hot corona streams through the ablator, preheating the main fuel. The picket designs, nevertheless, use thicker polymer layers (5 μm for OMEGA and 17 μm for the NIF) since our calculations show the beneficial overall effects of an increased overcoat thickness. The picket designs for OMEGA and the NIF are presented in Fig. 93.15. The laser pulse in both cases consists of a picket [we assume a Gaussian picket with FWHM (full width at half maximum) = t_p], an intensity rise, and the main-drive pulse with the maximum power P_{max}.

Shell thickness is determined by the implosion velocity and the laser energy. The minimum implosion velocity[1] required for ignition of large-aspect-ratio cryogenic targets is min (V_{imp}) ~ 3×10^7 cm/s. The implosion velocity in a robust ignition design must exceed this value in order to have excess kinetic energy at the time of ignition. Such a margin[14,16] helps to compensate for the effects of the shell nonuniformity. A larger value of the implosion velocity is also required to reduce the perturbation growth rates during the deceleration phase of implosion. As shown in Ref. 17, the ablation velocity during the deceleration phase is proportional to the hot-spot temperature to the power 5/2. The larger implosion velocity leads to a higher hot-spot temperature[16] ($T_{hs} \sim V_{imp}$) and larger ablative stabilization of the RT modes during the shell deceleration. Based on results of the stability analysis, we found that the implosion velocity for the direct-drive NIF targets should not be less than 4×10^7 cm/s. For the current design we choose $V_{imp} = 4.3 \times 10^7$ cm/s. A given implosion velocity and the absorbed laser energy (which can be translated into the shell kinetic energy, taking into account the implosion efficiency of ~7%) uniquely determine the shell mass.

Shell radius is defined by minimizing the duration of the shell's coasting phase. Soon after the laser is turned off (end of the acceleration phase), the target starts to decompress: the front and rear surfaces expand with a local sound speed. The expansion of the back of the shell lasts until the main shock reflected from the shell center starts to interact with the incoming shell (beginning of the deceleration phase). Minimizing the time of the shell's free expansion (coasting phase) maximizes the final total ρR. This leads to a requirement on the shell radius: by the time the laser is turned off, the main shock must reach the shell center. If the shell radius is too small, on the other hand, the deceleration phase will begin while the laser is still on. The high pressure in the vapor will prevent, in this case, the shell from gaining the required implosion velocity; therefore, an effective transfer of the absorbed laser energy to the shell's kinetic energy will not be possible.

Laser pulse shape in the picket design is determined by several parameters: (1) rear-surface adiabat, which affects the target neutron yield and shell ρR (it also controls the stability during the deceleration phase), (2) the adiabat shape inside the shell, and (3) proper timing of all shocks and compression waves developed during the implosion. The first two parameters determine the picket peak intensity and picket duration

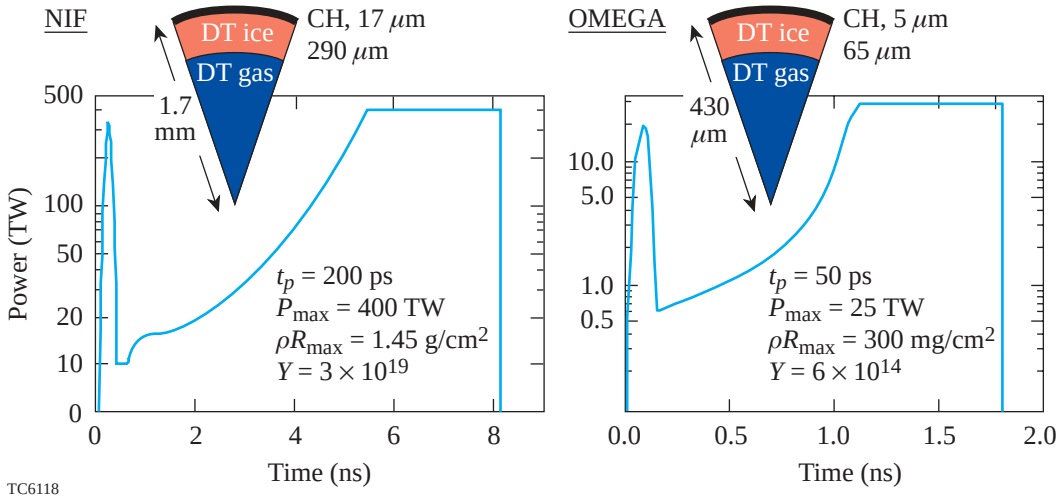

Figure 93.15
Direct-drive, $\alpha = 3$ cryogenic target designs for the OMEGA and NIF laser systems.

(see the previous section). Meeting the third constraint on the pulse shaping requires accounting for all hydrodynamic waves that are launched during the implosion. Next, we summarize the main waves. First, a strong shock wave (SW_1) is launched by the picket at the beginning of the pulse. Then, as the intensity drops to a much lower level after $t = t_p$, a rarefaction wave (RW_p) starts to propagate through the shock-compressed material, and, as soon as the rarefaction catches the shock, the shock strength starts to decrease. The SW_1 sets up the shell adiabat for the entire acceleration phase (with a minor increase due to a radiation preheat and additional hydrodynamic waves). Later, the laser power ramps up to reach the maximum value P_{max}, and a compression wave or a weak shock is formed at the ablation front. To emphasize that such a wave should not turn into a strong shock (this limits the slopes of the intensity rise), we denote this wave as a compression wave (CW). As the SW_1 breaks out at the shell's rear surface, the surface starts to expand, launching a rarefaction wave (RW_b). While the RW_b travels from the rear surface toward the ablation front, it establishes some velocity, pressure, and density gradients. Each fluid element inside the RW_b is accelerated according to $dv/dt = -\partial_x p/\rho$, where p and ρ are the pressure and density of the fluid element. At the head of the rarefaction, ρ is equal to the shell density compressed by the SW_1 and CW. When RW_b reaches the ablation front, the density suddenly drops, creating a large acceleration gradient. This forms a local excess in the pressure that starts to propagate in the form of a compression wave along decreasing pressure and density profiles. A compression wave propagating along a decaying density turns into a shock (SW_2) inside the shell.[18] We want to stress here that SW_2 cannot be avoided. It will be created even for a constant-intensity pulse. The effect of SW_2 on the target performance, however, can be minimized by appropriately choosing the rise time of the laser pulse: the point where the laser reaches the maximum power must be between the SW_1 breakout at the rear surface and the RW_b breakout at the ablation front (in other words, the laser must reach the peak power while RW_b propagates through the shell). In addition, a proper timing of the pulse requires that, while traveling inside the shell, the SW_1 always be ahead of the CW. The time difference, however, between the breakout of the CW and SW_1 at the rear surface must not be larger than $\Delta t = c_s/(\Delta_0/16)$, where c_s is the average sound speed inside the shell compressed by the SW_1, and Δ_0 is the initial shell thickness.

Figure 93.15 shows the picket target designs, taking into account all the constraints on the shell size and pulse shape discussed above (for a better shell stability, the coasting phase in the OMEGA design was extended). The OMEGA design reaches the implosion velocity $V_{imp} = 4.6 \times 10^7$ cm/s, peak of the total $\rho R_{max} = 300$ mg/cm^2, and it produces $Y = 6 \times 10^{14}$ neutrons. The NIF design has, correspondingly, $V_{imp} = 4.3 \times 10^7$ cm/s, $\rho R_{max} = 1.45$ g/cm^2, and $Y = 3 \times 10^{19}$ (gain = 55). Next, we study the stability of the designs presented in Fig. 93.15. We start by analyzing the perturbation growth rates.

1. Reduction in the Rayleigh–Taylor Growth Rates

The main motivation for the adiabat shaping is to increase the ablation velocity of the shell. Such an increase results in a reduction in the RT-growth rates. To separate the effect of the RT-growth-rate reduction from effects of the multiple material interfaces (which will be studied later), we consider a pure-DT shell (no polymer overcoat) driven by both a standard pulse and a picket pulse. The OMEGA all-DT target, equivalent to the design presented in Fig. 93.15, has an outer diameter of 430 μm and a shell thickness $\Delta_0 = 85$ μm. The pulse shape for the standard $\alpha = 3$ OMEGA design is taken from Ref. 14. Averaged over the time of shell acceleration, V_a increases from 4 μm/ns in the standard design to 6.5 μm/ns in the picket design. The RT-growth rates are estimated by substituting the ablation-front trajectories R_a obtained from the 1-D simulation into the fitting growth-rate formula,[20] $\Gamma_{RT} = 0.94\sqrt{kg} - 2.6\, kV_a$. Since the fitting formula uses time-independent planar geometry variables, g, $k = \ell/R_a$, and V_a are averaged over the duration of the acceleration phase. Figure 93.16 shows the results of the fitting formula applied to the two designs. Next, a series of two-dimensional simulations using the Lagrangian code *ORCHID*[21] was performed to calculate the growth rates of the RT modes. The instability was seeded by applying a 1% laser-intensity modulation.

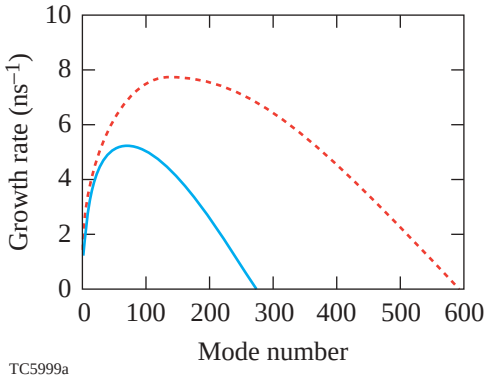

Figure 93.16
Rayleigh–Taylor growth rates for the standard (dashed curve) and the picket (solid curve) OMEGA designs.

Figures 93.17(a) and 93.17(b) compare the results of simulations (solid and dotted lines) with theoretical prediction (dashed straight lines) for mode numbers $\ell = 60$ and $\ell = 100$. Simulations exhibit lower growth rates at the beginning of the acceleration phase and higher growth rates at the end of acceleration. This is mainly due to a wave number variation during shell compression and, in the case of the picket design, lower ablation velocity at the end of the laser pulse. Averaged over the duration of the acceleration phase, however, simulations agree reasonably well with the result of the fitting formula. According to Fig. 93.16, the cutoff mode number is expected to be reduced from $\ell_{\text{cut}} \simeq 600$ for the standard pulse to $\ell_{\text{cut}} \simeq 280$ for the picket design. In Fig. 93.17(c) we plot the temporal evolution of the mode $\ell = 300$, which is predicted to be stable for the picket case. Indeed, the simulations clearly show the mode growth in the standard design and the mode stabilization in the picket design. Based on the results of 2-D simulations we conclude that the reductions in the growth rates due to adiabat shaping are in good agreement with the analytical predictions. Next, we turn our attention to the seeding of the RT modes in the picket design with multiple layers.

2. Seeding of the Rayleigh–Taylor Modes in Multilayer Targets

To calculate the nonuniformity evolution throughout the implosion, it is essential to accurately predict the initial conditions for the RT-instability growth. Such initial conditions, in turn, depend on how the laser imprint and surface roughness evolve prior to the onset of the RT instability (prior to the RW_b breakout at the ablation front). In this subsection we estimate the growth factor of the initial perturbation seeds during the early stage of implosion.

The RW_p (see p. 23) launched into the compressed material establishes a pressure profile decaying toward the ablation front. This creates pressure and density gradients of opposite directions at the CH/DT interface. Thus, a short period of the classical RT growth ("early time" RT growth) occurs at the interface. Such a period lasts until the CW reaches the interface and changes the sign of the pressure gradient. The amplification of the interface perturbations (seeded by the distorted SW_1) can be estimated from the following considerations: The interface between the heavier CH and lighter DT is a Lagrangian point moving with a local fluid velocity. Since the pressure profile across the interface is established by the rarefaction wave RW_p, the interface acceleration is an acceleration of a Lagrangian point inside the rarefaction wave. Next, we consider a rarefaction wave traveling along a stationary uniform density $\bar{\rho}$ and pressure $\bar{p}$. The solution of the hydrodynamic equations in this case written in the Lagrangian coordinates has the form[18] ($\gamma = 5/3$):

$$\rho = \bar{\rho}\left(\frac{x_0}{\bar{c}t}\right)^{3/4}, \quad p = \bar{p}\left(\frac{x_0}{\bar{c}t}\right)^{5/4}, \tag{6}$$

where $\bar{c} = \sqrt{\gamma\bar{p}/\bar{\rho}}$. The time coordinate in the last equation is shifted to the beginning of the rarefaction wave propagation. The acceleration of a Lagrangian point is calculated by taking the derivative of the pressure with respect to the Lagrangian

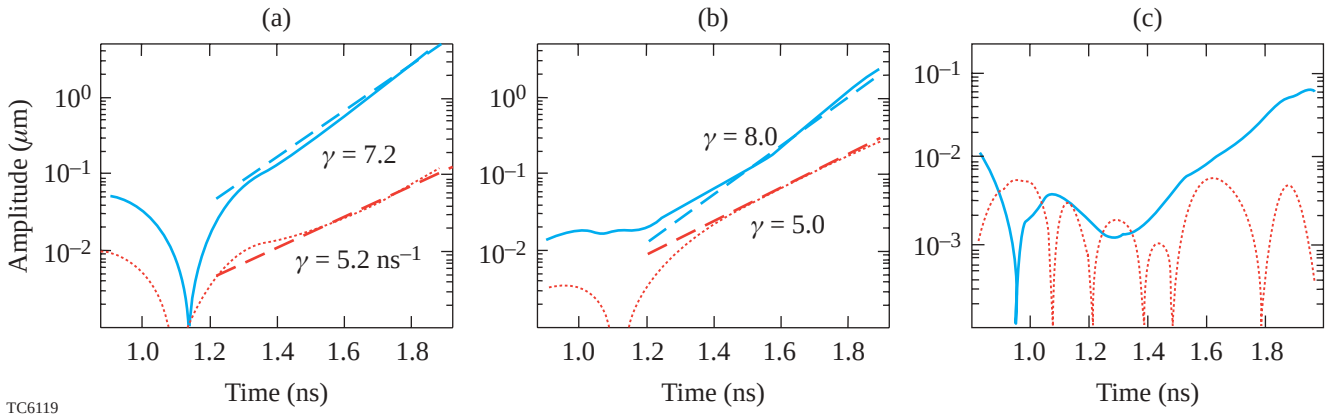

Figure 93.17
Mode evolution for (a) $\ell = 60$, (b) $\ell = 100$, and (c) $\ell = 300$. Numerical results are shown with the solid (standard design) and dotted (picket design) lines; the predictions of the fitting formula[20] are indicated by the dashed straight lines. Calculations are performed for the OMEGA $\alpha = 3$ design.

variable x_0 (at time $t = 0$, the rarefaction wave is at $x_0 = 0$):

$$g = -\frac{1}{\bar{\rho}}\frac{\partial p}{\partial x_0} = -\frac{3}{4}\frac{\bar{c}^2 x_0^{1/4}}{(\bar{c}t)^{5/4}}. \quad (7)$$

Next, we take x_0 to be the polymer thickness (Lagrangian position of the CH/DT interface) at the beginning of the RW_p propagation, $x_0 = \Delta_{CH} = c_{CH}t_r$, where t_r is the RW_p breakout time at the CH/DT interface, and c_{CH} is the sound speed of the shock-compressed CH. Simulations show that $\Delta_{CH} \simeq d_{CH}/6$, where d_{CH} is the initial overcoat thickness (the SW_1 compresses the plastic layer by a factor of 4; additional reductions in thickness are due to the mass ablation and adiabatic compression of the CH layer during the picket rise). The parameter $\bar{c}$ in this case is $\bar{c} = c_{CH} = \sqrt{\gamma p_{CH}/\rho_{CH}}$, where p_{CH} is the pressure at the shock front in CH and $\rho_{CH} = (\gamma+1)/(\gamma-1)\rho_{CH}^0$ is the shock-compressed CH density. Next, to find the perturbation growth fac-tor at the interface, we must solve the RT evolution equation (including decompression effects):

$$\frac{d}{dt}\left[\frac{d_t(\rho\eta)}{\rho}\right] - A_T k g \eta = 0, \quad (8)$$

where η is the CH/DT interface modulation amplitude, k is the wave number, and, according to the *LILAC* simulations, $A_T \simeq 1/3$. The Wentzel–Kramers–Brillouin (WKB) solution[22] of Eq. (8) has the form

$$\eta = \tau^{11/16}\left(Ae^{\zeta} + Be^{-\zeta}\right),$$

where $\zeta = 4/3\sqrt{k\Delta_{CH}}\,\tau^{3/8}$ and $\tau = c_{CH}t/\Delta_{CH}$. Equation (8) is subject to the initial conditions at the onset of the perturbation growth: $\eta(t = t_r) = \eta_0$ and $\dot{\eta}(t_r) = \dot{\eta}_0$. These conditions can be defined from the following considerations: If the interface perturbation is seeded by a nonuniform shock with a modulation amplitude η_s, then η_0 and η_s are related as $\eta_0 = \eta_s U_{ps}^{DT}/U_s^{CH}$, where

$$U_{ps}^{DT} = \sqrt{2/(\gamma+1)\,p^{DT}/\rho_{DT}^0}$$

is the post-shock fluid velocity in DT and

$$U_s^{CH} = \sqrt{p_p(\gamma+1)/2/\rho_{CH}^0}$$

is the shock velocity in CH. Because of the density jump across the CH/DT interface, the pressure behind the SW_1 drops as the shock crosses the interface. The transmitted pressure p_{DT} must satisfy the following equation derived from the matching conditions across the interface:

$$\sqrt{\Sigma} - \sqrt{\frac{\rho_{DT}^0}{\rho_{CH}^0}} = \sqrt{\frac{2\gamma}{\gamma-1}\frac{\rho_{DT}^0}{\rho_{CH}^0}}\left(1 - \Sigma^{\frac{\gamma-1}{2\gamma}}\right),$$

where $\Sigma = p_{DT}/p_p$. Substituting $\rho_{DT}^0 \simeq \rho_{CH}^0/4$, the last equation yields $p_{DT} \simeq 0.45\,p_p$; thus the transmitted pressure is one-half of the initial drive pressure. Thus, the initial interface amplitude becomes $\eta_0 \simeq \eta_s$. It is interesting to observe that the initial interface perturbation is approximately equal to the shock modulation amplitude. To calculate the initial velocity perturbation $\dot{\eta}_0$ we must take into account that the RW_p in the designs presented in Fig. 93.15 catches with the SW_1 inside the plastic, very close to the CH/DT interface. Thus, we can approximate that the interface starts to accelerate with g, defined by Eq. (7), right after the SW_1 crosses the interface. The velocity perturbation gained by the interface during time interval Δt is $\dot{\eta}_0 = g\Delta t$, where $\Delta t = \eta_s/U_s^{CH}$ is the time of the shock propagation across the amplitude η_s; then, $\dot{\eta}_0 \simeq 0.42\,\eta_s\,c_{CH}/\Delta_{CH}$. If the perturbations are seeded by the outer-surface roughness and the initial amplitude of the front ripple is a_0, then the shock amplitude[23] evolves according to

$$\eta_s(t) = a_0\left[J_0\left(kc_{CH}\,t/\mu\right) + 2/3\;J_2\left(kc_{CH}\,t/\mu\right)\right],$$

where $J_0(x)$ and $J_2(x)$ are Bessel functions of zero and second orders, respectively, and

$$\mu = 1\Big/\sqrt{1-\left(U_s^{CH}/4c_{CH}\right)^2} \simeq 1$$

in the strong shock limit. Approximating the Bessel functions with their envelopes gives $J_0(z) + 2/3J_2(z) \simeq \sqrt{2/(9\pi z)}$, where z calculated at the SW_1 breakout time at the interface is $z \simeq kd_{CH}/2$. Collecting all the terms together, the perturbation growth factor $GF = \eta(t)/a_0$ becomes

$$\mathrm{GF} = \frac{0.38}{\sqrt{kd_{\mathrm{CH}}}}\left(\frac{t}{t_r}\right)^{11/16} \times\left(\cosh\sigma - \frac{0.8}{\sqrt{kd_{\mathrm{CH}}}}\sinh\sigma\right), \qquad (9)$$

where $\sigma = 0.54\sqrt{kd_{\mathrm{CH}}}\left[\left(t/t_r\right)^{3/8} - 1\right]$. The perturbations imposed at the CH/DT interface by the perturbed SW_1 grow until the CW reaches the interface and changes the sign of the pressure gradient. Figure 93.18 plots the GF calculated for the NIF design presented in Fig. 93.15 ($t/t_r \sim 40$). The mode number ℓ is defined as $k = \ell/R_0$, where $R_0 = 1700$ μm is the initial outer shell radius. The amplification in the mode amplitude, for the mode numbers of interest to ICF, varies from 1 to 30, but only a fraction of this amplitude seeds the RT mode at the onset of the target acceleration. This is partially due to the interface amplitude compression by the CW. An additional reduction comes from the coupling of the interface ripple to the ablation front, which is stabilized by the dynamic overpressure effect.[24] Figure 93.19 illustrates the reduction in the interface amplitude prior to the target acceleration. The interface modulation evolution is calculated using 2-D *ORCHID* simulations with an imposed initial outer-surface perturbation. The dashed line represents the behavior of mode $\ell = 100$ with $a_0 = 0.5$ μm, and the solid line corresponds to $\ell = 300$ with $a_0 = 0.2$ μm. The SW_1 breaks out at the CH/DT interface at 0.4 ns. At this time the interface modulation jumps to the value of the shock ripple amplitude (the shock modulation for ℓ = 300 changes sign at $t = 0.4$ ns; therefore the plot shows the growth of this starting from zero amplitude). Although the short wavelengths experience a larger growth due to the early RT instability, their amplitudes are substantially reduced by the time of shell acceleration. The conclusion one can draw from this analysis is that the early RT growth of the CH/DT interface perturbations does not amplify significantly the seeds for the acceleration RT instability. Even if such amplification by a factor of several will occur, the perturbations will be substantially reduced by high ablation velocity (the adiabat has the largest value at the interface) when the ablation front crosses the CH/DT interface.

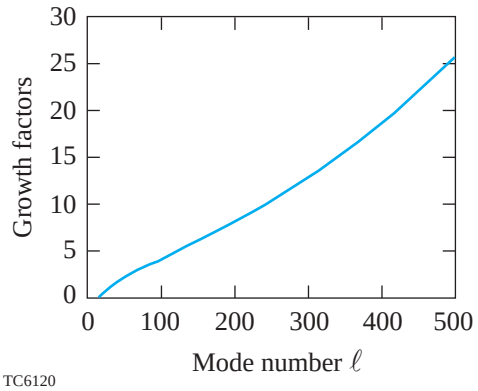

Figure 93.18
Growth factors of the "early time" RT instability in the NIF picket design.

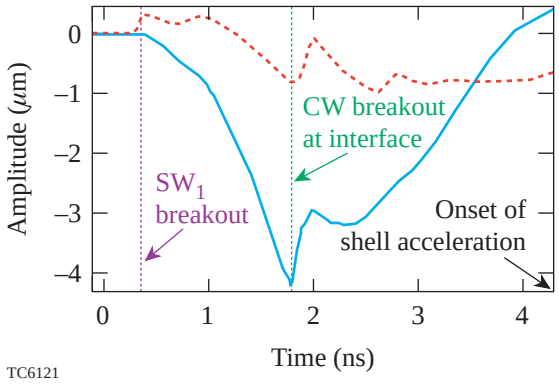

Figure 93.19
Evolution of the CH/DT interface modulation for $\ell = 100$ (dashed line) and $\ell = 300$ (solid line) prior to shell acceleration.

3. Convective Instability

It is well known that in the presence of the entropy gradient inside the shell, a convective instability develops if the effective acceleration and the entropy gradient are in the same direction.[7] Such an instability has been studied by several researchers in the past.[7,25] The following are important results of these studies: (1) In the classical RT case (no ablation) with negligibly small light-fluid density ($A_T \sim 1$), the convective mode is totally decoupled from the RT mode, and the RT-growth rate is $\gamma = \sqrt{kg}$, regardless of the adiabat shape (assuming a sharp interface between lighter and heavier fluids). (2) The growth rate of the convective modes is always smaller than the growth of the RT modes. The growth rates of the modes excited in the shell can be derived by combining the conservation equations into a single differential equation for the x component of the fluid velocity v (x coordinate is chosen in the direction of the acceleration g):

$$\left(\Gamma^2 v - g\frac{dv}{dx}\right) = \left[c_s^2\frac{d}{dx} + (\gamma - 1)g\right] \times \left(\Gamma^2 + k^2 c_s^2\right)^{-1}\left(\Gamma^2\frac{dv}{dx} - k^2 g v\right), \quad (10)$$

where k is the wave number, Γ is the perturbation growth rate, and $c_s = \sqrt{\gamma p/\rho}$ is the sound speed. In writing Eq. (10) the ablation effects were neglected. If $x = 0$ at the fluid interface and x is negative inside the shell, the pressure continuity condition at the interface reads as

$$p(\eta) = p_0(0) + \tilde{p}(0) + (dp/dx)\eta = p_0(0),$$

where $\tilde{p}$ is the pressure perturbation, p_0 is the equilibrium pressure, and η is the interface modulation amplitude. The velocity at the interface is related to the distortion amplitude as $v(0) = \Gamma\eta$; in addition, we write $dv/dx|_{x=0} = \mu k v(0)$, where μ is an undetermined constant. The pressure continuity in this case reduces to the simple relation

$$\Gamma = \sqrt{\frac{kg}{\mu}}. \quad (11)$$

It is easy to show that the solution $v \sim e^{kx}$ and $\Gamma = \sqrt{kg}\,(\mu = 1)$ satisfies Eq. (10); thus, the classical RT mode grows with $\Gamma = \sqrt{kg}$, regardless of the entropy profile inside the shell. As shown in Ref. 7, however, for all other modes that can be excited in the shell (the internal convective modes), $\mu > 1$ and the growth rates are smaller than $\sqrt{kg}$. In the ablative case, the growth rates of the RT instability are significantly reduced by the ablation. For the DT ablator, the fitting formula that reproduces the results of the self-consistent theory has the form[20] $\Gamma_{RT} = 0.94\sqrt{kg} - 2.6\,kV_a$. Near the cutoff wave number, where Γ_{RT} vanishes, the growth of the convective modes could exceed the RT growth. It is important, therefore, to study the internal mode growth in such a regime.

We begin the analysis by determining the spatial dependence of the adiabat for the picket designs shown in Fig. 93.15. The shell entropy $s(x)$ calculated using the 1-D simulations can be fitted with a power law $s(x) = s_0\left[1 - x/(\beta_s L_{sm})\right]^{-\beta_s}$, where L_{sm} (the minimum entropy gradient scale length) and the power index β_s are determined from the fitting procedure. The x coordinate is negative inside the shell, so $s(x)$ decreases from the interface toward the back of the shell. Next, we solve Eq. (10) to find the eigenvalue μ, imposing the condition of finite v at the back of the shell. Near the RT cutoff, the condition $kL_{sm} >> 1$ is satisfied, and Eq. (10) can be greatly simplified:

$$v'' - k^2 Q(x) v = 0,\ Q(x) = 1 - \frac{\mu}{\gamma k L_s},\ L_s = L_{sm} - \frac{x}{\beta_s}. \quad (12)$$

Here, prime denotes the spatial derivative. In solving Eq. (12) we assume $\mu >> 1$. This assumption will be verified later. Observe that Q is a decaying function of x; therefore the solution of Eq. (12) depends on the sign of Q inside the shell. It is easy to show that Q cannot be positive everywhere in the shell. Indeed, to satisfy the boundary condition at the shell's back, we must keep only the exponentially decaying solution

$$v_{WKB} \sim Q^{-1/4}\exp\left[k\int^x \sqrt{Q(y')}\,dy'\right],$$

where v_{WKB} is obtained using the WKB approximation. But such a solution does not satisfy the boundary condition at $x = 0$, $v'/v = k\mu$. Thus, Q must be negative somewhere in the shell. Next, we distinguish the following two cases: (1) Q changes sign at point $x = \bar{x}$, (2) Q is negative everywhere. In case (1), solution of Eq. (12) in the region where $Q > 0$ is $v = v_{WKB}$. In the vicinity of $x = \bar{x}$, the WKB approximation breaks down and Eq. (12) must be solved by expanding Q in the Taylor series,

$$Q = Q_0 - Q_1 k(x - \bar{x}),$$

where $Q_0 = 1 - \mu/\left[\gamma\left(kL_{sm} - k\bar{x}/\beta_s\right)\right] = 0$, and $Q_1 = \gamma/(\mu\beta_s)$. Then, the solution of Eq. (12) that matches v_{WKB} at $\tau \to \infty$ becomes $v_{in} \sim \mathrm{Ai}(\tau)$, where $\mathrm{Ai}(\tau)$ is the Airy function and $\tau = kQ_1^{1/3}(\bar{x} - x)$. We will show later that $|Q_1 k\bar{x}| << 1$ and the Taylor expansion of Q is still valid near $x = 0$. The boundary condition $v'/v = \mu k$ can be applied in this case to v_{in}. Using the expansion of the Airy function for the large negative arguments, the boundary condition reads as

$$\frac{1}{4\tau_0} + \sqrt{\tau_0}\,\tan\left(\frac{2}{3}\tau_0^{3/2} - \frac{\pi}{4}\right) + \mu^{4/3}(\beta_s/\gamma)^{1/3} = 0, \quad (13)$$

where $\tau_0 = \beta_s^{2/3}(\mu/\gamma - kL_{sm})(\gamma/\mu)^{1/3}$ is the value of $-\tau$ at the density jump ($x = 0$). Since $\mu >> 1$ (by assumption), the

right-hand side of Eq. (13) is large, and the equation can be satisfied only if the argument of the tangent is close to $\pi/2$. This defines τ_0, $(2/3)\tau_0^{3/2} \simeq 3\pi/4 + \pi n$, $n = 0,1,2$. Substituting the definition of τ_0 into the last equation leads to $\beta_s^2\gamma\left(\mu/\gamma - kL_{\rm sm}\right)^3 = 9\pi^2\left(3/4+n\right)^2\mu/4$, which has the following solution:

$$\mu = \gamma kL_{\rm sm} + \frac{\gamma}{4\beta_s}\left[9\pi^2(3+4n)^2\beta_s kL_{\rm sm}\right]^{1/3},\ n = 0,1,2. \quad (14)$$

Observe that $\mu >> 1$ for the short-wavelength modes considered here, in agreement with the initial assumption. Also, $\left|kQ_1\bar{x}\right| \sim \left(kL_{\rm sm}\right)^{-2/3} << 1$, which validates the Taylor expansion of Q near $x = 0$. Using Eq. (14), the growth rate $\Gamma = \sqrt{kg/\mu}$ takes the form

$$\Gamma = \sqrt{\frac{g}{\gamma L_{\rm sm}\left\{1+\left[\frac{9\pi(1+4n/3)}{8\beta_s kL_{\rm sm}}\right]^{2/3}\right\}}}. \quad (15)$$

Next, we recall that Eq. (15) is valid only if Q changes sign inside the shell, i.e., $-d < \bar{x} < 0$, where d is the shell thickness. Such a requirement puts an upper limit on values of μ: $\mu < \gamma k\left(L_{\rm sm} + d/\beta_s\right)$; using Eq. (14), the last condition reads as $n < \left(2\beta_s kL_{\rm sm}/3\pi\right)\left(d/\beta_s L_{\rm sm}\right)^{3/2}$. The number n has a simple meaning: n indicates how many times the eigenmode changes sign inside the shell. To calculate the number n for the ICF target, we must recall that the internal modes are seeded only by the vorticity inside the shell.[7] In the ICF experiments the vorticity is induced either by the rippled shock propagating from the ablation front or by the rippled rarefaction wave in the case of the initial inner-surface roughness (feedout). In both cases the imposed vorticity oscillates inside the shell, and the characteristic spatial frequency of such oscillations is of the order of the perturbation wavelength. As an example, let us consider the case of the rippled shock. If a_0 is the initial outer-surface amplitude of the mode with the wave number k, the shock creates the shell vorticity[23,24] Ω_0 according to

$$\Omega_0 = i\left(\nabla\times\mathbf{v}\right)_z = -kv_x - i\partial_x v_y$$

$$\simeq \frac{3}{2}k^2 a_0 c_s\left[J_1(\zeta) + \frac{1}{2}J_3(\zeta)\right], \quad (16)$$

where $\zeta = k\Delta_0/2\left(m/m_{\rm sh}\right)$, $J_1(\zeta)$ and $J_3(\zeta)$ are the Bessel functions, m is the mass coordinate inside the shell, $m_{\rm sh}$ is the total shell mass, and Δ_0 is the initial shell thickness. Taking into account that 1/5 of the initial shell material is ablated by the time the shell accelerates (see the **Propagation of a Decaying Shock** section), $\zeta_{\max} = 2k\Delta_0/5$. Using Eq. (16) and approximating $J_m(\zeta) \sim \sin\left(\zeta - m\pi/2 - \pi/4\right)$, it is easy to calculate the number of zeros in Ω_0: $N_0 \sim 2k\Delta_0/(5\pi)$. Taking $n = N_0$, the validity condition of Eq. (15) becomes

$$\frac{\Delta_0}{d} < \frac{5}{3}\sqrt{\frac{d}{\beta_s L_{\rm sm}}}. \quad (17)$$

This condition is not satisfied for the target designs presented in Fig. 93.15 [$\Delta_0/d \sim 10$ (shell is compressed by the shock SW_1 and the compression wave CW), $d \simeq 8\ \mu$m, $L_{\rm sm} \simeq 5.4\ \mu$m, and $\beta_s = 0.5$ for the OMEGA picket design]. Thus, to calculate the convective instability growth rate we must consider the second case when Q is always negative inside the shell.

If $Q < 0$, the WKB solution of Eq. (12) takes the form

$$v = \frac{A}{Q_-^{1/4}}\cos\left(k\int_0^x\sqrt{Q_-(y')}dy'\right)$$

$$+\frac{B}{Q_-^{1/4}}\sin\left(k\int_0^x\sqrt{Q_-(y')}dy'\right), \quad (18)$$

where $Q_- = -Q > 0$ and A and B are constants of integration. The boundary condition at $x = 0$ relates $B \simeq A\mu/\sqrt{Q_-(0)}$. To define the boundary condition at $x = -d$, we must keep in mind that both ρ and c_s vanish at the rear surface. Then, the solution that does not blow up at $x = -d$ must satisfy $v'(-d)/v(-d) = \mu k\left(\gamma - 1\right)/\gamma$ [this condition can be easily derived directly from Eq. (10)]. Applying the latter condition to solution (18) gives, in the limit of large μ,

$$k\int_{-d}^0\sqrt{\frac{\mu}{\gamma kL_s(x)} - 1}\,dx = n\pi,\ n = 1,2... \quad (19)$$

Performing integration in the last equation and substituting $n = N_0$, we determine μ. Then, the growth rate $\Gamma = \sqrt{kg/\mu}$ becomes

$$\Gamma \simeq \sqrt{\frac{g}{\gamma L_{\mathrm{sm}} \Sigma}},$$

$$\Sigma = \frac{\left(d/\sqrt{2}\beta L_{\mathrm{sm}}\right)^2 + \left(\Delta_0/5\beta L_{\mathrm{sm}}\right)^2}{\left(\sqrt{1+d/\beta L_{\mathrm{sm}}}-1\right)^2} - \frac{1}{2}\sqrt{1+\frac{d}{\beta L_{\mathrm{sm}}}}. \tag{20}$$

Figure 93.20 plots the growth rates calculated for the OMEGA picket design using Eqs. (15) (n = 0, dashed line) and (20) (solid line). Observe a strong reduction in the growth rate due to the vorticity oscillations. We want to emphasize here that Eq. (20) is valid only if condition (17) is not satisfied. It is possible, however, to steepen the adiabat profile (by introducing a second picket in the laser pulse, for example), reducing the minimum scale length L_{sm} and increasing the compressed shell thickness d (the larger adiabat at the ablation front will lead to a decrease in the shell density). Equation (17) will be satisfied in this case, and Eq. (15) with $n = N_0$ must be used to calculate the growth rate. To validate the result of the performed analysis of the convective mode evolution, we carried out a series of single-mode 2-D *ORCHID* simulations imposing modulation on the outer surface of the shell. Figure 93.21 shows a plot of the density and vorticity as functions of the mass for $\ell = 300$ in the OMEGA picket design (Fig. 93.15). The dashed line represents the beginning of acceleration phase, and the solid line corresponds to the end of the acceleration phase (the mass is reduced because of the ablation). The vorticity amplitude has grown by a factor of 2 during the shell acceleration, which is in agreement with Eq. (20) (the acceleration phase in the OMEGA design lasts for 0.8 ns).

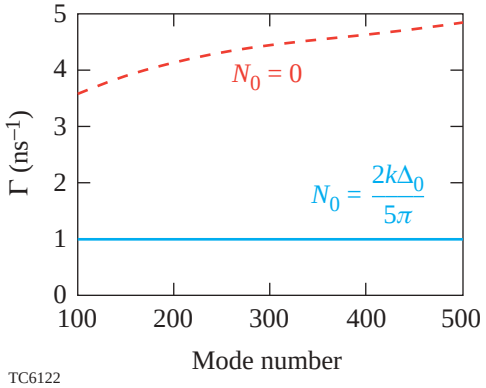

Figure 93.20
Growth rate of the internal convective mode with (solid line) and without (dashed line) vorticity oscillation inside the shell.

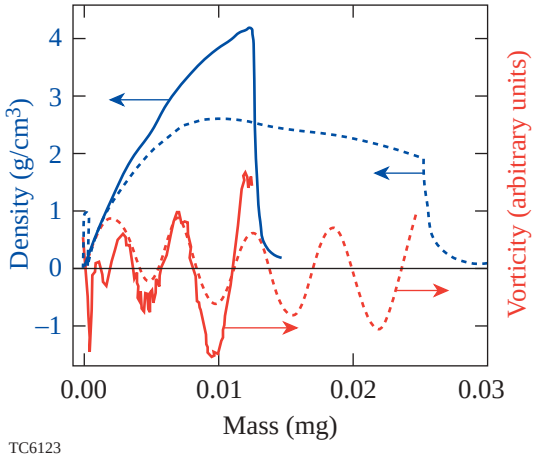

Figure 93.21
Mass density and vorticity calculated at the beginning (dashed line) and the end (solid line) of the acceleration phase.

In conclusion, Fig. 93.20 suggests that there is no significant amplification of the outer-surface distortions due to the convective instability (the growth factor is less than 3 for the entire mode spectrum). One needs to take the results of the present analysis with great caution. We did not address the question of how the internal mode can affect the growth of the RT modes. This issue will be studied in future work. Our simulations, however, indicate that even if such coupling exists, it does not significantly modify the RT growth for the designs described in Fig. 93.15. The conclusions could be different for other shaped-adiabat designs.

4. Multimode Results

The analysis performed in Subsections 1–3 gives an estimate for only the single-mode growth factors experienced by the perturbations during the implosion. To make a conclusion about the shell integrity for a particular target design, one must carry out multimode calculations, taking into account the realistic spectra of the surface roughness and the laser-intensity nonuniformity. Stability analyses of the direct-drive cryogenic targets reported in the past[14,19] reveal that the laser imprint is the dominant source for a potential shell breakup during the acceleration phase. To study the effect of the adiabat shaping on the shell integrity, we performed a set of multimode *ORCHID* simulations. First, we discuss the simulation results for the OMEGA cryogenic targets (dimensions are shown in Fig. 93.15) driven by the standard and picket pulses. A single-beam laser nonuniformity spectrum is evaluated for a static DPP (distributed phase plate) speckle. Then, an overlap of 12 OMEGA beams and two polarizations at any spot on the capsule are assumed. The effect of the two-dimensional SSD

(smoothing by spectral dispersion) beam-smoothing technique[26] is modeled by employing a "flipping" approximation: the sign of the laser perturbation is randomly chosen every correlation time t_c, where $t_c = \left[\Delta\nu \sin\left(k\delta/2\right)\right]^{-1}$, δ is the speckle size (δ = 2.35 μm for the OMEGA), $\Delta\nu$ = 1 THz is the laser bandwidth, and k is the perturbation wave number. Averaged over time T, the single-beam rms nonuniformity σ for a constant-intensity laser pulse decays in time as $\sigma \sim \sigma_0\sqrt{t_c/T}$. Because of a finite maximum angular spread $\Delta\theta$ of the light propagating through the laser, the averaged mode amplitude cannot be reduced to the levels below the asymptotic limit. This limit is inversely proportional to the square root of the number of statistically independent speckle patterns

$$N_{\text{stat}}(\lambda) = \left(4S^x_{\max}/\lambda\right)\left(4S^y_{\max}/\lambda\right),$$

where λ is the nonuniformity wavelength, $S^{x(y)}_{\max} = F\Delta\theta^{x(y)}$ is the maximum spatial shift in the $x(y)$ direction, F = 180 cm is the focal length, and $\Delta\theta^x$ = 50 μrad and $\Delta\theta^y$ = 100 μrad for the OMEGA laser system. The asymptotic limits are modeled in the flipping approximation by selecting only N_{stat} independent choices for the sign of the nonuniformity amplitude. Snapshots of the shell isodensity contours for the standard and the picket designs are shown in Figs. 93.22(a) and 93.22(b), respectively. The shell has moved the same distance (~100 μm) in both designs. The plots reveal a dramatic reduction in shell

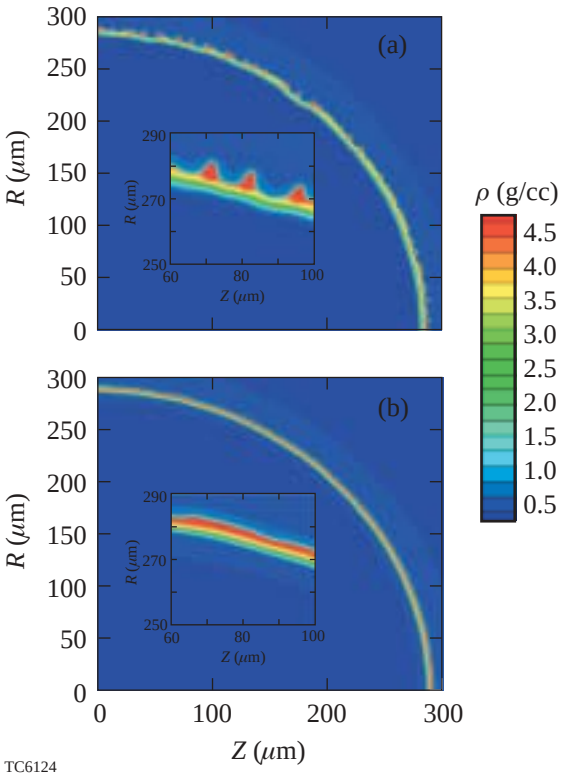

Figure 93.22
Isodensity contours of the (a) standard and (b) picket OMEGA α = 3 designs. At the time shown on the plots, the shell has moved 100 μm in both designs.

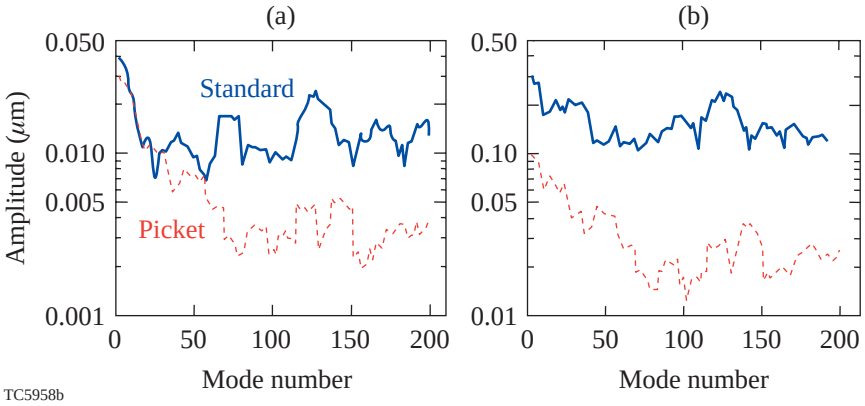

Figure 93.23
Mode spectra for the standard (solid line) and picket (dashed line) OMEGA α = 3 designs (a) at the beginning of acceleration phase and (b) at the time shown on Fig. 93.22(b).

nonuniformity in the picket design. We also emphasize that the picket reduces not only the perturbation growth rates but also the laser imprint.[27] Figure 93.23(a) plots the mode spectrum at the beginning of the acceleration phase for both designs. As shown in the plot, the picket reduces the initial amplitudes by a factor of 2.5 to 3 for the modes with $\ell > 50$. Comparing the mode amplitudes for the picket and standard designs at the time shown in Fig. 93.22 [see Fig. 93.23(b)], we observe that the separation between the two spectral lines is clearly increased (amplitudes in the picket designs are smaller by a factor of 10 for $\ell > 50$), indicating a slower RT growth in the picket design. A reduction in the growth of the low-ℓ modes is also noticeable. This is due to the ablation effects in a finite-thickness shell (for details see Ref. 28). The numerical simulations of the NIF cryogenic target design show a similar trend: shell nonuniformities are highly reduced in the picket design compared to the standard design. Although detailed multimode simulations including all the nonuniformity sources (surface roughness, laser imprint, and power imbalance) are still in progress, a preliminary analysis reported in this article indicates a substantial improvement in the shell uniformity by using laser-induced adiabat shaping.

Picket Pulse Experiments

To test the effect of the adiabat shaping on the performance of the imploding shells, a series of experiments[10] were carried out on the OMEGA laser system. The experiments were performed on 33-μm thick, 905-μm-diam, D_2-filled polystyrene shells, filled to a pressure of 3 and 15 atm. Two pulse shapes [Fig. 93.24(a)] were used to compress the shells with a low adiabat ($\alpha = 2$) at the fuel/pusher interface. The standard pulse has a 1-TW, 700-ps-long foot followed by the main pulse with a peak power of 20 TW. The picket design has a narrow, 100-ps-FWHM (full width at half maximum) Gaussian picket combined with the main drive pulse described above. The adiabat in the standard pulse varies from 2 to 2.5; the adiabat at the ablation front in the picket design was raised to 4. There was also an increase in the adiabat at the rear surface in the picket design. Analysis performed using the stability post-processor[28] indicated that the shell in the standard design was broken due to the perturbation growth, while the shell in the picket design remained intact during the shell implosion. The experimental results are summarized in Fig. 93.24(b). The plot compares the experimental yield against the 1-D *LILAC* prediction. Observe that the predicted yields for the picket design were slightly reduced for both fill pressures, while the experimental yields grew by a factor of 2.5 for the 15-atm fill and by a factor of 2 for the 3-atm fill. The ratio of the experimental yield to the predicted 1-D yield grew from 4% to 18% for the 15-atm fill and from 3% to 15% for the 3-atm fill. A significant improvement in neutron yields indicates a better stability of the implosion shells when a picket was added to the drive laser pulse. A detailed analysis has revealed, however, that the radiation transport in CH shells leads to an additional shaping of the shell adiabat. The effect of such additional shaping will be addressed in future work.

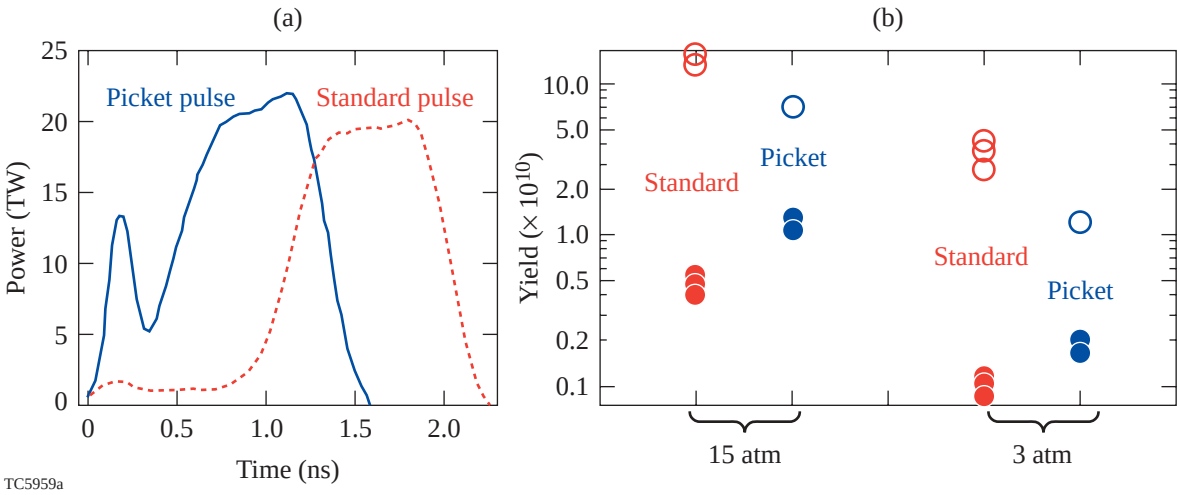

Figure 93.24
(a) Experimental laser pulses for the standard (dashed line) and picket (solid line) $\alpha = 2$, 33-μm-CH-shell target designs. (b) Neutron yield for the standard and picket pulses as predicted by the 1-D code *LILAC* (open circles) and obtained in the experiments (solid circles).

ACKNOWLEDGMENT

One of the authors (V. G.) thanks Dr. A. Velikovich for many helpful discussions. This work was supported by the U.S. Department of Energy Office of Inertial Confinement Fusion under Cooperative Agreement No. DE-FC03-92SF19460, the University of Rochester, and the New York State Energy Research and Development Authority. The support of DOE does not constitute an endorsement by DOE of the views expressed in this article.

REFERENCES

1. J. D. Lindl, *Inertial Confinement Fusion: The Quest for Ignition and Energy Gain Using Indirect Drive* (Springer-Verlag, New York, 1998).

2. S. E. Bodner, D. G. Colombant, J. H. Gardner, R. H. Lehmberg, S. P. Obenschain, L. Phillips, A. J. Schmitt, J. D. Sethian, R. L. McCrory, W. Seka, C. P. Verdon, J. P. Knauer, B. B. Afeyan, and H. T. Powell, Phys. Plasmas **5**, 1901 (1998).

3. S. E. Bodner, Phys. Rev. Lett. **33**, 761 (1974); J. Sanz, Phys. Rev. Lett. **73**, 2700 (1994); V. N. Goncharov, R. Betti, R. L. McCrory, P. Sorotokin, and C. P. Verdon, Phys. Plasmas **3**, 1402 (1996); J. D. Kilkenny, S. G. Glendinning, S. W. Haan, B. A. Hammel, J. D. Lindl, D. Munro, B. A. Remington, S. V. Weber, J. P. Knauer, and C. P. Verdon, Phys. Plasmas **1**, 1379 (1994); S. G. Glendinning *et al.*, Phys. Plasmas **7**, 2033 (2000); C. Cherfils *et al.*, Phys. Rev. Lett. **83**, 5507 (1999); J. Grun *et al.*, Phys. Rev. Lett. **53**, 1352 (1984); J. P. Knauer, R. Betti, D. K. Bradley, T. R. Boehly, T. J. B. Collins, V. N. Goncharov, P. W. McKenty, D. D. Meyerhofer, V. A. Smalyuk, C. P. Verdon, S. G. Glendinning, D. H. Kalantar, and R. G. Watt, Phys. Plasmas **7**, 338 (2000).

4. S. Chandrasekhar, in *Hydrodynamic and Hydromagnetic Stability* (Oxford University Press, Glasgow, 1961).

5. S. E. Bodner, J. Fusion Energy **1**, 221 (1981).

6. J. D. Lindl and W. C. Mead, Phys. Rev. Lett. **34**, 1273 (1975).

7. L. D. Landau and E. M. Lifshitz, *Fluid Mechanics*, 2nd ed. (Butterworth-Heinemann, Newton, MA, 1987); D. L. Book and I. B. Bernstein, J. Plasma Phys. **23**, 521 (1980).

8. T. R. Boehly, D. L. Brown, R. S. Craxton, R. L. Keck, J. P. Knauer, J. H. Kelly, T. J. Kessler, S. A. Kumpan, S. J. Loucks, S. A. Letzring, F. J. Marshall, R. L. McCrory, S. F. B. Morse, W. Seka, J. M. Soures, and C. P. Verdon, Opt. Commun. **133**, 495 (1997).

9. J. Paisner *et al.*, Laser Focus World **30**, 75 (1994).

10. J. P. Knauer, V. N. Goncharov, P. W. McKenty, T. C. Sangster, R. Betti, V. Yu. Glebov, T. J. B. Collins, D. D. Meyerhofer, P. B. Radha, C. Stoeckl, J. A. Frenje, C. K. Li, R. D. Petrasso, and F. H. Séguin, "Improved Performance of Direct-Drive Implosions with a Laser-Shaped Adiabat," submitted to Physical Review Letters.

11. Ya. B. Zel'dovich and Yu. P. Raizer, *Physics of Shock Waves and High-Temperature Hydrodynamic Phenomena*, edited by W. D. Hayes and R. F. Probstein (Dover Publications, Mineola, NY, 2002).

12. R. J. Trainor and Y. T. Lee, Phys. Fluids **25**, 1898 (1982).

13. J. Delettrez and E. B. Goldman, Laboratory for Laser Energetics Report No. 36, University of Rochester (1976).

14. P. W. McKenty, V. N. Goncharov, R. P. J. Town, S. Skupsky, R. Betti, and R. L. McCrory, Phys. Plasmas **8**, 2315 (2001).

15. V. N. Goncharov, S. Skupsky, T. R. Boehly, J. P. Knauer, P. McKenty, V. A. Smalyuk, R. P. J. Town, O. V. Gotchev, R. Betti, and D. D. Meyerhofer, Phys. Plasmas **7**, 2062 (2000).

16. W. K. Levedahl and J. D. Lindl, Nucl. Fusion **37**, 165 (1997).

17. V. Lobatchev and R. Betti, Phys. Rev. Lett. **85**, 4522 (2000).

18. R. Betti, V. Lobatchev, and R. L. McCrory, Phys. Rev. Lett. **81**, 5560 (1998).

19. Laboratory for Laser Energetics LLE Review **79**, 121, NTIS document No. DOE/SF/19460-317 (1999). Copies may be obtained from the National Technical Information Service, Springfield, VA 22161.

20. R. Betti, V. N. Goncharov, R. L. McCrory, and C. P. Verdon, Phys. Plasmas **5**, 1446 (1998).

21. R. L. McCrory and C. P. Verdon, in *Computer Applications in Plasma Science and Engineering*, edited by A. T. Drobot (Springer-Verlag, New York, 1991), Chap. 11, pp. 291–325.

22. C. M. Bender and S. A. Orszag, *Advanced Mathematical Methods for Scientists and Engineers* (McGraw-Hill, New York, 1978).

23. R. Ishizaki and K. Nishihara, Phys. Rev. Lett. **78**, 1920 (1997).

24. V. N. Goncharov, Phys. Rev. Lett. **82**, 2091 (1999).

25. S. J. Han and B. R. Suydam, Phys. Rev. A **26**, 926 (1982); A. I. Kleev and A. L. Velikovich, Plasma Phys. Control. Fusion **32**, 763 (1990).

26. S. Skupsky, R. W. Short, T. Kessler, R. S. Craxton, S. Letzring, and J. M. Soures, J. Appl. Phys. **66**, 3456 (1989).

27. T. J. B. Collins and S. Skupsky, Phys. Plasmas **9**, 275 (2002).

28. V. N. Goncharov, P. McKenty, S. Skupsky, R. Betti, R. L. McCrory, and C. Cherfils-Clérouin, Phys. Plasmas **7**, 5118 (2000).

High-Conversion-Efficiency Optical Parametric Chirped-Pulse Amplification System Using Spatiotemporally Shaped Pump Pulses

Since its invention in the early 1990s,[1] optical parametric chirped-pulse amplification (OPCPA) has become an attractive alternative to Ti:sapphire-based regenerative amplifiers for producing millijoule-level broadband laser pulses for injection of high-energy, short-pulse lasers that operate at a 1-μm wavelength.[2–4] The primary advantage of OPCPA is the fact that only a single pass through several (~3 to 7) centimeters of material is required to provide broadband pulse-amplification factors as large as 10^8 with little or no gain narrowing. Due to its single-pass nature, pulses amplified using OPCPA do not have the prepulses that are commonly associated with regenerative amplifiers, and the fact that a minimal amount of material is required means that there is little *B*-integral accumulation in the amplification process. It has been noted, however, that the pump-to-signal conversion efficiency of the OPCPA process can be quite poor, especially for systems pumped by commercial, *Q*-switched lasers, [5] Thus if several hundred millijoules of OPCPA output are desired at moderate repetition rates (1 to 10 Hz), pump lasers providing of the order of 5 J of energy at these repetition rates would be required. In addition, if high OPCPA output stability is also required, the fact that OPCPA involves a nonlinear amplification process means that the pump laser must also have very good energy stability.

One approach to overcoming these concerns is to use a pump laser that is better suited to the OPCPA process. Since this process involves no energy storage, the amplification factor for a pulse at a given temporal and spatial position is determined by the pump intensity at that particular spatiotemporal location. This has several implications: First, careful tailoring of the pump and seed spatiotemporal profiles is required to achieve high optical parametric amplification (OPA) conversion efficiency.[6,7] Second, even slight variations in the pump intensity can result in large amplification-factor fluctuations, potentially leading to significant spatial and spectral modulation and large overall energy fluctuations in the amplified broadband output pulse. It has been shown that, for a narrow range of pump intensities and a particular interaction length, saturation in the OPA process can be observed, reducing the amplification-factor fluctuations to a value similar to or lower than that of the pump.[8,9] As a consequence, in addition to careful design of the OPA itself, it is also important that the pump intensity profile be carefully controlled in both space and time to achieve efficient and stable operation of the parametric amplifier.

Much of the previous OPCPA work reported in the literature was conducted using pump lasers that offered limited control over the pumping pulse characteristics.[3,4,10,11] In this article, we experimentally demonstrate that improved control over the temporal and spatial profiles of the pump laser significantly increases the efficiency of the OPA process. We emphasize the temporal and spatial aspects of the pump that provide optimal pumping conditions, leading to both efficient and stable OPCPA output characteristics.

To optimize the OPCPA conversion efficiency and stability, a three-dimensional modeling code was developed that predicts the output of an OPCPA system given arbitrary pump and seed input energies and spatiotemporal profiles. This model, the details of which are described elsewhere,[12] was used to determine both the optimal pump spatiotemporal profile and the OPCPA configuration. Optimal conversion efficiency can be obtained with a uniform rate of energy transfer from the pump to the signal and idler, homogeneously depleting the pump in space and time. In our setup, a pump temporal profile that is flat in time with fast rise and fall times and a full width at half maximum (FWHM) that is roughly equivalent to that of the seed pulse is required. The spatial profile of the pump laser should be high-order super-Gaussian with a FWHM that is comparable to that of the seed pulse. As it is amplified, the originally Gaussian spatiotemporal profile of the seed is significantly sharpened due to the high gain of the OPA process. Thus when the amplification process begins to saturate, the spatiotemporal profiles of the seed and pump are well matched, improving energy extraction. Lithium triborate (LBO) was chosen as the OPA nonlinear medium because of its relatively high nonlinearity, high angular acceptance, and low walkoff between the pump beam (extraordinary wave) and the seed

beam (ordinary wave). The input pump intensity was limited primarily by the measured damage threshold of the antireflective coatings on the OPA crystals, so the model was used to select the crystal lengths that provided both high conversion efficiency and an amplified broadband pulse whose energy and spatial profile fluctuations were minimized.

A diagram of the experimental OPCPA setup is shown in Fig. 93.25. The OPA pump laser, shown in the shaded box, consists of a master oscillator, a temporal pulse-shaping system, a diode-pumped Nd:YLF regenerative amplifier, spatial beam shaping, a double-passed Nd:YLF power amplifier, and frequency doubling. The oscillator is a diode-pumped, single-longitudinal-mode Nd:YLF laser producing ~100-nJ pulses at 1.053 μm with a 300-Hz repetition rate.[13] The output of the oscillator is sent into an aperture-coupled-stripline (ACSL) temporal-pulse-shaping system, which can be configured to provide nearly arbitrary temporal pulse shapes for pulses up to 4 ns in duration.[14] The temporally shaped pulse is then amplified from ~50 pJ to 3 mJ in a diode-pumped, Nd:YLF regenerative amplifier.[15] The output of the regenerative amplifier is spatially expanded and apodized using a serrated-tooth apodizer to produce a 5-mm-FWHM beam that has a flat spatial profile at the output of the pump laser. The apodized pulse is then amplified from ~400 μJ to 40 mJ in a two-pass, flashlamp-pumped, 7-mm Nd:YLF power amplifier operating at 5 Hz. The output of the amplifier is relay imaged to a 3-mm beta-barium borate (BBO) frequency-doubling crystal, producing 526.5-nm pulses with energies as high as 25 mJ. A Pellin–Broca prism separates the second-harmonic light from the unconverted 1.053-μm light so that the latter does not serve as a seed for the OPA. The output of the BBO is then relay imaged to the OPA crystals.

As discussed above, optimizing the conversion efficiency of our OPCPA system requires a constant-intensity pump pulse with a temporal duration that is of the order of that of the seed. As shown in Fig. 93.26(a), temporally flat, 1-ns pulses with a 10 to 90 rise time of ~160 ps are produced at the output of the BBO doubling crystal. The time-integrated spatial profile of the pump laser, measured at the input to the OPA, is presented

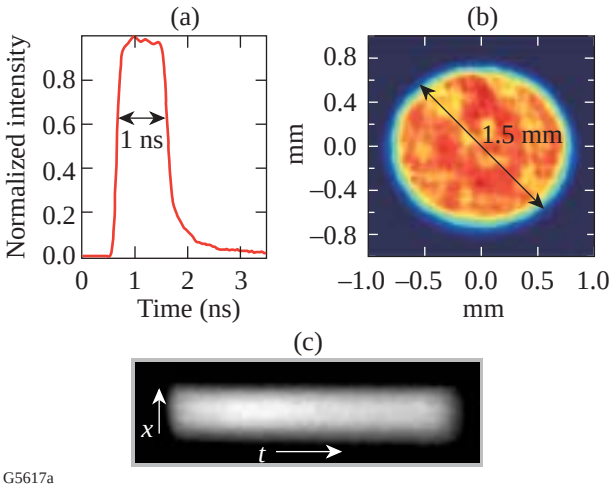

Figure 93.26
(a) 1-ns FWHM square temporal profile of the OPA pump laser; (b) spatial profile of the OPA pump laser; (c) streak camera measurement of the spatiotemporal profile of the pump showing little spatiotemporal coupling.

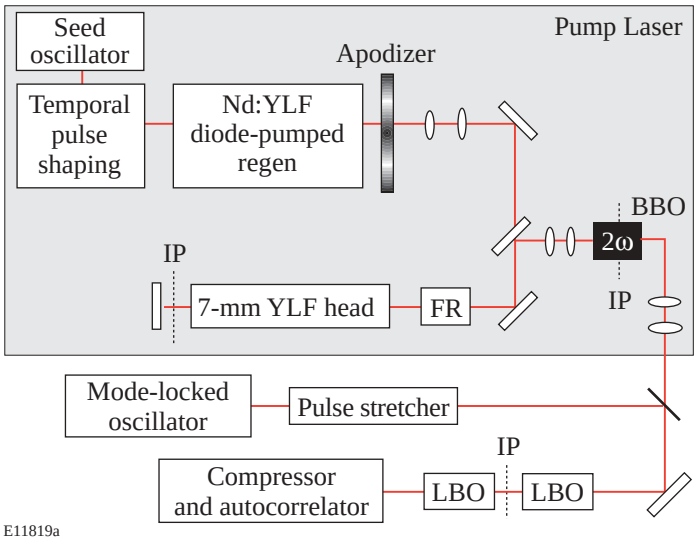

Figure 93.25
Diagram of the OPCPA experimental setup. The shaded box includes all of the components of the OPA pump laser. FR: Faraday rotator, IP: image plane; BBO: beta-barium borate; LBO: lithium triborate.

in Fig. 93.26(b). This beam has a tenth-order super-Gaussian spatial profile with a FWHM that is approximately equal to the spatial FWHM of the seed pulse. Because OPCPA is an instantaneous process, variations in the spatial profile of the pump over its temporal duration (spatiotemporal coupling) can lead to a reduction in conversion efficiency.[4] Figure 93.26(c) shows the spatiotemporal profile of the pump pulse as measured by a streak camera, demonstrating that there is no spatiotemporal coupling in the OPA pump pulse.

The broadband seed laser for the OPCPA system is a mode-locked, Nd:glass laser (Time-Bandwidth Products, Inc.) producing pulses with a center wavelength of 1.053 μm and a FWHM bandwidth of ~6 nm. The laser operates at a repetition rate of 76 MHz and is synchronized to an external master clock that also controls the OPA pump laser's master oscillator and pulse-shaping system. The jitter between the broadband seed and pump lasers, which can lead to output energy and temporal profile fluctuations, was measured to be less than 23 ps peak-to-valley and thus does not affect the stability of the OPCPA output. The 160-mW output of the seed laser is temporally stretched to ~700 ps in a double-passed, Öffner-triplet-based pulse stretcher,[16,17] providing ~800 pJ of seed energy at the OPA input with a Gaussian spatial and temporal profile.

The OPA consists of two wedged (2°), 5 × 5-mm-clear-aperture LBO crystals with lengths of 25 and 23 mm cut at 11.8° to allow type-I angular phase matching. The crystals have dielectric antireflective coatings provided by the vendor (Conex Systems, Inc.). The pump and temporally stretched seed beams have a FWHM of ~1.5 mm, providing a maximum pump intensity of ~1.1 GW/cm^2. The two LBO crystals are used in a walkoff-compensated configuration[18] with a ~4-mm air gap between them. This gap introduces a negligible amount of dephasing that does not affect the conversion process. The angle between the pump and seed pulses is 0.5°, which allows the signal and idler beams to be separated after the OPA process.

Figure 93.27 shows the conversion efficiency of the two-crystal OPCPA system as a function of pump energy. At maximum conversion efficiency, 17.7 mJ of pump energy produces 5.1 mJ of amplified signal energy, providing an overall gain of greater than 6×10^6 and a conversion efficiency of 29%. As demonstrated by the solid curve in Fig. 93.27, there is excellent agreement between modeling and experimental results. In addition to maximizing conversion efficiency, the OPCPA system was designed to minimize output-energy fluctuations. As shown in the inset table in Fig. 93.27, at the point of maximum conversion efficiency, the energy stability of the OPCPA output is 1.6% rms (measured over 100 shots) and is actually better than that of the pump. This improvement in output stability over that of the pump was predicted previously[8] and was achieved by carefully designing our OPA so that, at its output, energy in the signal just begins to reconvert into pump energy. We believe that this system demonstrates a significant improvement in output stability beyond systems previously reported in the literature.

The spectra of the input, stretched seed pulse and the amplified signal pulse are shown in Fig. 93.28(a). The FWHM of the amplified signal spectrum is approximately 8 nm, centered at ~1055 nm. Whereas the spectrum of the unamplified seed pulse is roughly Gaussian in shape, the shape of the amplified spectrum is square due to saturation in the OPCPA process. The amplified output of the OPCPA system is compressed in a double-passed, single-grating compressor.

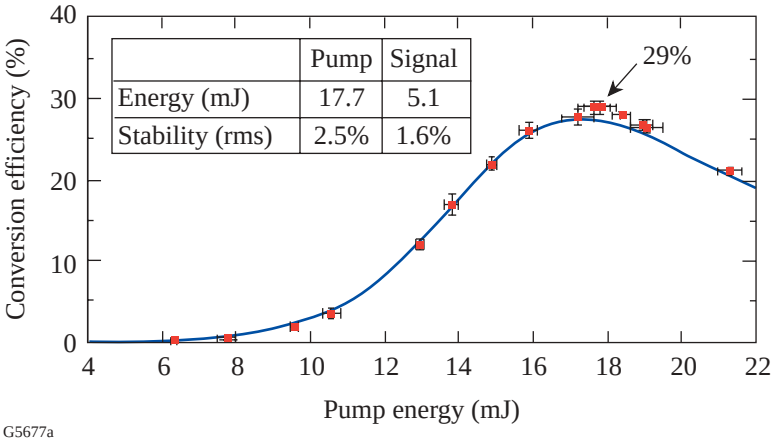

G5677a

Figure 93.27
Conversion efficiency as a function of pump energy. Solid curve shows model predictions with the squares representing experimentally measured values. Error bars show fluctuations in measured energies. Inset chart shows pump and signal energies and stabilities at the 29% conversion efficiency point.

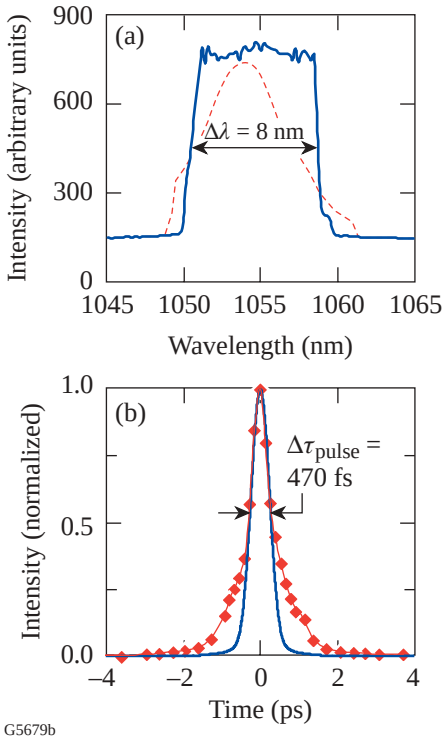

Figure 93.28
(a) Spectra of stretched seed pulse (dashed) and amplified signal pulse (solid). Clipping in the seed-pulse spectrum is due to the finite extent of the stretcher optics. (b) Measured autocorrelation (diamonds) of the amplified signal shown along with an autocorrelation trace (solid line) calculated from a fast Fourier transform (FFT) of the spectrum of the amplified signal shown in part (a). The wings in the measured autocorrelation are also present without OPCPA amplification, indicating that they are due to spectral phase errors in the stretcher–compressor combination.

The autocorrelation at the output of the pulse compressor, as measured with a scanning autocorrelator, is shown in Fig. 93.28(b). Using the measured spectra to estimate the transform-limited pulse width, we estimate the temporal duration (FWHM) of the compressed, amplified signal to be 470 fs, which is approximately 1.3 times the Fourier transform limit. Without amplification, the stretched and recompressed seed autocorrelation trace contains wings that are similar to those shown in Fig. 93.28(b). We thus believe that these wings are due to the uncompensated spectral phase in our stretcher–compressor combination and not the OPCPA process itself.

One of the advantages of an OPA is the fact that any aberrations in the pump spatial profile are transferred to the idler beam. Thus, the signal-beam quality is not degraded in the OPA. We measured the far field of our amplified signal beam at the focus of a 500-mm-focal-length lens with a 12-bit beam analyzer (Spiricon LBA 500PC and Cohu 4800 CCD camera). By comparing the FWHM of the Fourier transform of the measured near-field profile with that of the measured far field, we determined that the amplified-signal-beam FWHM is ~1.3 times the diffraction limit in the horizontal direction and ~1.1 times the diffraction-limited width in the vertical direction. These numbers match closely with those measured for the stretched seed pulse, indicating that the OPA did not introduce additional phase errors to the spatial profile of the amplified pulse.

The maximum pump-to-signal conversion efficiency possible in a degenerate OPA such as the one presented here is 50%. In our experiment, the conversion efficiency is limited by a number of factors including the finite slopes of the spatiotemporal profile of the pump pulse, walk-off between the seed and pump, and noise in the spatiotemporal profile. Our simulations show that if we are able to decrease the rise time of the temporal profile to ~50 ps and increase the order of the super-Gaussian spatial profile to 30, we could increase the conversion efficiency of our system to approximately 40%. We have also designed a new OPCPA system containing a two-crystal preamplifier and a single-crystal power amplifier that will be able to generate higher energies while increasing the overall system conversion efficiency to greater than 40%.[12]

We have demonstrated an OPCPA system that uses a spatiotemporally shaped pump pulse to maximize the conversion efficiency of the OPCPA process. This system produces 5 mJ of amplified signal at a 5-Hz repetition rate with a pump-to-signal conversion efficiency of 29%. To our knowledge, this is the highest conversion efficiency ever achieved in an OPCPA system. In addition to high conversion efficiency, the system output is highly stable with an rms stability of 1.6%, which is actually better than that of the pump laser.

ACKNOWLEDGMENT

This work was supported by the U. S. Department of Energy Office of Inertial Confinement Fusion under Cooperative Agreement No. DE-FC03-92SF19460, the University of Rochester, and the New York State Energy Research and Development Authority. The support of DOE does not constitute an endorsement by DOE of the views expressed in this article.

REFERENCES

1. A. Dubietis, G. Jonusauskas, and A. Piskarskas, Opt. Commun. **88**, 437 (1992).

2. I. N. Ross *et al.*, Opt. Commun. **144**, 125 (1997).

3. J. Collier *et al.*, Appl. Opt. **38**, 7486 (1999).

4. I. Jovanovic *et al.*, Appl. Opt. **41**, 2923 (2002).

5. I. Jovanovic, C. A. Ebbers, and C. P. J. Barty, Opt. Lett. **27**, 1622 (2002).

6. I. A. Begishev *et al.*, Sov. J. Quantum Electron. **20**, 1100 (1990).

7. I. A. Begishev *et al.*, Sov. J. Quantum Electron. **20**, 1104 (1990).

8. S. K. Zhang *et al.*, Opt. Commun. **184**, 451 (2000).

9. M. J. Guardalben, J. Keegan, L. J. Waxer, and J. D. Zuegel, presented at the 2002 OSA Annual Meeting, Orlando, FL, 29 September–3 October 2002 (paper TuC5).

10. I. N. Ross *et al.*, Appl. Opt. **39**, 2422 (2000).

11. X. Yang *et al.*, Opt. Lett. **27**, 1135 (2002).

12. M. J. Guardalben, J. Keegan, L. J. Waxer, and J. D. Zuegel, "Optimization of a High-Conversion-Efficiency Optical Parametric Chirped-Pulse Amplification System" (in preparation).

13. A. V. Okishev and W. Seka, IEEE J. Sel. Top. Quantum Electron. **3**, 59 (1997).

14. M. D. Skeldon, A. V. Okishev, R. L. Keck, W. Seka, and S. Letzring, in *Third International Conference on Solid State Lasers for Application to Inertial Confinement Fusion*, edited by W. H. Lowdermilk (SPIE, Bellingham, WA, 1999), Vol. 3492, pp. 131–135.

15. A. V. Okishev, D. Battaglia, I. Begishev, and J. D. Zuegel, in *OSA Trends in Optics and Photonics (TOPS) Vol. 73, Conference on Lasers and Electro-Optics*, OSA Technical Digest (Optical Society of America, Washington, DC, 2002), pp. 365–366.

16. G. Cheriaux *et al.*, Opt. Lett. **21**, 414 (1996).

17. D. Du *et al.*, Opt. Lett. **20**, 2114 (1995).

18. D. J. Armstrong *et al.*, J. Opt. Soc. Am. B **14**, 460 (1997).

Ultrafast Superconducting Single-Photon Optical Detectors and Their Applications

Introduction

Single-photon detectors (SPD's) represent the ultimate sensitivity limit for any quantum radiation detectors. In the visible light range, the best known and most widely used are Si avalanche photodiodes (APD's)[1] and photomultiplier tubes (PMT's).[2] The operation of photomultiplier/avalanche devices is based on the electron cascade and multiplication effect, which significantly amplifies the response and allows for an easy measurement of the response pulses. Unfortunately, this method of registration leads to a large time lag and jitter of the device response. In addition, the counting rates of APD's and PMT's are well below 100 MHz. Their actual speed is even more limited since, for noise reduction purposes, they have to be used in a time-gated mode, which reduces their counting rates to 10 MHz or below.

Detection of single-photon infrared (IR) radiation remains a major technological challenge because IR photons carry significantly less energy than those of visible light, making it difficult to engineer an efficient electron cascade. The most successful Si APD's have their sensitivity restricted by the band gap, while APD's based on narrow-gap semiconductors exhibit unacceptably large dark counts.[3] The best quantum efficiency (QE) reported for InGaAs APD's is ~16% at 1.2 μm, but the large, ~0.5-ns jitter and high, $>10^4$-per-second dark counts[3] make them unattractive for several important applications, including practical quantum communication systems.[2,4] The PMT's are bulky and demonstrate QE < 0.001% at 1.2 μm and ~150-ps jitter.[2] Finally, the most recently proposed far-IR detectors based on single-electron transistors[5] are very slow and require millikelvin temperatures.

In this article, we review our most recent research on superconducting SPD's (SSPD's). We demonstrate their excellent operating parameters and show that in many areas they drastically outperform their semiconductor counterparts. Applications ranging from visible free-space and IR fiber-based quantum communications[4] to nondestructive testing of very-large-scale-integrated (VLSI) devices[6] require SPD's with very high counting rates, very low jitter, and negligible dark counts. Effective operation in the mid-IR spectrum range is also very important. Our nanostructured, NbN SSPD's,[7,8] based on the nonequilibrium hot-electron effect in ultrathin superconducting films,[9] offer picosecond time resolution and jitter, experimental QE ranging from >10% for visible light to 5% to 3% in the 1.3-μm to 1.55-μm IR range, and very low dark counts.

The following sections will (1) present an overview of the physics of operation of SSPD's; (2) briefly discuss our fabrication methods; (3) present the experimental results and show the SSPD performance; (4) review already identified applications of SSPD's for VLSI chip testing and quantum cryptography; and (5) present our conclusions, including the direct comparison with other SPD's.

Physics of Operation of SSPD

Superconducting devices have already become practical as radiation sensors because of their quantum nature and low-noise cryogenic operation environment.[9] The superconducting energy gap 2Δ is typically two to three orders of magnitude lower than the gap in semiconductors; thus, individual optical photons are able to generate a large number of excited carriers when hitting a superconductor.[10] Measuring the resulting electrical pulse allows precise detection of the photon arrival. The efficient avalanche also results in an enhanced resolution of energy-resolving devices, such as superconducting tunnel junctions,[11] and extends the range of detectable energies well into the IR range for photodetectors. Finally, energy relaxation time constants of excited electrons in superconductors are in the picosecond range for both the low-temperature[12] and high-temperature[13] superconductors, ensuring the gigahertz repetition rates for superconducting photon counters.

Our SSPD consists of a superconducting stripe whose thickness is less than the electron thermalization length. The device is operated at a temperature far below the material's critical temperature T_c, in a regime where the bias current I is close to the critical value I_c. Absorption of a photon leads to

the formation of a hotspot region[14] where superconductivity is suppressed or even destroyed [Fig. 93.29(a)]. During the initial thermalization, the hotspot grows in size [Fig. 93.29(b)] as hot electrons diffuse out of the hotspot core. The supercurrent, which biases the device, is expelled from the resistive hotspot volume and is concentrated in the "sidewalks" near the edges of the film [Fig. 93.29(c)]. If the current density after this redistribution exceeds the critical value outside the hotspot, phase-slip centers are created in the sidewalks, the superconductivity is destroyed, and the resistive barrier is formed across the entire width of the device [Fig. 93.29(d)], which, in turn, gives rise to a voltage signal with the amplitude proportional to I. The hotspot growth is followed by its healing, due to the relaxation/cooling of excited electrons and their out-diffusion. Thus, after an ~30-ps-long quasiparticle relaxation time,[12] the hotspot collapses, superconductivity (zero voltage state) is restored, and the detector is ready to register another photon.

The SSPD operation principle outlined above depends directly on the superconductor characteristics, including 2Δ, diffusivity, electron–electron, and electron–phonon interaction times, as well as on the device geometry. Our material-of-choice is NbN, characterized by the picosecond quasiparticle relaxation; it is suitable for photon counting in the <0.4-μm- to 3.5-μm-wavelength range. Photons with a wavelength of 1 μm create in a 10-nm-thick NbN stripe a hotspot of ~20-nm diameter.[8] This means that the single-quantum mode of the SSPD operation requires that the width of our NbN superconductive stripe should be 200 nm or narrower.

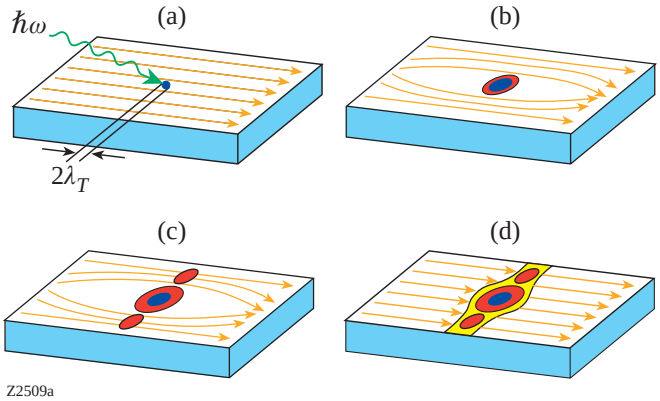

Figure 93.29
Schematics of the hotspot-generated and supercurrent-assisted formation of a resistive barrier in an ultrathin and submicrometer-width superconducting stripe, kept at a temperature far below T_c. The arrows indicate the flow direction of a supercurrent biasing the stripe.

SSPD Fabrication

NbN superconductive films that we use to fabricate our SSPD's have a thickness of 3.5 nm to 10 nm and are deposited on sapphire substrates by dc reactive magnetron sputtering in an Ar and N_2 mixture.[15] The films are characterized by T_c = 10 to 11 K, the superconductive transition width $\Delta T_c \sim 0.3$ K, and the critical current density $j_c = 6$ to 7×10^6 A/cm^2 at 4.2 K. To implement a detector, we have chosen meander-type geometry with characteristic sizes ranging from 10×10 μm^2 to 4×4 μm^2 and a filling factor f (the ratio of the area occupied by the superconducting meander to the detector nominal area) up to 0.5. The width of the superconductive stripe varies from 80 nm to 200 nm. Our patterning and etching procedures are presented in detail in Ref. 15; here we mention only that our fabrication process includes an electron-beam lithography, followed by either ion milling through a Ti mask layer or reactive ion etching through a photoresist.

Figures 93.30 and 93.31 present scanning electron microscope images of two SSPD's that are fabricated according to two different patterning procedures described in Ref 15. Figure 93.30 shows a 10×8-μm^2, 10-nm-thick meander device, fabricated using the Ti mask and ion milling. We note that in this technology, although we can fabricate devices with very narrow (0.1 μm to 0.2 μm in width) meander stripes, f is always much lower than 1, as the separation between the lines remains significantly larger than the line width. Figure 93.31 presents the center part of our latest-generation, interdigitated structures with f = 0.4 to 0.5, etched in a 3.5-nm-thick NbN film. Using ultrathin films and direct reactive ion etching, we

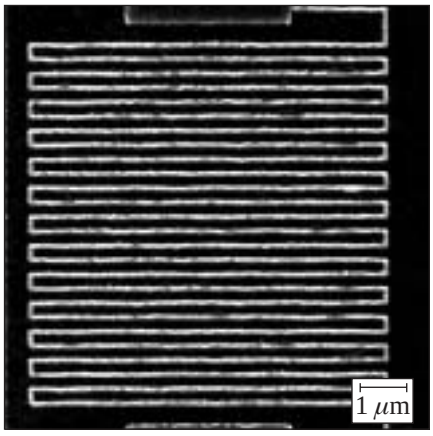

Figure 93.30
A scanning-electron-microscope image of a 10×8-μm^2, 10-nm-thick meander-type SSPD. The superconducting stripe width is ~130 nm and $f \approx 0.2$.

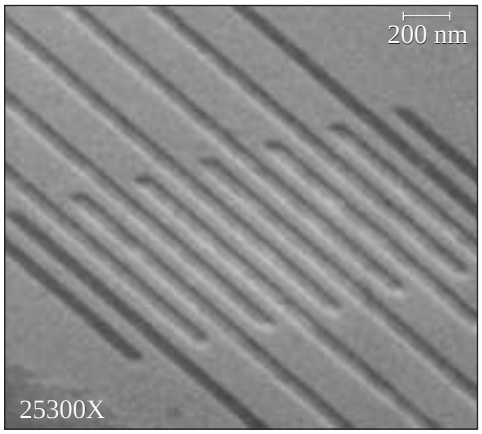

Figure 93.31
A scanning-electron-microscope image of an interdigitated, 3.5-nm-thick SSPD. The width of superconducting stripes (center of the picture) is ~80 nm and $f = 0.5$.

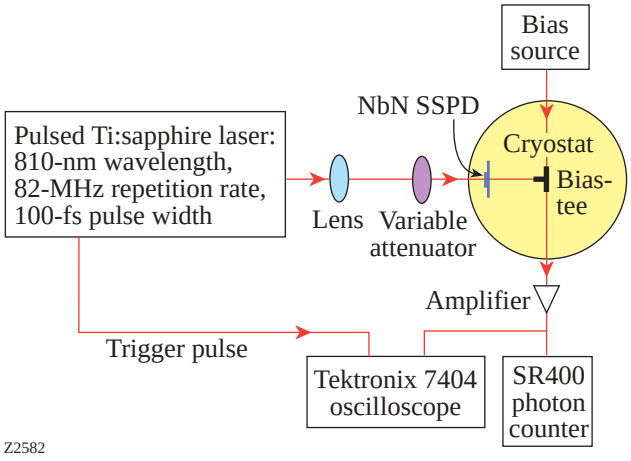

Figure 93.32
Experimental setup for free-space detection of single photons.

not only increased f but also drastically reduced our SSPD stripe edge nonuniformities. This latter factor seems to be dominant in the device performance since, as will be presented later, the 3.5-nm-thick structures exhibited over-an-order-of-magnitude-higher experimental QE, despite having significantly decreased the photon absorption coefficient η.[7]

Experimental Results and the SSPD Performance

A schematic diagram of our experimental setup is shown in Fig. 93.32. The SSPD was placed on a cold plate inside an optical, liquid-helium cryostat and maintained at 4.2 K. The device was wire bonded to a microstrip transmission line and connected to the dc bias and rf output circuitry via a broadband, cryogenic bias-tee. The output signal, generated as a result of the photon capture, was amplified by a 20-dB-gain, room-temperature broadband amplifier and either fed into a Tektronix 7404 single-shot digital oscilloscope (synchronously triggered by a Ti:sapphire laser) or counted by an SR400 photon counter. The room-temperature amplifier and the oscilloscope were characterized by a bandwidth of 0.01 to 12 GHz and 0 to 4 GHz, respectively.

As a photon source, we used 100-fs-wide, 82-MHz-repetition-rate pulses from a self-mode-locked Ti:sapphire laser. The incident radiation was focused on the device and attenuated to the picowatt level, using banks of neutral-density filters. The optical beam diameter was typically ~50 μm to ensure the SSPD uniform illumination. In addition, the QE spectral sensitivity dependence of the SSPD was measured using a continuous-wave (cw) blackbody radiation source and cw and pulsed laser diodes.

Figure 93.33 shows a collection of real-time "snapshots" recorded by the single-shot oscilloscope for different numbers of photons per laser pulse, incident on a 4×4-μm^2-area, 10-nm-thick SSPD, and is intended to illustrate the physical response of our devices. Each snapshot presents a 50-ns-long record of the response to four successive 100-fs-wide optical pulses, randomly selected out of a real-time detector output data stream. Trace (a) in Fig. 93.33 corresponds to essentially a macroscopic signal with ~20,000 photons per pulse hitting the detector. In this case, the device responded to each optical pulse in the laser train; however, as the incident laser intensity was decreased (with other experimental conditions unchanged), the quantum nature of the detector response started to emerge. For ~2400 photons per pulse [traces (b) and (c)], the amplitude of the response pulses was decreased, but, most interestingly, some of the signals were absent in the response train [trace (c)]. Further, over-an-order-of-magnitude decrease in the photon flux did not lead to the decrease of the output signal amplitude, which is characteristic of classical intensity detectors, but many of the response pulses were missing [trace (d)] due to both the limited QE of the device and fluctuations in the number of photons incident on the detector. The quantum nature of our device response was most apparent in the bottom pair of traces: (e) and (f) (1 photon/pulse). We note that

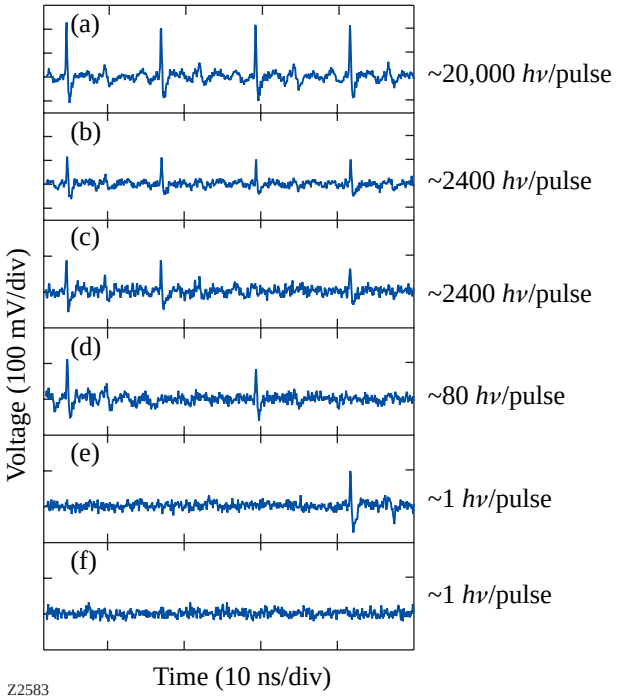

Figure 93.33
Real-time responses of a SSPD to trains of 100-fs optical pulses with different numbers of photons per pulse per device area. The presented records illustrate the quantum nature of our device responses at low photon fluxes. Radiation wavelength was 810 nm.

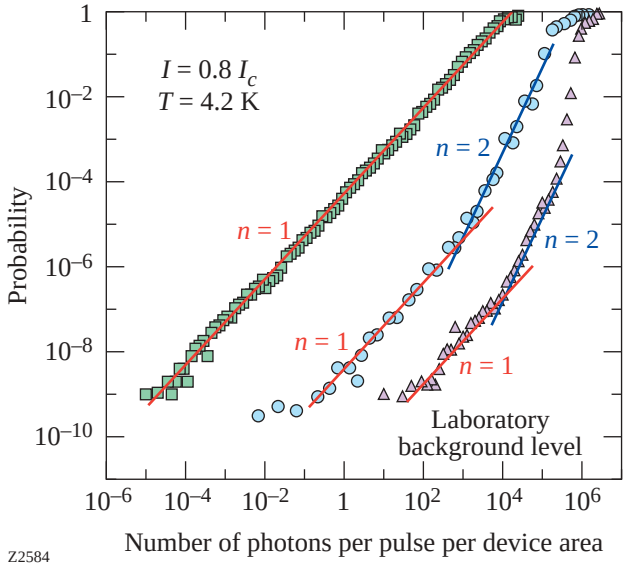

Figure 93.34
Probability of photon counting versus the incident photon radiation flux for a 10×10-μm^2, 10-nm-thick SSPD at 405-nm (squares), 810-nm (circles), and 1550-nm (triangles) wavelengths. The bias current was I/I_c = 0.8 and temperature was 4.2 K. The solid lines illustrate the slope exponents n = 1 and n = 2.

in each case, the detector response is very different and its actual performance has to be judged, based on the response averaged over the recording time much longer than 50 ns. We also note that within the time resolution of our electronics, the width of the SSPD response pulses remained constant for all tested photon fluxes.

Records like the ones shown in Fig. 93.33, but averaged over almost 5×10^9 optical pulses (accumulated over a period of 60 s using the SR400 counter), allowed us to perform statistical analysis of the SSPD response. We observed that for weak photon fluxes (<100 photons per pulse), both the average number of captured pulses for a given photon flux and the signal amplitude remained constant. Figure 93.34 shows the probability of photon counting (the ratio of the average number of photons captured per second to the repetition rate of laser pulses) as a function of the average number per pulse of 405-nm, 810-nm, and 1550-nm photons from our Ti: sapphire laser, incident on a 10×10-μm^2-area, 10-nm-thick device. The device was biased at I = 0.8 I_c, which was low enough to remain subcritical even when I_c was thermally suppressed at the highest incident light intensities. We note that for 405-nm photons we have a linear dependence over ten orders of magnitude of the photon flux intensity. At wavelength λ = 810 nm, we observe the linear response at low photon counts and the quadratic law for higher photon fluxes. Finally, for λ = 1550 nm, the photon counting rate is a highly nonlinear function of the photon flux, with the linear dependence observed only in the range of 10^2 to 10^4 photons per pulse. We also observe that for the lowest photon fluxes, our experimental data points, for every wavelength, level off at the same ~10^{-9} probability value (~0.1 counts per second). We interpret this response as the laboratory photon background, resulting from accidental photon absorption by our detector. On the other hand, the saturation (probability approaching 1) observed at the highest incident photon flux levels represents the transition of our quantum device into a classical detector [see also Fig. 93.33(a)].

SSPD's are passive devices, and the main sources of dark or false counts are either extrinsic bias-current instabilities or intrinsic fluctuations. The supercurrent fluctuations are dominating at I very close to I_c and rapidly (exponentially) decrease with the I decrease,[16] while thermally activated phase-slip centers are typically negligible since we operate our devices at $T << T_c$. Thus, long-term stability of I when the detector is biased close to I_c is crucial for minimizing dark counts. One

must remember, however, that SSPD's are very broadband sensors and they have to be properly screened from unwanted "photon noise." Large values of dark counts were observed in SSPD implementations, where thermal background radiation from room-temperature objects was inadvertently coupled into the detector.[6] Measurements of dark counts performed in the setup shown in Fig. 93.32 with the SSPD blocked by a cold load lead to an average of <0.01 counts per second for $I \leq 0.95\, I_c$ and were, apparently, limited by our biasing electronics.

The behavior observed in Fig. 93.34 results from the direct linear dependence of the hotspot size on the photon energy.[8] Thus, for a fixed I, low-energy photons generate hotspots too small to ensure efficient SSPD operation, leading to enhanced probability of multiphoton detection with the increase of the photon flux.

For a mean number of m photons per pulse, the probability $P(n)$ of absorbing n photons from a given pulse is given by the Poisson distribution:

$$P(n) \sim \frac{e^{-m}(m)^n}{n!}. \tag{1}$$

For very weak ($m << 1$) photon fluxes, the probability of detecting one photon, two photons, three photons, etc., is

$$P(1) \sim m,\ P(2) \sim \frac{m^2}{2},\ P(3) \sim \frac{m^3}{6},\ \text{etc.} \tag{2}$$

Based on Eq. (2), we can conclude that for a very low number of photons per pulse incident on the SSPD, we clearly observe in Fig. 93.34 a single-photon detection regime (exponent $n = 1$) for each studied wavelength. While for 405-nm radiation, the presence of at least one photon in the optical pulse was sufficient to trigger the detector response, for $\lambda =$ 1550 nm, the multiphoton absorption ($n \geq 2$) was dominant.

The probability of photon counting measured at the one-photon-per-pulse level incident upon the SSPD and expressed in percent can be defined as its *experimental* QE [more rigorously: detection efficiency (DE)] for a given photon energy. We must stress that QE is a function of I and the highest values are measured for I very close to I_c as shown in Refs. 8 and 16. Typically, we operate our SSPD's with $I \leq 0.95\, I_c$ since, as we mentioned before, higher I values result in excessive dark counts. Figure 93.35 presents experimental QE spectral dependence for two representative 10 × 10-μm^2-area devices. The 3.5-nm-thick SSPD (squares) was an interdigitated device (see Fig. 93.31) with 80-nm-wide NbN fingers and $f = 0.5$, while the 10-nm-thick, 200-nm-wide-stripe SSPD (triangles) was a meander-type structure (see Fig. 93.30) with $f \approx 0.2$. We observe that in both cases, the DE spectral dependence exhibited an exponential, activated-type character with the slope value characteristic for all devices with the same thickness.[8] We associate the activation-type behavior with the presence of fluctuations, both extrinsic (stripe width) and intrinsic (superconducting). Simultaneously, we note the drastic improvement in the performance of the 3.5-nm-thick device, as compared to the 10-nm structure, in terms of both the much smaller slope value and the much higher experimental QE.[16]

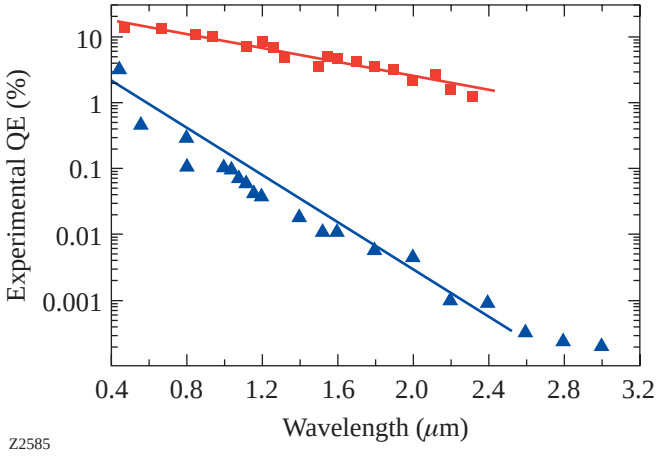

Figure 93.35
Spectral dependences of QE for 10 × 10-μm^2 SSPD's, with NbN stripe thickness of 10 nm (triangles) and 3.5 nm (squares), respectively. The solid lines are guides to the eye, illustrating the exponential dependence of the QE on wavelength.

As we mentioned in the **SSPD Fabrication** section, this performance improvement is the result of significant improvements in our fabrication technology.[15] The interdigitated devices implement the ultrathin NbN stripe (larger hotspot dimension) and are truly nanostructured in terms of their physical dimensions. Our best 10-nm-thick SSPD's exhibit experimental QE of ~3% at $\lambda = 405$ nm, decreasing to ~0.01% at $\lambda = 1550$-nm wavelength. At the same time, the 3.5-nm devices reach over-an-order-of-magnitude-higher QE, ranging from >10% at $\lambda = 405$ nm to 3.5% at $\lambda = 1550$ nm.

Proper coupling of our devices to the incident photon flux is another, besides I, limiting factor of the SSPD's experimental QE value. Unlike semiconductor SPD's, the SSPD's have a

relatively small active area, and only a certain percentage of incident photons is actually absorbed in the ultrathin NbN stripe. The above limitations are extrinsic; thus, in order to estimate the SSPD ultimate performance, defined as the *intrinsic* QE of the superconducting stripe,[7,8] one needs to factor in both the filling factor and the photon absorption coefficient. For 10-nm-thick devices, $f \approx 0.2$ and $\eta \approx 0.3$, leading to the intrinsic QE = DE/($f\eta$), indicating that the possible improvement can reach up to a factor of 20. In the case of the 3.5-nm SSPD's, similar calculations indicate that the intrinsic QE should reach the theoretical maximum of 100% for all visible-light wavelengths. The above approach is questionable, however, since for our ultrathin, nanostructured devices, the NbN optical conductivity can be quite different from the dc value used in Eq. (1) in Ref. 7 to calculate η. The best approach to further increase the QE of our detectors is, we believe, not by changing the interdigitated SSPD geometry, but by adding a backside mirror to reflect the transmitted photons back into the detector. It would be even more effective to form a $\lambda/4$ resonator with the detector acting as one of the resonator mirrors. In this case, however, the SSPD would loose its broadband sensitivity.

Finally, one can define a *system* QE as the number of photons falling at input on the fiber or other coupling optics, divided by the number of photon counts recorded by the detector. This QE definition includes the impact of the detector coupling optics rather than the SSPD size, and it was used in Ref. 6 to describe the performance of the early SSPD-based system designed for noninvasive testing of the VLSI chips. The system QE value reported in Ref. 6 for one of the first 10-nm-thick, meander-type SSPD's was 0.002% at 1.3-μm wavelength. The latest 3.5-nm devices in the same fiber-based system (although with significantly modified/improved optics) exhibit a system QE of 2% at the same wavelength—a four-orders-of-magnitude improvement over a two-year period.

We have also performed extensive time-domain characterization of our SSPD's, which are presented in Ref. 17. Here we want only to mention that the 10-nm-thick SSPD's have a time resolution <100 ps and a device jitter <35 ps. Thus, they are able to detect photons with at least 10-Gbit/s counting rate and are more than three orders of magnitude faster than any semiconductor SPD. The 3.5-nm devices are expected to have even better time resolution, reaching values close to the intrinsic electron–phonon cooling time in ultrathin NbN films of 30 ps.[12] Their jitter has been already measured and is below 20 ps.

Applications of SSPD's

1. Noncontact VLSI Chip Testing

Modern, high-performance, electronic VLSI circuits are extremely difficult to test on both the functional and logic levels because of their complexity, density of packaging, and the use of flip-chip bonding. Devices are increasingly more sensitive and can be easily perturbed during testing, skewing results and slowing the design and development time. Thus, in complex circuits such as microprocessors, nonperturbing methods of testing the chip functionality while it operates are most desirable.

A normally operating silicon complementary metal oxide semiconductor (CMOS) transistor has a nonzero probability of emitting near-IR (0.9 μm to 1.4 μm) photons when current passes through the channel. This is the spontaneous photon emission associated with intraband transitions as the hot carriers move across the transistor channel.[18,19] Thus, this photon emission is time-correlated with the transistor switching event and measures directly the transistor switching time, as well as the entire circuit timing characteristics. This intrinsic transistor/circuit information is ideal for timing data acquisition and fault analysis (e.g., leaky transistors tend to emit more photons). The use of near-IR emission from CMOS integrated circuits as a way of diagnosing timing and flaws of VLSI chips has been implemented in the IDS PICA probe system, manufactured by NPTest, San Jose, CA. The IDS PICA system can be equipped with an imaging near-IR detector, the Mepsicron II PMT (Quantar Tech., Inc) or with the SSPD device.[6] The imaging PMT camera enables light emission from many devices on a test circuit to be simultaneously analyzed, but its IR efficiency is extremely low, leading to hour-long acquisition times and poor noise-to-signal ratio. The SSPD can analyze emission from a single CMOS device only, but its superior IR QE cuts acquisition times to minutes or seconds.

The 3.5-nm-thick NbN SSPD sensors are currently being implemented in the latest IDS PICA version. Test results from a 0.18-μm-linewidth, 1.6-V-bias CMOS integrated circuit running at 100 MHz are shown in Fig. 93.36. The collected histogram has an extremely high signal-to-noise ratio and the time between transistor switching events can be measured with 10-ps accuracy. In addition to the peaks coming from photon emission from nMOS transistors, we can also observe weak signals collected from pMOS inverters. Holes in pMOS devices have lower mobility and emit IR photons much less frequently. We need to stress that the integrated circuit under test and the photon-collecting microscope are at room tem-

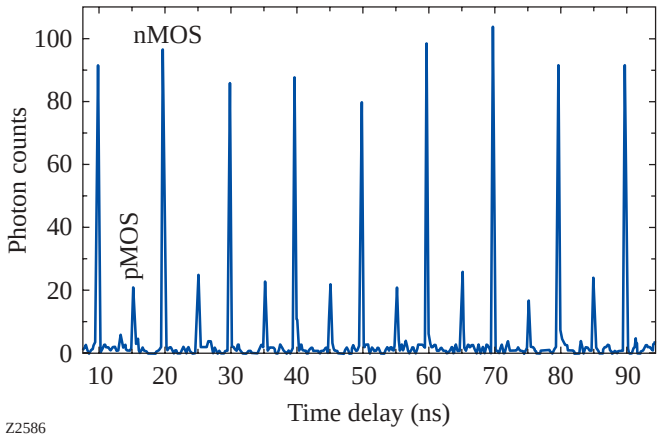

Figure 93.36
Histogram of single-photon emissions from a CMOS VLSI chip, collected by the NbN SSPD. Signals from both nMOS and pMOS transistors are clearly visible. The picture was copied directly from the PICA screen.

perature, and the microscope is connected to the SSPD via a multimode fiber. Physically, the chip-testing apparatus is approximately 2 to 3 m away from the detector, which is placed inside a commercial cryocooler, operating at 3.5 K.

2. Quantum Cryptography

Quantum cryptography (QC) provides a radical improvement over today's methods for secure communications. Unconditionally secret communication is possible in actual physical environments due to the Heisenberg indeterminacy principle: it is impossible to measure the state of a quantum bit without altering it. In QC, the data transport is performed as an exchange of individual photons with their polarization used to code the logic information for the communication protocol. QC is based on the real-time Vernam encryption scheme (so-called "one-time pad").[20] The quantum key is formed during the photon transmission (there is no pre-existing key), and the Vernam cipher is invulnerable to any computer attack of any strength, including quantum computations.

A recent theoretical paper by Gilbert and Hamrick[21] proves that QC is practical, providing that the data transmission rate is high enough to overcome the intrinsic system losses. Both the transceiver (Alice) and the receiver (Bob) must operate at transmission rates of at least 1 Gbit/s for the practical quantum key distribution operation. A GHz-repetition-rate, actively mode-locked laser can be used as the high-speed source of coherent single photons,[22] so Alice can readily operate at the GHz range. A serious problem, however, exists at the Bob end, which should count photons not only very efficiently, but also with negligible dark counts and very low jitter.

Figure 93.37 presents a possible QC receiver, containing four SSPD's for independent counting of photons with four different polarizations imprinted by Alice. The NbN SSPD's are the most promising for practical QC since, as we have already presented, they exhibit sufficiently high QE and are able to reach GHz-range counting rates with very low jitter and negligibly low dark counts. The SSPD's can successfully operate from ultraviolet to IR; thus, they can be implemented in both optical free-space and fiber-based transmission schemes.

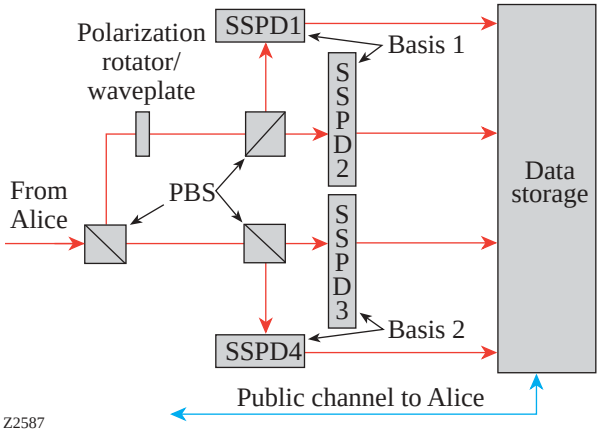

Figure 93.37
Quantum cryptography receiver (Bob) based on four NbN SSPD's. PBS stands for polarization beamsplitter.

Conclusions

Table 93.II presents the main characteristics of our SSPD's, in direct comparison with other modern single-photon detectors. Experimental QE, ultimate counting rate, jitter, and dark counting rates are compared for 1.3-μm photons, which is the most-interesting wavelength for applications ranging from noninvasive VLSI chip testing to fiber-based optical communications. As can be seen, superconducting detectors significantly outperform even the best semiconductor devices.

ACKNOWLEDGMENT

This work was supported by the AFOSR grant F49620-01-1-0463 (Rochester), by RFBR grant 02-02-16774 (Moscow), and by NPTest, San Jose, CA. The authors would like to thank their colleagues from the University of Rochester, Moscow State Pedagogical University, and NPTest for their contributions to the SSPD research. We are also very grateful to Dr. Deborah Van Vechten and the U.S. Office of Naval Research for fostering the Rochester–Moscow collaboration.

Table 93.II: Performance of different SPD's operating at $\lambda = 1.3\ \mu$m.

Detector Model	Counting Rate	QE	Jitter	Dark Counts
	(Hz)	(%)	(ps)	(s^{-1})
InGaAs APD (Fujitsu)	5.0×10^6 [(a)]	16	200	500 [(b)]
IR PMT (Hammamatsu)	9.0×10^6	0.5	150	2.0×10^4
Si APD (EG&G)	5.0×10^6	0.01	350	25
Mepsicron (Quantar, Inc.)	1.0×10^6 [(c)]	0.001	100	0.1
Superconducting tunnel junction	5.0×10^3	60	N/A	N/A
SSPD (measured)	10×10^9	5	35	0.1[(d)]
SSPD (projected)	30×10^9	>10	<20	<0.01

[(a)]Gated regime with 0.1%-per-gate after-count probability.
[(b)]Calculated with 10^{-4}-per-gate probability.
[(c)]Data for a high-speed version; standard devices exhibit $1 \times 10^5\ s^{-1}$.
[(d)]Room-temperature input.

REFERENCES

1. T. Isoshima *et al.*, Rev. Sci. Instrum. **66**, 2922 (1995).
2. A. Karlsson *et al.*, IEEE Circuits and Devices Mag. **15**, 34 (1999).
3. F. Zappa *et al.*, Opt. Eng. **35**, 938 (1996).
4. A. A. Verevkin, J. Zhang, W. Slysz, R. Sobolewski, A. P. Lipatov, O. Okunev, G. Chulkova, A. Korneev, and G. N. Gol'tsman, in *Free-Space Laser Communication and Laser Imaging II*, edited by J. C. Ricklin and D. G. Voelz (SPIE, Bellingham, WA, 2002), Vol. 4821, pp. 447–454.
5. O. Astafiev *et al.*, Appl. Phys. Lett. **80**, 4250 (2002).
6. S. Somani, S. Kasapi, K. Wilsher, W. Lo, R. Sobolewski, and G. Gol'tsman, J. Vac. Sci. Technol. B, Microelectron. Nanometer Struct. **19**, 2766 (2001).
7. G. N. Gol'tsman, O. Okunev, G. Chulkova, A. Lipatov, A. Semenov, K. Smirnov, B. Voronov, A. Dzardanov, C. Williams, and R. Sobolewski, Appl. Phys. Lett. **79**, 705 (2001).
8. A. Verevkin, J. Zhang, R. Sobolewski, A. Lipatov, O. Okunev, G. Chulkova, A. Korneev, K. Smirnov, G. N. Gol'tsman, and A. Semenov, Appl. Phys. Lett. **80**, 4687 (2002).
9. A. D. Semenov, G. N. Gol'tsman, and R. Sobolewski, Supercond. Sci. Technol. **15**, R1 (2002).
10. K. S. Il'in, I. I. Milostnaya, A. A. Verevkin, G. N. Gol'tsman, E. M. Gershenzon, and R. Sobolewski, Appl. Phys. Lett. **73**, 3938 (1998).
11. A. Peacock *et al.*, Nature **381**, 135 (1996); R. J. Schoelkopf *et al.*, IEEE Trans. Appl. Supercond. **9**, 2935 (1999).
12. K. S. Il'in, M. Lindgren, M. Currie, A. D. Semenov, G. N. Gol'tsman, R. Sobolewski, S. I. Cherednichenko, and E. M. Gershenzon, Appl. Phys. Lett. **76**, 2752 (2000).
13. M. Lindgren, M. Currie, C. Williams, T. Y. Hsiang, P. M. Fauchet, R. Sobolewski, S. H. Moffat, R. A. Hughes, J. S. Preston, and F. A. Hegmann, Appl. Phys. Lett. **74**, 853 (1999).
14. A. M. Kadin and M. W. Johnson, Appl. Phys. Lett. **69**, 3938 (1996).
15. G. N. Gol'tsman, K. Smirnov, P. Kouminov, B. Voronov, N. Kaurova, V. Drakinsky, J. Zhang, A. Verevkin, and R. Sobolewski, "Fabrication of Nanostructured Superconducting Single-Photon Detectors," to be published in IEEE Transactions on Applied Superconductivity.
16. A. Lipatov, O. Okunev, K. Smirnov, G. Chulkova, A. Korneev, P. Kouminov, G. Gol'tsman, J. Zhang, W. Slysz, A. Verevkin, and R. Sobolewski, Supercond. Sci. Technol. **15**, 1689 (2002).
17. J. Zhang, W. Slysz, A. Verevkin, G. Chulkova, A. Korneev, A. Lipatov, O. Okunev, G. Gol'tsman, and R. Sobolewski, "Response Time Characterization of NbN Superconducting Single-Photon Detectors," to be published in IEEE Transactions on Applied Superconductivity.
18. J. C. Tsang and J. A. Kash, Appl. Phys. Lett. **70**, 889 (1997).
19. M. Pavesi *et al.*, Phys. Rev. B **65**, 195209 (2002).
20. G. S. Vernam, J. Amer. Inst. Elec. Eng. **XLV**, 109 (1926).
21. G. Gilbert and M. Hamrick, "Practical Quantum Cryptography: A Comprehensive Analysis (Part One)," MITRE Technical Report MTR00W0000052 (September 2000), http://xxx.lanl.gov/abs/quant-ph/0009027; also to be published in Physics Reports.
22. T. R. Clark *et al.*, Electron. Lett. **35**, 720 (1999).

Very Fast Metal–Semiconductor–Metal Ultraviolet Photodiodes on GaN with Submicron Finger Width

Metal–semiconductor–metal (MSM) photodiodes made on GaN are attractive candidates for fast ultraviolet (UV) signals due to the simplicity of fabrication and the visible blind feature (no response for $\lambda > 365$ nm). The temporal response of a MSM photodetector fabricated on GaN has been examined both theoretically[1] and experimentally.[2–4] While the theoretical modeling for a 0.25-μm MSM interdigitated structure predicted a small time constant of 3.5 ps, experimental measurements have been limited to feature dimensions no smaller than 2 μm. More recently T. Palacios *et al.*[5] reported on the responsivity of submicron (0.5-μm) MSM UV detectors on GaN; however, the temporal response was not characterized. In this article, we present the results of temporal measurements of a MSM photodiode on GaN with finger width and pitch ranging from 0.3 μm to 5 μm. These detectors were packaged with a specially designed fast circuit. The minimum temporal resolution between consecutive optical pulses was measured to be 26 ps. At high illumination levels, broadening of the detector response was observed and can be attributed to space-charge screening.

The GaN wafers (2-μm thickness) grown on *c*-plane sapphire were purchased from Technologies and Devices International, Inc.[6] The residual impurities produced a free-electron concentration below 1×10^{16} cm^{-3}. The MSM detectors were fabricated at Cornell Nanofabrication Facilities (CNF) using electron-beam lithography. A 15-nm Au layer was deposited prior to the exposure of the electron beam due to the low conductivity of the material. Native oxide on the surface was removed with a diluted HF (hydrofluoric acid) solution prior to metallization, Ti/Pt (5 nm/80 nm). The finger spacing and width, which were equal, ranged from 0.3 μm to 5 μm. The active area was either 50×50 μm^2 or 25×25 μm^2. After fabrication of the fingers, a FOx-12 (field oxide) negative resist layer with 450-nm thickness was deposited and exposed with the *e* beam to form a SiO_2 passivation layer over the entire device.

Unlike other high-speed measurements that used microwave techniques,[7,8] our time-domain experiments used a broadband circuit to directly couple out the electrical pulse generated in the active area. The top view of this fixture is shown in Fig. 93.38. The backside of the circuit board is grounded. The transmission line width was designed to be 1.1 mm to match the 50-Ω impedance of the 34-GHz digitizing oscilloscope. A large bias resistor R_c was used to block out reflections from the charging circuit. To avoid an abrupt width change, a pad with a curved taper, calculated[9] to reduce the impedance mismatch between the transmission line and the active area, was fabricated on the device. An ultrabroadband (12 KHz to 40+ GHz) optical capacitor ("Opt-Cap" in Fig. 93.38) is soldered on the edge of the board to produce a high-speed electrical connection to the backside ground plane. The sample is glued on the gap between the transmission line and the Opt-Cap and electrically connected by silver paste. The impulse response of the whole detector was simulated numerically.[10]

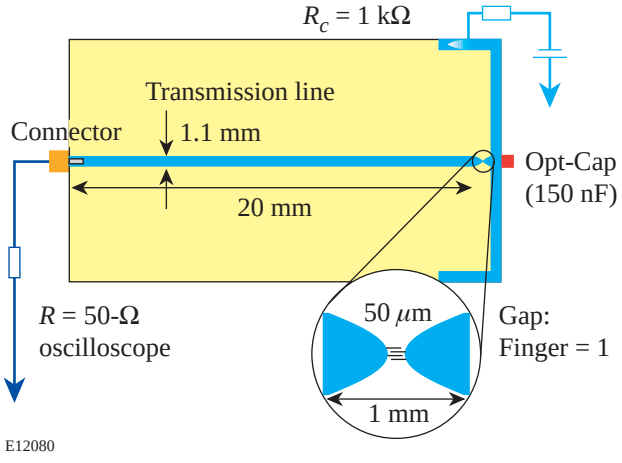

Figure 93.38
Top view of the broadband circuit designed for the MSM photodetector. R_c (1 kΩ) isolates the electrical pulse from bias circuit. An ultrabroadband optical capacitor (Opt-Cap) was soldered to the device and the ground. To avoid an abrupt width change, a pad with a calculated curve tapers the transmission line down to the active area.

The temporal response measurement was implemented with a mode-locked Ti:sapphire laser ($\lambda \sim 810$ nm). The output of the femtosecond laser was coupled into a custom-built third-harmonic generator to produce a UV beam ($\lambda \sim 270$ nm). The beam was then focused onto the active area of the sample by a UV-grade fused-silica lens with a 2-cm focal length. The focal spot was measured to be smaller than 10 μm. The electrical pulse was displayed on a 34-GHz digital oscilloscope and recorded by a computer.

The device was plugged directly into the oscilloscope to eliminate the dispersion from connecting cables. Figure 93.39 is a plot of the normalized signal from devices with different fingers widths (0.3 μm, 2 μm, and 5 μm) under 5-V bias. The curves have been shifted in time for visual convenience. The optical energy is about 6 pJ/pulse. The main peaks are followed by ringing reflections from the circuit. It is interesting to compare our data on the 5 μm with those in Ref. 2: they reported a full width at half maximum (FWHM) of longer than 100 ps at 5-V bias, almost twice the pulse duration we measured. The slower response was attributed[2] to carrier transit time, which is contradicted by our experiments.

Further, our data show that the fall time is even faster than the rise time for all the samples at low illumination level, and the FWHM's of the impulse response from different fingers (60 ps for 0.3 μm, 54 ps for 2 μm, and 58 ps for 5 μm) are similar (Fig. 93.39).

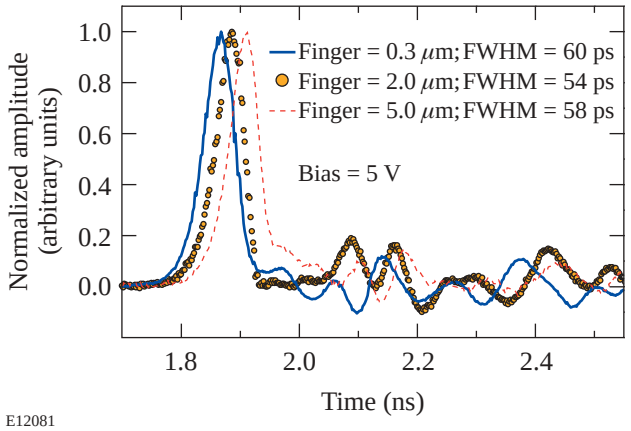

Figure 93.39
Time response of the detectors with different fingers (0.3 μm, 2 μm, and 5 μm) under 5-V bias. The amplitudes of the signal have been normalized to the peak values, and the dc background has been subtracted.

To study the relationship between electric field and temporal response time, we changed the bias voltage from 1 V to 10 V while maintaining the same illumination level. The pulse durations remained essentially the same. Another sample, with a 0.3-μm finger spacing and a 25×25-μm^2 active area, was examined. Its FWHM was measured at 58 ps, almost the same as the larger samples, thus eliminating device capacitance as the dominant factor contributing to the pulse width. This led us to examine the measurement test fixture, including the silver paste, the discontinuity of the connector, the surface roughness, and the width variation of the transmission line. The combined effect could cause the charging and discharging of the device to experience different impedances. For the device with 0.3 μm, using reflection (ringing) in the response signal, which is 12% of the peak, we estimate the discharging impedance to be 63 Ω. If the charging time is determined by the Z_C = 63 Ω and discharging time is determined by oscilloscope impedance, 50 Ω, the ratio of them should be 63:50 = 1.26. This matches well with the experimental results of 58-ps rise time and 45-ps fall time. Overall we believe that at a low illumination level the very short electrical pulse generated in our detectors was broadened by the measurement system and the real impulse response of the samples should be faster than the measured pulse duration.

To explore further the inherent device response, a split-beam technique was used. In these experiments, the UV beam was split into two parts with an adjustable delay. The two pulses were then used to excite the detector. Figure 93.40 shows the results of the double-pulse measurement for a device with 0.3-μm finger and 25×25-μm^2 active area at 5-V bias. Separable responses began to be discernible at a time delay of 26 ps. This indicates that our devices had an inherent response time of less than 26 ps. When one optical pulse was delayed by 54 ps, the two pulses were well resolved: the value of the valley was about 70% of the value of the peak. This is consistent with our measured pulse duration. If delayed further to 90 ps, the two pulses were clearly separated, as can be seen in the plot.

The power dependence of the response speed was studied by tuning the UV output from the custom-built tripling system from 3 pJ to 391 pJ. In Fig. 93.41 we plot the temporal response data of a sample with 0.3-μm finger width for optical pulse energies of 3, 116, and 391 pJ, respectively. Again the signal amplitudes have been normalized to their peak values. The applied bias is 5 V for all measurements. As the incident optical energy increases, the rise time remains almost constant; however, the fall time increases significantly. This is attributed

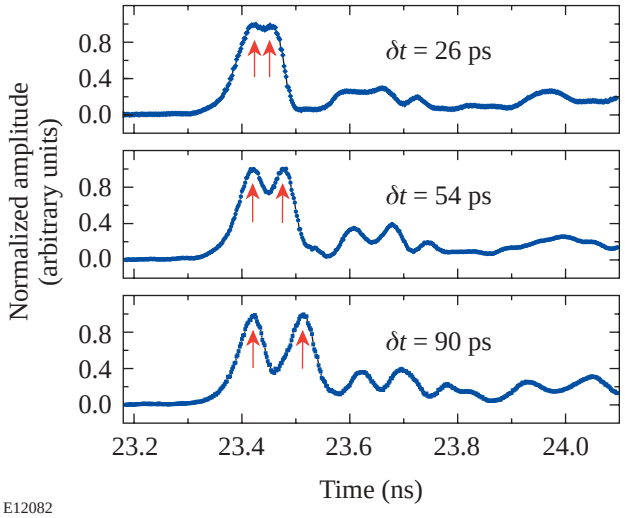

Figure 93.40
Time resolution of the detector in free space. The beam was split into two parts, and one of them was delayed. When the delay was 26 ps, two main peaks started to be discernable. The reflections of the circuit can also be clearly seen.

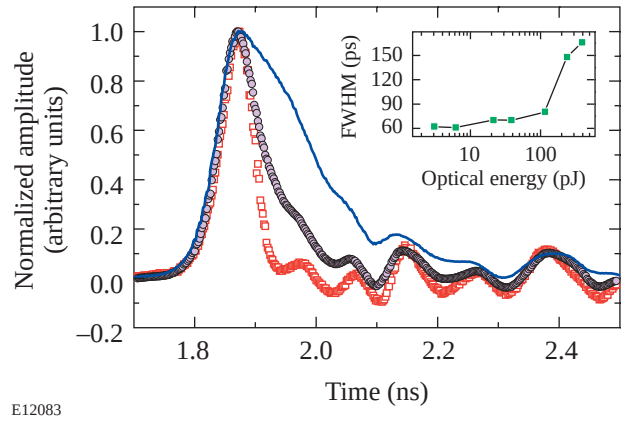

Figure 93.41
Impulse response of MSM devices under different illumination energies of 3 pJ (squares), 116 pJ (circles), and 391 pJ (solid line). The insert shows the dependence of pulse width on the incident optical energy. The pulse duration remains constant below 6 pJ.

to screening of the internal field (dark electric field) between the finger electrodes by the space-charge field created by the field-induced separation of photogenerated electrons and hole at high illumination conditions.[9,11,12] The measured FWHM's under a different optical energy are plotted in the inset of Fig. 93.41. As can be seen, the FWHM remains flat (60 ps) for optical energy up to 6 pJ, after which the FWHM increases by approximately 10 ps up to 110 pJ and then to 166 ps for optical energy of 391 pJ. The condition on which the space-charge effect does not affect the pulse shape of impulse response was calculated in Refs. 11 and 12 and given as

$$E < \frac{\varepsilon_0(\varepsilon_s + 1)L^2 V(t + D)hc}{4\lambda q t^2 (1 - r)[1 - \exp(-\alpha d)]}, \quad (1)$$

where E is the incident optical pulse energy, ε_s is the relative permittivity of the semiconductor, L^2 is the active area, V is the applied bias, t is the finger width, D is the interelectrode spacing, λ is the incident wavelength, r is the reflection coefficient, α is the optical absorption coefficient, and d is the thickness of the GaN film. Based on all the parameters used in fabrication and experiment, we obtained a pulse energy of 6.54 pJ for our devices. This is in close agreement with our experimental results (FWHM starts increasing after 6 pJ).

In summary, MSM photodiodes have been fabricated on GaN with finger width and pitch ranging from 0.3 μm to 5 μm, and the impulse responses have been measured at λ = 270 nm under both low and high illumination conditions with a fast, broadband circuit. For an optical pulse energy less than 6 pJ, the response speed of the detectors was about 60 ps, regardless of the bias voltages (up to 10 V) and finger dimensions. Analysis of the rise and fall times indicates that the very short photogenerated electric pulse was broadened by the measurement system. The inherent device response was determined to be less than 26 ps by the double-pulse measurements. At higher incident optical energies, the pulse width increased significantly due to the screening of the dark electric field between the finger electrodes. The experimental results are in close agreement with theory.

ACKNOWLEDGMENT

One of the authors (JL) thanks Ms. Lu Chen for her help at CNF. This work was supported by the U.S. Department of Energy Office of Inertial Confinement Fusion under Cooperative Agreement No. DE-FC03-92SF19460, the University of Rochester, and the New York State Energy Research and Development Authority. The support of DOE does not constitute an endorsement by DOE of the views expressed in this article.

REFERENCES

1. R. P. Joshi, A. N. Dharamsi, and J. McAdoo, Appl. Phys. Lett. **64**, 3611 (1994).
2. J. C. Carrano *et al.*, J. Electron. Mater. **28**, 325 (1999).
3. J. C. Carrano *et al.*, Appl. Phys. Lett. **73**, 2405 (1998).
4. D. Walker *et al.*, Appl. Phys. Lett. **74**, 762 (1999).
5. T. Palacios *et al.*, Appl. Phys. Lett. **81**, 1902 (2002).
6. TDI, Inc., Silver Spring, MD 20904.
7. B. C. Wadell, *Transmission Line Design Handbook* (Artech House, Boston, 1991).
8. N. Biyikli *et al.*, Appl. Phys. Lett. **79**, 2838 (2001).
9. K. Aliberti *et al.*, Appl. Phys. Lett. **80**, 2848 (2002).
10. The details will be reported in a subsequent publication.
11. S. V. Averine and R. Sachot, Solid-State Electron. **44**, 1627 (2000).
12. S. V. Averine and R. Sachot, IEE Proc., Optoelectron. **147**, 145 (2000).

Glassy Liquid Crystals for Tunable Reflective Coloration

Amorphous Molecular Glasses

Glasses have been in existence for thousands of years, and yet they still represent one of the frontiers in materials science today.[1] They are traditionally classified as amorphous solids exhibiting isotropic properties. Cooled at a sufficiently rapid rate, all liquids should bypass crystallization to form glass. It is well known that liquid viscosity increases exponentially with decreasing temperature. Phenomenologically, the glass transition temperature T_g is defined on the basis of viscosity reaching a value of 10^{13} poise.[2] Despite intensive efforts over several decades, understanding of molecular processes accompanying glass transition has remained largely qualitative.[1,2]

Glassy films are characterized by their superior optical quality over a large area with no grain boundaries and, therefore, are ideally suited for electronics, optics, photonics, and optoelectronics.[3] Glass formation is ubiquitous among polymeric materials. To take advantage of the ease of film processing due to low melt viscosity and the feasibility of vacuum deposition, considerable efforts have been devoted in recent years to developing low-molar-mass organic materials. Existing amorphous molecular glasses can be categorized as follows: (a) bulky, odd-shaped or twin molecules;[4–6] (b) starburst molecules and dendrimers;[7–9] (c) spiro-linked molecules;[10–12] and (d) tetrahedrally configured molecules.[13] In general, an elevated T_g relative to the application temperature is desired for stability against recrystallization. Representative structures are presented in Fig. 93.42, where *G x*°C *I* expresses a T_g at *x*°C.

Glassy Liquid Crystals

It is arguable that glasses are not necessarily amorphous or isotropic. In principle, mesomorphic organic glasses can be realized by vitrifying liquid crystals through thermal quenching. Liquid crystals are a class of self-organizing fluids characterized by a uniaxial, lamellar, helical, or columnar arrangement in nematic, smectic, cholesteric, and discotic liquid crystalline order,[14] respectively, as depicted in Fig. 93.43.

Each type of liquid crystal has found its respective niche in optics, photonics, or optoelectronics. With these molecular arrangements frozen in the solid state, glassy liquid crystals (GLC's) represent a novel material class that combines properties intrinsic to liquid crystals with those common to polymers, such as glass transition and film- and fiber-forming abilities. The preparation of defect-free GLC films requires

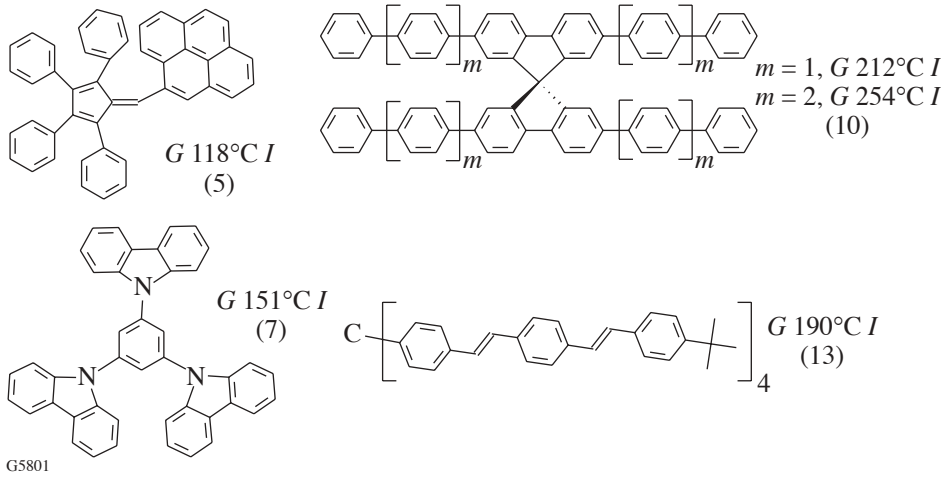

Figure 93.42
Representative amorphous molecular glasses.

slow cooling from mesomorphic melts without encountering crystallization, a challenge to thermal quenching as a conventional means to vitrification. From a fundamental perspective, transition of liquid crystal into mesomorphic solid adds a new dimension to the traditional view of transition from isotropic liquid into isotropic solid. The differential scanning calorimetric thermograms compiled in Fig. 93.44 serve to distinguish a GLC from a conventional liquid crystal.

Heating a conventional liquid crystal causes a first-order transition from crystalline solid to liquid crystal at its melting point T_m followed by a transition into isotropic liquid at its clearing point T_c. In contrast, a stable GLC undergoes a second-order transition from mesomorphic solid into liquid crystal at T_g, without modifying the molecular order, followed by a transition into isotropic liquid at T_c. Intermediate between a conventional liquid crystal and a stable GLC lies an unstable GLC, which tends to recrystallize from mesomorphic melt above T_g upon heating with subsequent melting to liquid crystal at T_m and clearing at T_c. Empirically, T_g/T_m was found to fall between 2/3 and 3/4 on an absolute temperature scale.

The very first attempt to synthesize GLC's in 1971 yielded materials with a low T_g and poor morphological stability.[15] In parallel to low-molar-mass GLC's, liquid crystalline polymers have been explored for the past three decades.[16–18] In essence, GLC's are advantageous in their superior chemical purity and favorable rheological properties.[19] Existing GLC's can be categorized into (a) laterally or terminally branched, one-string compounds with a T_g mostly around room temperature;[20] (b) twin molecules with an above-ambient T_g, but generally lacking morphological stability;[21–24] (c) cyclosiloxanes functionalized with mesogenic and chiral pendants;[25–27] (d) carbosilane dendrimers exhibiting a low T_g,[28–30] and (e) macrocarbocycles with mesogenic segments as part of the ring structure.[31]

Representative structures are presented in Fig. 93.45, where *G x*°C *Nm* or *Ch y*°C *I* expresses a T_g and a T_c (for a nematic or cholesteric to isotropic transition) at *x* and *y*°C, respectively. Based on the previously reported structures, there does not seem to be a systematic approach to the design of glassy liquid crystals. Specifically, the structural factors determining the type of mesomorphism, T_g and T_c, and the stability against recrystallization from the glassy state have remained largely elusive. Glassy cholesteric liquid crystals capable of selective wavelength reflection are of particular interest because of the relevance to tunable reflective coloration.

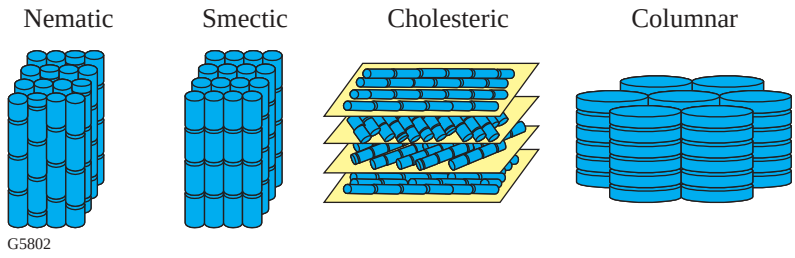

Figure 93.43
Liquid crystalline order via molecular self-organization.

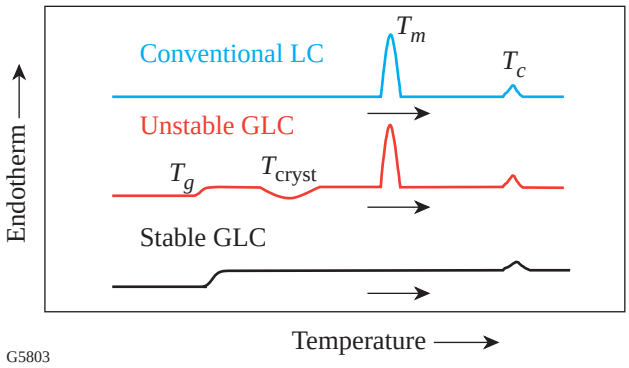

Figure 93.44
DSC thermograms of liquid crystals.

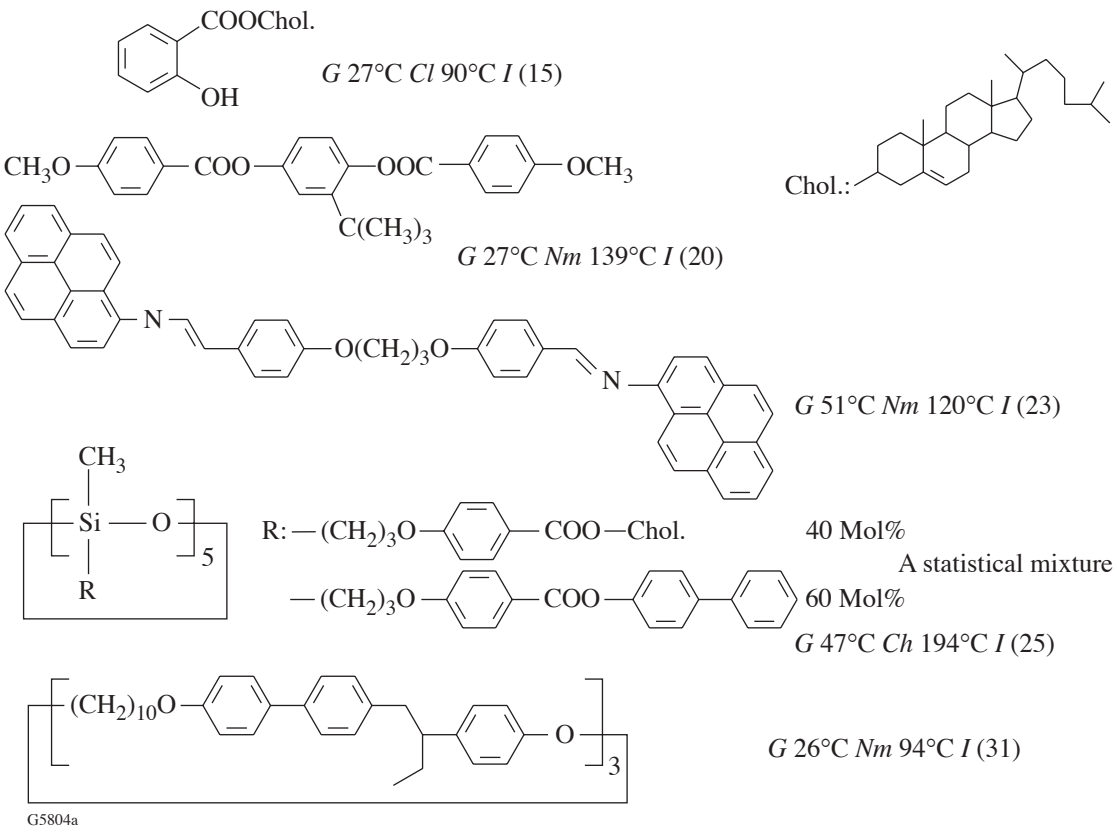

Figure 93.45
Representative glassy liquid crystals reported previously.

Optical Properties of Cholesteric Liquid Crystal Films

A cholesteric liquid crystal contains both nematic and chiral moieties in a single molecular entity or as a binary mixture. Consisting of a helical stack of quasinematic layers, a well-aligned cholesteric film can be characterized by handedness and helical pitch length p, as depicted in Fig. 93.46.

Handedness describes the direction in which twisting of the nematic director occurs from one layer to the next, and p is defined as the distance over which the director rotates by 360°. The property of selective reflection can be described in terms of $\lambda_R = p(n_e + n_o)/2$, in which n_e and n_o are the extraordinary and ordinary refractive indices of the quasi-nematic

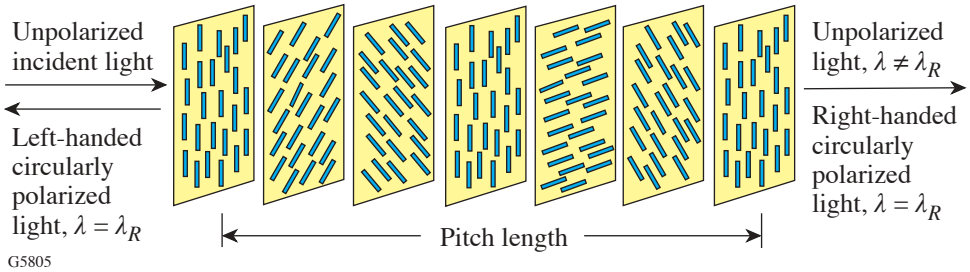

Figure 93.46
Selective reflection by a left-handed cholesteric film.[32]

layer, respectively. The other parameter of interest is the helical twisting power, a measure of the ability of a chiral moiety to generate a given helical pitch length. Let us consider incident unpolarized white light propagating through a left-handed film as illustrated in Fig. 93.46. Natural (i.e., unpolarized) light consists of equal amounts of left- and right-handed (LH and RH) circularly polarized components. The LH circularly polarized component in the neighborhood of λ_R is selectively reflected, while the RH component is completely transmitted. The selective reflection bandwidth is determined by optical birefringence, $\Delta n = n_e - n_o$. A sufficiently thick, single-handed cholesteric film is capable of reflecting 50% of incident unpolarized light within the selective reflection band. Outside the selective reflection band, incident light is transmitted regardless of its polarization state. It follows that a stack of RH and LH films tuned at the same λ_R will reflect 100% of incident unpolarized light within the selective reflection band without attenuating the rest of the spectrum.

A New Approach to Glassy Liquid Crystals with Elevated Phase Transition Temperatures and Superior Morphological Stability

Most existing liquid crystals tend to crystallize when cooled to below their melting points, thus losing the desired molecular order characteristic of liquid crystals and resulting in polycrystalline films that scatter light or limit charge transport. As an emerging class of advanced materials, GLC's preserve varied forms of molecular order characteristic of liquid crystals in the solid state. To prevent spontaneous crystallization, we have implemented a molecular design strategy in which mesogenic and chiral pendants are chemically bonded to a volume-excluding core. While the core and the pendant are crystalline as separate entities, the chemical hybrid with a proper flexible spacer connecting the two readily vitrifies into a GLC when cooled. A definitive set of GLC's has been synthesized and characterized[33–43] as summarized in Fig. 93.47, where *G x*°C (*Nm*, S_A, or *Ch*) *y*°C *I* expresses a T_g and a T_c (for a nematic,

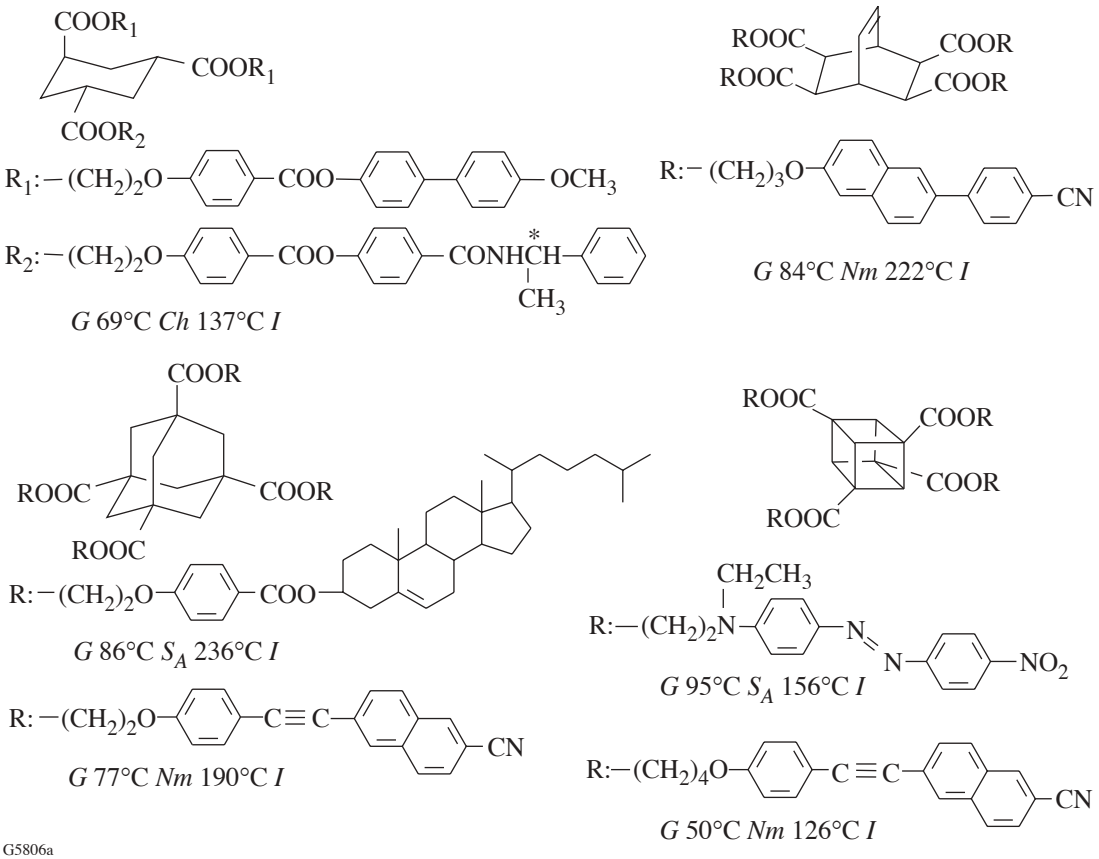

Figure 93.47
Representative morphologically stable glassy liquid crystals.

smectic A, or cholesteric to isotropic transition) at x and y°C, respectively. Cyclohexane, bicyclooctene, adamantine, and cubane serve as the cores to which nematic and chiral pendants are attached, a manifestation of the versatility of our design concept. A spacer length of two to four methylene units was found to be optimum for vitrification with an elevated T_g.

Major advances have been made recently using a cyanoterphenyl nematogen, with an exceptionally high T_m and T_c, in the construction of GLC's with substantially elevated transition temperatures without compromising morphological stability. Note the glassy nematics with a T_g close to 130°C and a T_c close to 350°C,[44] the highest values ever achieved in GLC's. As shown in Fig. 93.48, a linear nematogen is superior to an angular one in terms of phase transition temperatures. Glassy cholesterics have been synthesized in the past via a statistical approach, which requires intensive purification of a multicomponent reaction product.[45] A deterministic synthesis strategy, as described in Reaction Scheme 1, produced enantiomeric glassy cholesterics with an identical molecular structure except opposite chirality.[46]

The mixture of (I) and (II) in Reaction Scheme 1 at a mass ratio of 42 to 58 showed a T_g at 67 and a T_c at 131°C. The polarization spectra of single-handed glassy cholesteric films are shown in Fig. 93.49. An unpolarized incident beam is decomposed into two circularly polarized components of equal intensities propagating in opposite directions. Since handedness of circularly polarized light can be reversed via reflection from a specular surface, essentially 100% circular polarization of an unpolarized light source can be accomplished. An optical notch filter consisting of a stack of glassy cholesteric films of opposite handedness is shown in Fig. 93.49 to yield an attenuation of 3.75 optical density units, equivalent to a contrast ratio of better than 5000 to 1, representing the best performance of organic materials to date. The spectral range intended for

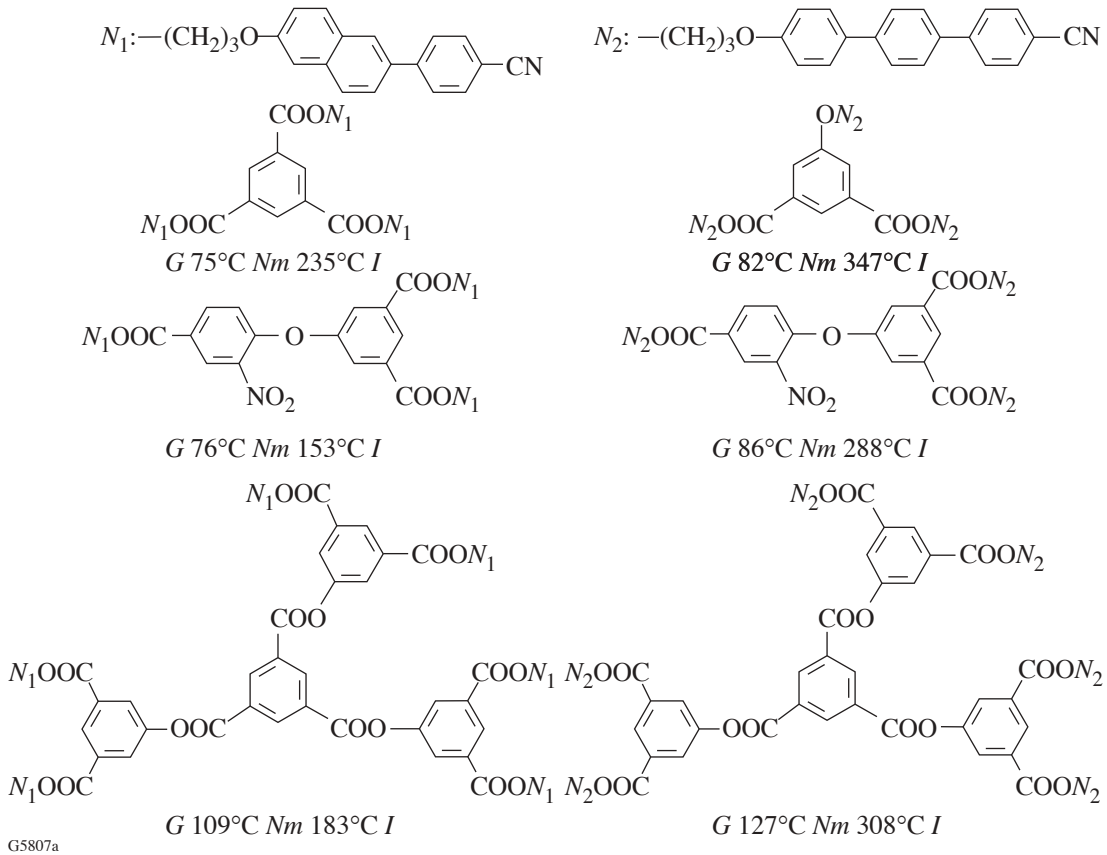

Figure 93.48
High-temperature glassy nematics.

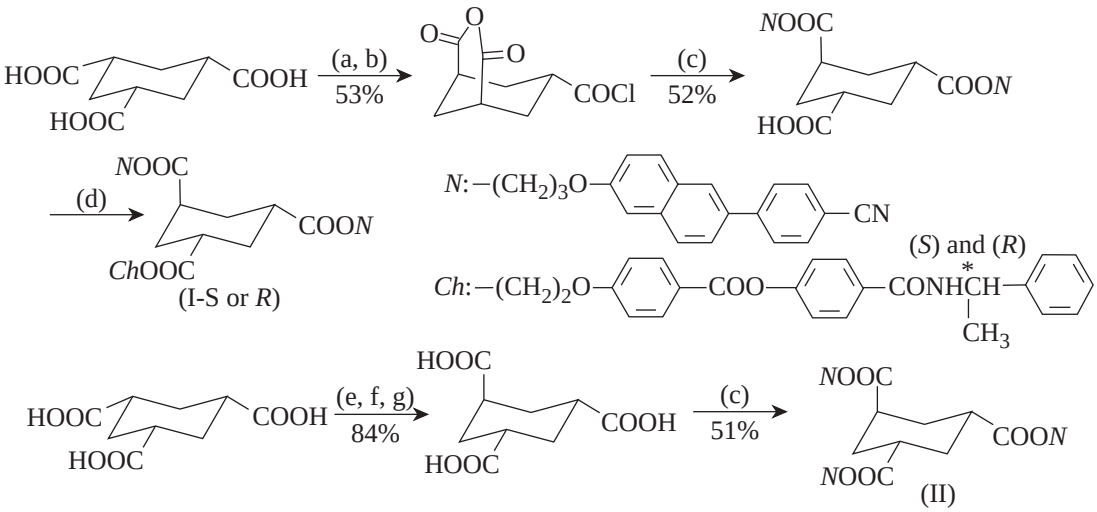

Reaction Scheme 1
Deterministic synthesis of glassy cholesterics.

(a) $(CH_3CO)_2O$/reflux; (b) $SOCl_2$/reflux; (c) *N*OH/DMAP/Et_3N; (d) *Ch*OH/DEADC/PPh_3;
(e) $(CH_3CO)_2O$, CH_3CO_2Na; (f) CH_3COCl; (g) H_2O
DMAP: 4-(dimethylamino)pyridine; DEADC: diethyl azodicarboxylate; PPh_3: triphenylphosphune

G5808

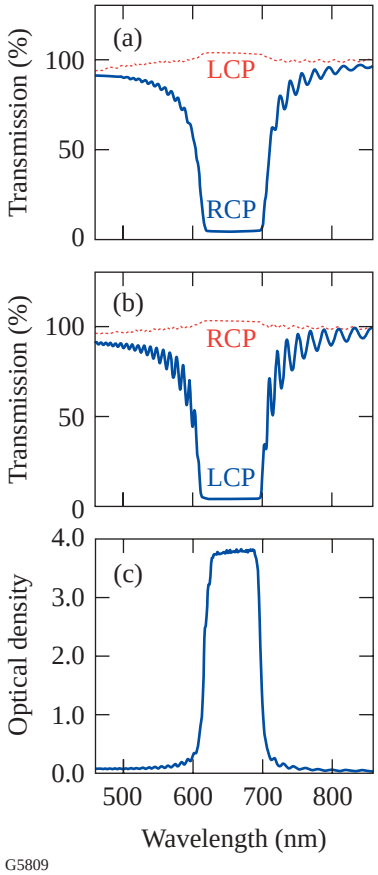

G5809

Figure 93.49
Optical spectra of an unpolarized beam through (a) a right-handed, (b) a left-handed glassy cholesteric film, and (c) a notch filter comprising the two single-handed films (reproduced with permission from Ref. 46; copyright 2000 Wiley-VCH).

polarization and reflection can be readily tuned by varying the chemical composition.

The cyanoterphenyl group has also been successfully implemented in high-temperature glassy cholesterics synthesized in a deterministic fashion using the 5-oxyisophthalate linking unit, as shown in Fig. 93.50. Note that *G x*°C *Ch y*°C *I* expresses a T_g and a T_c (for cholesteric to isotropic transition) at *x* and *y*°C, respectively, determined from a differential scanning calorimetry (DSC) heating scan. The DSC cooling scan is presented as *I w*°C *Ch z*°C *G*, indicating a T_c (for isotropic to cholesteric transition) and a T_g at *w* and *z*°C, respectively.

Tunable Reflective Coloration by Glassy Cholesteric Films

Two distinct modes of coloration exist in nature: *pigmentary*, involving electronic transitions of chromophores underlying light absorption and emission; and *structural*, involving interference, diffraction, or scattering of ambient light by nanostructures.[47] Examples of structural colors include butterfly wings, bird feathers, and beetle cuticles. In particular, beetles' exocuticles resemble cholesteric liquid crystalline films capable of selective wavelength reflection with simultaneous circular polarization, giving rise to long-lasting brilliant colors. A wide variety of cholesteric liquid crystalline materials have been developed, such as low-viscosity liquids, lyotropic and thermotropic polymers, liquid crystal/polymer composites, and glassy liquid crystals. Of particular interest are glassy liquid crystals that resist spontaneous crystallization through heating-cooling cycles, such as mixtures of Compounds (III) and (IV) depicted in Fig. 93.51. Although (IV) crystallizes upon heating to 95°C, both (III) and its binary mixtures with (IV) form stable glassy cholesteric films.[45] Also shown in Fig. 93.51 are the selective reflection bands ranging from blue to green, red, and the infrared region with mixtures at an increasing ratio of (IV) to (III).

Furthermore, the selective reflection band and its width were shown to be tunable, albeit irreversibly, via photoracemization of a bridged binaphthyl dopant.[48] In particular, phototunability is demonstrated in Fig. 93.52, where UV irradiation of a cholesteric film at a temperature above its T_g (i.e., 120°C versus 68°C) over an increasing time period followed by cooling to room temperature is shown to result in an increasing selective reflection wavelength. Morphologically stable GLC's that resist crystallization upon heating and cooling are the key to the successful implementation of this device concept.

Reversible Tunability of Reflective Coloration

Reversible tunability of reflective coloration has been extensively explored with temperature, pressure, electric field, and light as the external stimuli.[49–57] The approach based on photoisomerization appears to be the most promising. The concept was first demonstrated by Sackman,[54] and revisited recently by Ikeda *et al*.,[55] based on *cis*-to-*trans* isomerization of azobenzene dopants in cholesteric fluid films. Shibaev *et al*.[56] employed a chiral azobenzene, both as a dopant and as a comonomer, in a polymer system with an ambient T_g and a response time of tens of minutes. Tamaoki *et al*.[57] used a glassy cholesteric matrix containing an azobenzene dopant, a material system allowing for photomodulation of pitch length at temperatures above T_g followed by cooling to below T_g to preserve the modified pitch in the solid state. All these approaches employing azobenzenes to tune reflective coloration suffer from fatigue and thermally activated *cis*-to-*trans* isomerization. Photoinduced interconversion between nematic and

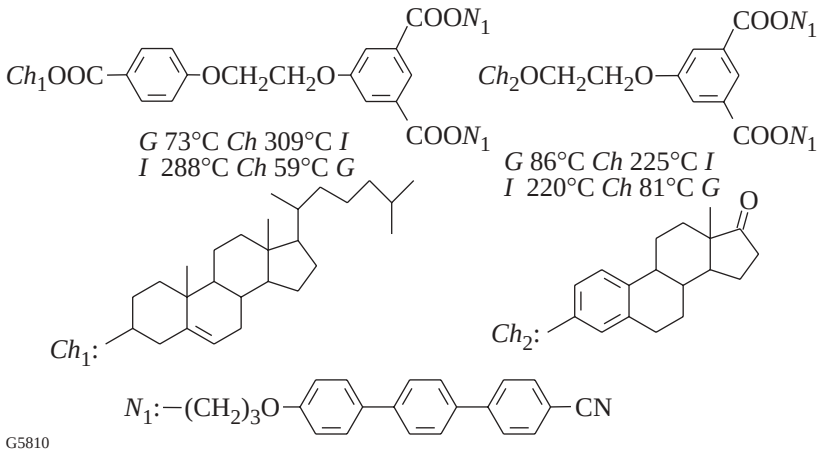

Figure 93.50
High-temperature glassy cholesterics.

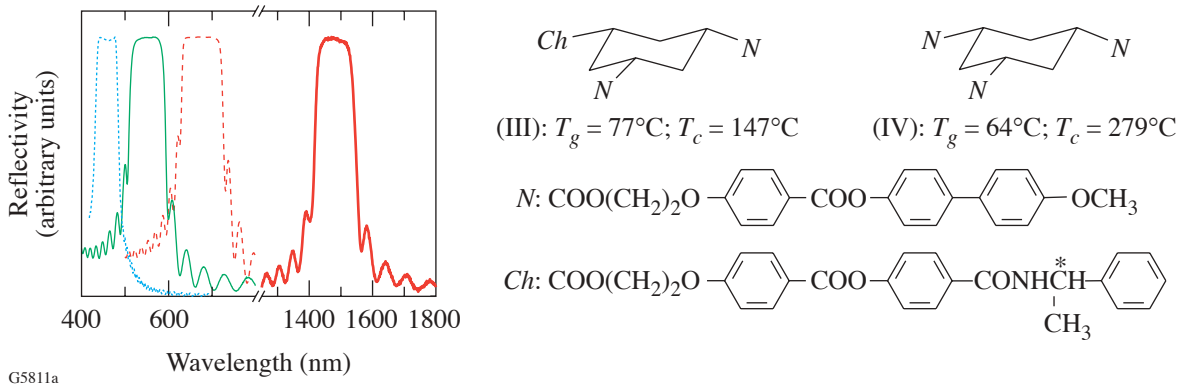

Figure 93.51
Reflective coloration by glassy cholesteric films.

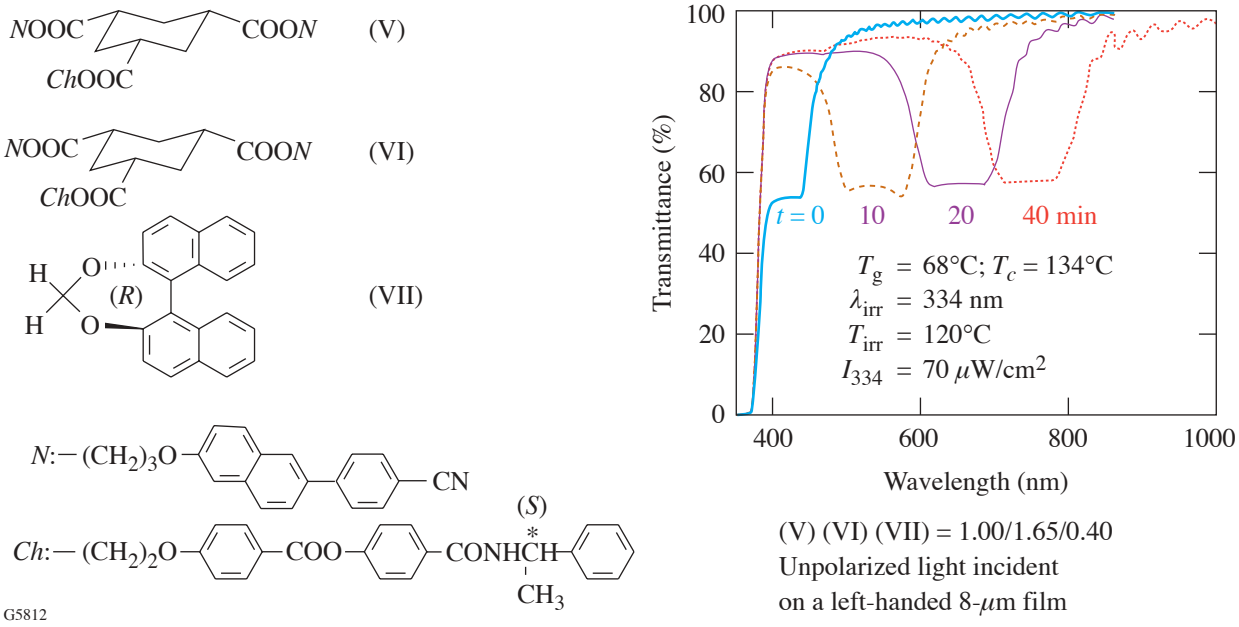

(V) (VI) (VII) = 1.00/1.65/0.40
Unpolarized light incident
on a left-handed 8-μm film

Figure 93.52
A phototunable glassy cholesteric film.

cholesteric mesomorphism and that between the right- and left-handed cholesteric mesomorphism have also been reported,[58–63] where a helical pitch length of the order of 10 μm was observed.

Of all the photoresponsive moieties that have been explored, diarylethenes[64] appear to be the most promising in terms of thermal stability and fatigue resistance. The premise is that the two interconvertible isomers, viz., the open and closed forms, present disparate helical twisting powers in a liquid crystal matrix. Indeed, the closed form of chiral diarylethenes was found to have a stronger helical twisting power than the open form in nematic liquid crystal hosts with a helical pitch length of the order of 10 μm in all cases.[62,63] To accomplish tunable reflective coloration in the visible region, a cholesteric liquid crystal with a short pitch length must be used as the host to define the base case. Moreover, glassy liquid crystal films are much preferred over liquid crystal films in practical application. Isomerization of diarylethenes was found to take place not only in liquid but also in single-crystalline[64] and amorphous[65,66] solids without altering the morphology. Modulation of pitch length, however, requires a relative rotation between quasi-nematic layers as depicted in Fig. 93.46, a macroscopic rearrangement allowable only in the liquid state; therefore, we aim at cholesteric GLC's containing diarylethene moieties.

A Novel Class of Photoresponsive GLC's

Reversible tunability of reflective coloration using diarylethene-containing GLC's is envisioned in Fig. 93.53. A glassy cholesteric film comprising the open form of a diarylethene moiety with a predetermined reflection wavelength λ_R^0 is heated to above its T_g, where irradiation at λ_1 is performed to afford the closed form. This treatment results in a shorter reflection wavelength λ_R^c, which can be preserved in the solid state with subsequent cooling to below T_g. The more-extended conjugation of the closed form could cause light absorption in the visible region. With λ_R^c frozen in the solid state, irradiation of the closed form at λ_2 will regenerate the open form, thereby bleaching the undesired absorptive color without altering λ_R^c, a clear advantage over the use of liquid films. As dictated by the open form, subsequent heating to above T_g will recover λ_R^0, which can then be frozen in the solid state by cooling through T_g. To attain the envisioned phototunability, we have developed the first diarylethene-containing nematic and chiral glasses. The molecular structures are depicted in Fig. 93.54, where *N* and *Ch* denote a nematic and a chiral moiety, respectively. Work is in progress to take advantage of these novel glassy materials together with the high-temperature GLC's shown in Figs. 93.48 and 93.50 for reversible tunability of reflective coloration with superior thermal stability and fatigue resistance.

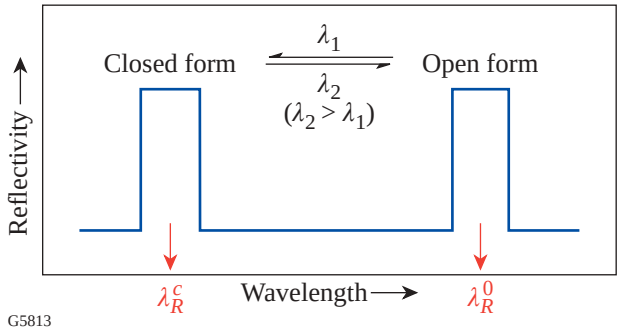

Figure 93.53
Reversible phototunability of reflective coloration.

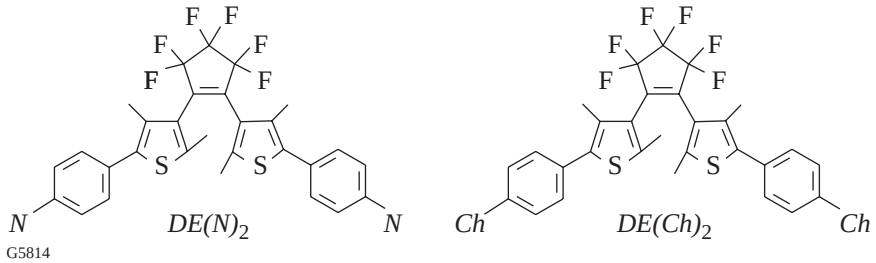

Figure 93.54
Novel glassy materials containing photoresponsive diarylethenes.

Conclusions

Glassy liquid crystals with elevated glass transition and clearing temperatures, a broad mesomorphic fluid temperature range, and excellent morphological stability have been developed for a diversity of photonic applications. In particular, glassy cholesteric films have been demonstrated for high-performance circular polarizers, optical notch filters, and reflectors across a spectral range that can be tuned by varying the chemical composition or by UV irradiation, albeit irreversibly. The molecular design concept governing glassy liquid crystals has been generalized to photoresponsive material systems containing diarylethenes, thereby enabling reversible tunability of reflective coloration with superior thermal stability and fatigue resistance.

ACKNOWLEDGMENT

The authors wish to thank F. Fan for synthesizing some of the materials reported herein, and S. D. Jacobs and K. L. Marshall at the University of Rochester's Laboratory for Laser Energetics for technical advice and helpful discussions. They are grateful for the financial support provided by the Multidisciplinary University Research Initiative, administered by the Army Research Office, under DAAD19-01-1-0676, the National Science Foundation under Grants CTS-9818234 and 0204827, and Eastman Kodak Company. Additional funding was provided by the U.S. Department of Energy Office of Inertial Confinement Fusion under Cooperative Agreement No. DE-FC03-92SF19460, the University of Rochester, and the New York State Energy Research and Development Authority. The support of DOE does not constitute an endorsement by DOE of the views expressed in this article.

REFERENCES

1. C. A. Angell, Science **267**, 1924 (1995).
2. P. G. Debenedetti and F. H. Stillinger, Nature **410**, 259 (2001).
3. G. Zerbi, ed. *Organic Materials for Photonics: Science and Technology*, European Materials Research Society Monographs, v. 6 (North-Holland, Amsterdam, 1993).
4. D. Braun and R. Langendorf, J. Prakt. Chem.-Chem. Ztg. **341**, 128 (1999).
5. I. Alig *et al.*, J. Mater. Chem. **8**, 847 (1998).
6. D. F. O'Brien *et al.*, Adv. Mater. **10**, 1108 (1998).
7. K. Naito and A. Miura, J. Phys. Chem. **97**, 6240 (1993).
8. K. Katsuma and Y. Shirota, Adv. Mater. **10**, 223 (1998).
9. M. Halim *et al.*, *ibid.*, **11**, 371 (1999).
10. N. Johansson *et al.*, *ibid.*, **10**, 1136 (1998).
11. U. Bach *et al.*, *ibid.*, **12**, 1060 (2000).
12. B. Schartel, T. Damerau, and M. Hennecke, Phys. Chem. Chem. Phys. **2**, 4690 (2000).
13. S. Wang *et al.*, J. Am. Chem. Soc. **122**, 5695 (2000).
14. P. J. Collings and J. S. Patel, eds. *Handbook of Liquid Crystal Research* (Oxford University Press, New York, 1997).
15. K. Tsuji, M. Sorai, and S. Seki, Bull. Chem. Soc. Jpn. **44**, 1452 (1971); M. Sorai and S. Seki, *ibid.*, 2887 (1971).
16. C. B. McArdle, ed. *Side Chain Liquid Crystal Polymers* (Chapman and Hall, New York, 1989).
17. N. A. Platé and S. L. Schnur, eds. *Liquid-Crystal Polymers*, Specialty Polymers (Plenum Press, New York, 1993).
18. A. Ciferri, ed. *Liquid Crystallinity in Polymers* (VCH Publishers, New York, 1991).
19. H. Shi, S. H. Chen, M. E. De Rosa, T. J. Bunning, and W. W. Adams, Liq. Cryst. **20**, 277 (1996).
20. W. Wedler *et al.*, J. Mater. Chem. **1**, 347 (1991).
21. G. Attard and C. T. Imrie, Liq. Cryst. **11**, 785 (1992).
22. H. Dehne *et al.*, Liq. Cryst. **6**, 47 (1989).
23. G. S. Attard, C. T. Imrie, and F. E. Karasz, Chem. Mater. **4**, 1246 (1992).
24. N. Tamaoki, G. Kruk, and H. Matsuda, J. Mater. Chem. **9**, 2381 (1999).
25. F.-H. Kreuzer *et al.*, Mol. Cryst. Liq. Cryst. **199**, 345 (1991).
26. F.-H. Kreuzer, R. Maurer, and P. Spes, Makromol. Chem., Macromol. Symp. **50**, 215 (1991).
27. K. D. Gresham *et al.*, J. Polym. Sci. A, Polym. Chem. **32**, 2039 (1994).
28. K. T. Lorenz *et al.*, Adv. Mater. **8**, 414 (1996).
29. S. A. Ponomarenko *et al.*, Macromolecules **33**, 5549 (2000).
30. I. M. Saez, J. W. Goodby, and R. M. Richardson, Chem. Eur. J. **7**, 2758 (2001).
31. V. Percec *et al.*, Macromolecules **25**, 3851 (1992).
32. R. Dreher and G. Meier, Phys. Rev. A **8**, 1616 (1973).
33. H. Shi and S. H. Chen, Liq. Cryst. **17**, 413 (1994).
34. *ibid.*, **18**, 733 (1995).
35. J. C. Mastrangelo, T. N. Blanton, and S. H. Chen, Appl. Phys. Lett. **66**, 2212 (1995).
36. H. Shi and S. H. Chen, Liq. Cryst. **19**, 785 (1995).
37. S. H. Chen, J. C. Mastrangelo, H. Shi, A. Bashir-Hashemi, J. Li, and N. Gelber, Macromolecules **28**, 7775 (1995).

38. H. Shi and S. H. Chen, Liq. Cryst. **19**, 849 (1995).

39. M. E. De Rosa, W. W. Adams, T. J. Bunning, H. Shi, and S. H. Chen, Macromolecules **29**, 5650 (1996).

40. S. H. Chen, J. C. Mastrangelo, T. N. Blanton, A. Bashir-Hashemi, and K. L. Marshall, Liq. Cryst. **21**, 683 (1996).

41. S. H. Chen, H. Shi, B. M. Conger, J. C. Mastrangelo, and T. Tsutsui, Adv. Mater. **8**, 998 (1996).

42. S. H. Chen, J. C. Mastrangelo, H. Shi, T. N. Blanton, and A. Bashir-Hashemi, Macromolecules **30**, 93 (1997).

43. S. H. Chen, D. Katsis, A. W. Schmid, J. C. Mastrangelo, T. Tsutsui, and T. N. Blanton, Nature **397**, 506 (1999).

44. F. Y. Fan, S. W. Culligan, J. C. Mastrangelo, D. Katsis, S. H. Chen, and T. N. Blanton, Chem. Mater. **13**, 4584 (2001).

45. D. Katsis, P. H. M. Chen, J. C. Mastrangelo, S. H. Chen, and T. N. Blanton, *ibid.*, **11**, 1590 (1999).

46. H. P. Chen, D. Katsis, J. C. Mastrangelo, S. H. Chen, S. D. Jacobs, and P. J. Hood, Adv. Mater. **12**, 1283 (2000).

47. M. Srinivasarao, Chem. Rev. **99**, 1935 (1999).

48. S. H. Chen, J. C. Mastrangelo, and R. J. Jin, Adv. Mater. **11**, 1183 (1999).

49. P. Pollmann and B. Wiege, Mol. Cryst. Liq. Cryst. **150B**, 375 (1987).

50. H. Kimura, M. Hosino, and H. Nakano, J. Phys. Colloq. **40**, 174 (1979).

51. R. B. Meyer, Appl. Phys. Lett. **14**, 208 (1969); H. Baessler and M. M. Labes, Phys. Rev. Lett. **21**, 1791 (1968).

52. R. A. M. Hikmet and H. Kemperman, Nature **392**, 476 (1998).

53. Y. Nishio *et al.*, Macromolecules **31**, 2384 (1998).

54. E. Sackmann, J. Am. Chem. Soc. **93**, 7088 (1971).

55. H.-K. Lee *et al.*, J. Phys. Chem. B **104**, 7023 (2000).

56. A. Yu. Bobrovsky *et al.*, Adv. Mater. **12**, 1180 (2000).

57. N. Tamaoki *et al.*, *ibid.*, **12**, 94 (2000); N. Tamaoki, *ibid*. **13**, 1135 (2001).

58. B. L. Feringa, P. M. Huck, and H. A. van Doren, J. Am. Chem. Soc. **117**, 9929 (1995).

59. M. Suarez and G. B. Schuster, *ibid.*, 6732 (1995).

60. C. Denekamp and B. L. Feringa, Adv. Mater. **10**, 1080 (1999).

61. B. L. Feringa *et al.*, Chem. Rev. **100**, 1789 (2000).

62. T. Yamaguchi *et al.*, Chem. Mater. **12**, 869 (2000).

63. T. Yamaguchi *et al.*, J. Mater. Chem. **11**, 2453 (2001).

64. M. Irie, Chem. Rev. **100**, 1685 (2000).

65. T. Kawai, T. Koshido, and K. Yoshino, Appl. Phys. Lett. **67**, 795 (1995).

66. T. Kawai *et al.*, Jpn. J. Appl. Phys. **38**, L1194 (1999).

High-Resolution Near-Field Raman Microscopy of Single-Walled Carbon Nanotubes

Introduction

Recent rapid advances in nanotechnology and nanoscience are largely due to our newly acquired ability to measure and manipulate individual structures on the nanoscale. Among the new methods are scanning probe techniques, optical tweezers, and high-resolution electron microscopes. A recently demonstrated near-field optical technique allows spectroscopic measurements with 20-nm spatial resolution.[1] This method makes use of the strongly enhanced electric field close to a sharp metal tip under laser illumination and relies on the detection of two-photon excited fluorescence. Fluorescence imaging, however, requires a high fluorescence quantum yield of the system studied or artificial labeling with fluorophores. Furthermore, fluorescence quenching by the metal tip competes with the local field enhancement effect and therefore limits the general applicability. On the other hand, Raman scattering probes the unique vibrational spectrum of the sample and directly reflects its chemical composition and molecular structure. A main drawback of Raman scattering is the extremely low scattering cross section, which is typically 14 orders of magnitude smaller than the cross section of fluorescence. Surface-enhanced Raman scattering (SERS), induced by nanometer-sized metal structures, has been shown to provide enormous enhancement factors of up to 10^{15}, allowing for Raman spectroscopy even on the single-molecule level.[2,3] Controlling SERS with a sharp metal tip that is raster scanned over a sample surface has been proposed in Refs. 1 and 4, and near-field Raman enhancement has been experimentally demonstrated in Refs. 5–9. Here, we show the chemical specificity of this near-field technique and demonstrate an unprecedented spatial resolution.

Single-walled carbon nanotubes (SWNT's) have been the focus of intense interest due to a large variety of potential nanotechnological applications. The unique properties of SWNT's arise from their particular one-dimensional structure, which is directly linked to the characteristic Raman bands. Raman scattering on SWNT's has been studied intensively in the literature (see, e.g., Refs. 10–13), and Raman enhancements of up to 10^{12} have been reported for tubes in contact with fractal silver colloidal clusters.[14] In this article, near-field Raman imaging of SWNT's is demonstrated using a sharp silver tip as a probe. We show, for the first time, that single isolated SWNT's can be detected optically with a spatial resolution of better than 30 nm. This high-resolution capability is applied to resolve local variations in the Raman spectrum along a single SWNT that would be hidden in far-field measurements. The near-field origin of the Raman enhancement is proven by tip-to-sample-distance measurements.

Experimental

Our experimental setup is based on an inverted optical microscope with an x,y scan stage for raster scanning a transparent sample with SWNT's. A laser beam (λ = 633 nm, 30 to 100 μW) is reflected by a dichroic beam splitter and focused by a high numerical aperture objective (1.4 N.A.) on the sample surface. A sharp silver tip is positioned near the focus of the beam and maintained above the sample surface at a distance $\approx$ 1 nm by means of a sensitive shear-force feedback mechanism.[15] Raman-scattered light is collected with the same objective, transmitted by the beam splitter, and filtered by a long pass filter. The signal is detected either by a combination of a spectrograph and a thermoelectrically cooled charge-coupled device (CCD) or by a narrow bandpass filter (FWHM = 10 nm) centered at 760 nm (or 700 nm), followed by a single-photon counting avalanche photodiode. A near-field Raman image is established by raster scanning the sample and continuously recording the scattered Raman signal. Sharp silver tips with a radius of 10 to 15 nm are produced by electrochemical etching followed by focused-ion-beam (FIB) milling with a dual-beam FIB system (FEI Strata-235) and applying a similar procedure as used for STM/AFM tip sharpening.[16]

To establish a strong field enhancement at the tip, the electric field of the exciting laser beam needs to be polarized along the tip axis.[17] To achieve this condition in our on-axis illumination scheme, we displace the tip from the center of the beam in the direction of polarization into one of the two longitudinal field lobes characteristic of strongly focused Gaussian beams.[18] The strength of this longitudinal field increases with increasing N.A. of the focusing lens and, in our

configuration, is only five times weaker than the transverse field strength at the center of the focus.

Results and Discussion

Two different types of SWNT samples were studied. The first sample consists of nearly monodisperse SWNT's grown by chemical vapor deposition (CVD) on SiO_2 substrates. The substrates were first cleaned by solvent washing, then heated to 700°C in a tube furnace for 30 min while being exposed to air. Next, 50 μL of Ferritin solution [Sigma-Aldrich; diluted in deionized (DI) water, 1:10 ratio (Ferritin: H_2O)] was applied to the clean substrate, which was left for 30 s, then rinsed with DI water and placed in the tube furnace using growth parameters similar to commonly known SWNT growth methods.[19] The material for the second sample was purchased from Bucky USA and consists of purified SWNT's with a diameter distribution from 1.0 to 1.8 nm, produced by arc discharge using Ni/Y catalyst particles. The material was dispersed in dichlorethane, sonicated for 1 h, and spin-cast onto a microscope cover glass. AFM measurements were performed to determine sample coverage and to distinguish spatially isolated tubes from nanotube bundles.

The far-field Raman spectra of the SWNT samples (not shown) are dominated by the sharp tangential stretching mode at 1596 cm^{-1} (G band) and a broader band around 2615 cm^{-1} (G' band), which arises from an overtone of the disorder-induced mode around 1310 cm^{-1}.[20] Figure 93.55 shows confocal far-field Raman images of SWNT bundles produced by arc discharge that were recorded by integrating the signal intensity of the G' band [760-nm bandpass filter (see above)] for vertical (a) and horizontal (b) polarization of the incident laser beam. Similar Raman images are obtained by detecting the intensity of the G band using the 700-nm bandpass filter. The Raman images clearly demonstrate that tubes oriented completely perpendicular to the respective light polarization do not produce any signal (see arrows in Fig. 93.55). This polarization contrast is a consequence of the polarization properties of the G and G' Raman bands reported for G in the literature.[11,12,21] AFM measurements of the same area reveal that the diameter of the nanotube bundles varies between 5 and 15 nm, which corresponds to 10 to 100 individual nanotubes per bundle.

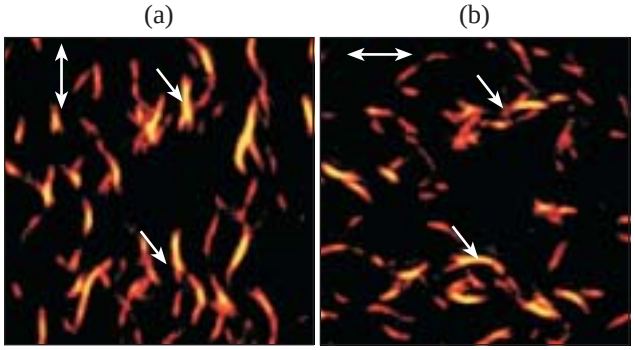

Figure 93.55
Confocal Raman images of SWNT bundles produced by arc discharge on glass acquired by detecting the intensity of the G' band ($\nu = 2615$ cm^{-1}) while raster-scanning the sample (without metal tip, scan area 15×15 μm) for vertical (a) and horizontal polarization (b) of the laser excitation at 633 nm. The arrows indicate tubes that are oriented completely perpendicular to one polarization direction, demonstrating the polarization contrast.

Confocal Raman imaging of SWNT's grown by CVD was not possible within feasible acquisition times because the sample consists mostly of separated individual SWNT's for which the Raman scattering strength is much weaker. However, as shown in Fig. 93.56(a) for CVD-grown SWNT's, the contrast and resolution of Raman images can be greatly increased by positioning a sharp silver tip near the laser focus. The simultaneously recorded topographic image is presented in Fig. 93.56(b). The lower portions [Figs. 93.56(c) and 93.56(d)] show cross sections taken along the dashed white lines. Besides SWNT's, the topographic image shows a large number of small circular features with a height ≈ 2 nm, which are due to condensating water and can be removed by sample heating to 70°C. Comparison of the widths (FWHM) of SWNT's in the topographic and Raman images indicates that the resolution of the Raman image is better than the resolution of the topographic image (25 nm versus 30 nm). This high spatial resolution is unprecedented and clearly indicates the near-field origin of the Raman signal. The width of the optical features and the topographical features results from the convolution of the tip shape with the object studied and is therefore limited by the finite size of the tip apex. Both images are closely correlated and the SWNT's are clearly identified. The small topographic features formed by condensation do not show up, however, in the Raman image, which proves the chemical specificity of the method. The diameter of SWNT's grown by CVD can be controlled by growth parameters. The sample used in Fig. 93.56 consists mostly of SWNT's with a diameter ≈ 1.4 nm, which is verified by the topographic data in Figs. 93.56(b) and 93.56(d) and also by independent AFM measurements in the absence of water condensation. Thus, we observe near-field Raman scattering from spatially separated single SWNT's. It is important to notice that vertically *and* horizontally oriented SWNT's are observed in the Raman

image with similar signal intensity, even though the incident laser light is oriented vertically. This observation is in strong contrast to the polarization contrast observed in the far-field measurements shown in Fig. 93.55. Accordingly, the polarization of the enhanced field has to be radially symmetric with respect to the tip axis. This finding is in agreement with theoretical calculations[17] and confirms the unique properties of the near field.

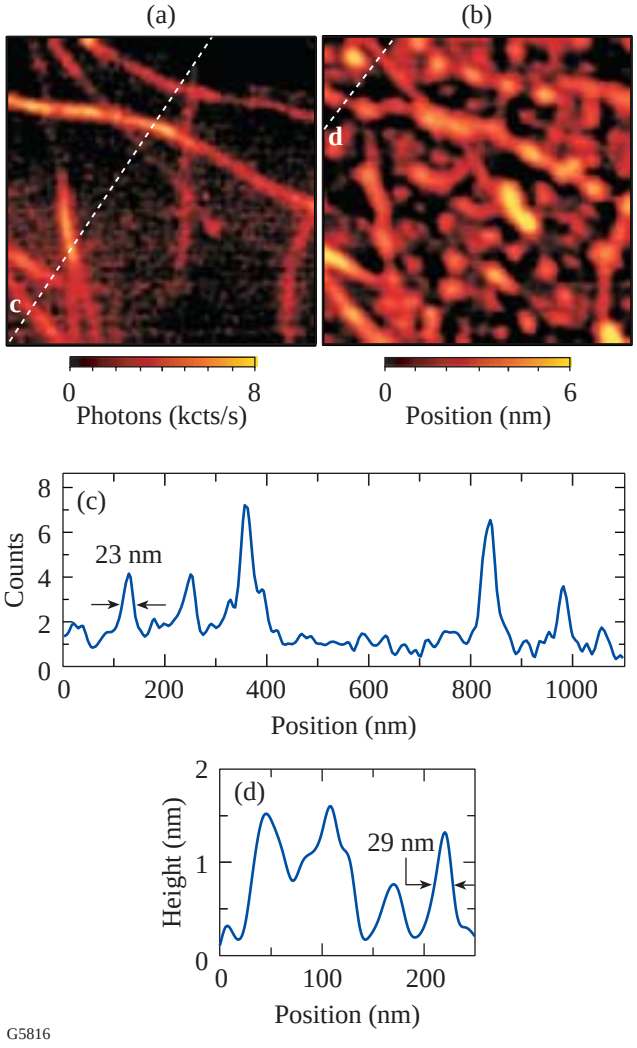

Figure 93.56
Simultaneous near-field Raman image (a) and topographic image (b) of SWNT's grown by CVD on glass (scan area $1 \times 1\ \mu$m). The Raman image is acquired by detecting the intensity of the G' band upon laser excitation at 633 nm. No Raman scattering signal is detected from humidity-related circular features present in the topographic image (see text). (c) Cross section taken along the indicated dashed line in the Raman image. (d) Cross section taken along the indicated dashed line in the topographic image. The height of individual tubes is ≈ 1.4 nm. Vertical units are photon counts per second for (c) and nanometer for (d).

The optical resolution apparent in Fig. 93.56 shows that the enhanced field is laterally confined to the size of the metal tip. To demonstrate the confinement of the enhanced fields in the longitudinal direction, the tip is positioned above a SWNT and the Raman scattering strength is recorded as a function of tip-to-sample distance Δz. The result, shown in Fig. 93.57, has been fitted with an exponential curve and normalized with the Raman scattering strength in the absence of the tip, i.e., with the far-field Raman signal. For distances $\Delta z < 30$ nm, the increase of the signal clearly indicates a distance-dependent near-field contribution with a decay length of 11 nm. This longitudinal confinement is in agreement with the lateral confinement observed in the near-field Raman images and consistent with the tip radius of 10 to 15 nm as determined by a scanning electron microscopy [cf. Fig. 93.57(b)]. All of the tips used in our experiments were fabricated by the same procedure and rendered similar SEM images; however, only about 30% to 40% of the tips produced a measurable signal enhancement. The reason for this behavior is the subject of ongoing studies. The highest Raman enhancement factors observed so far were estimated to be around 10^3. These numbers follow from the detected ratio of near-field to far-field signals and from a comparison of the different volumes probed by the near field and the far field.

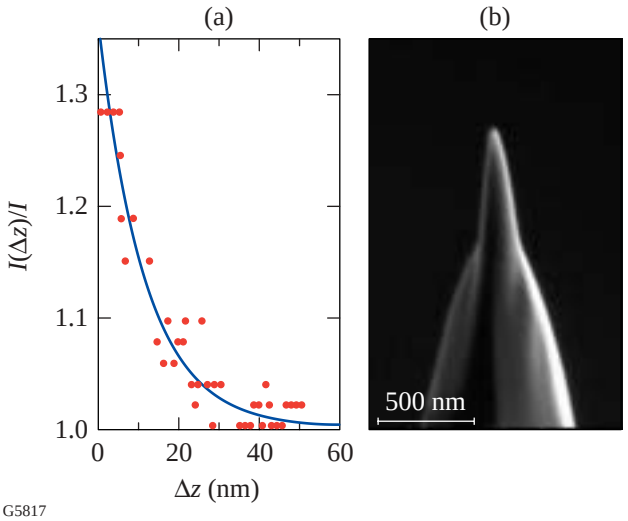

Figure 93.57
(a) Dependence of the Raman-scattering strength of the G' band (I) on the longitudinal separation (Δz) between a single SWNT and the tip. The solid line is an exponential fit with a decay length of 11 nm. The signal is normalized with the far-field signal. (b) Scanning electron micrograph of a sharp silver tip fabricated by focused-ion-beam milling.

To demonstrate the high-resolution spectroscopic capabilities of the near-field technique presented here, we investigate the Raman spectrum along a SWNT with a diameter of 1.7 nm grown by arc discharge. Figure 93.58(a) shows the topography near the end of a SWNT produced by this technique. Three bumps with a height ≈ 5 nm can be recognized on top of the SWNT. Because of their size, these bumps are presumably Ni/Y-catalyst particles, indicating the initial point of growth.[22] The labels 1 to 4 in Fig. 93.58(a) mark the positions at which Raman spectra were taken in the presence of the metal tip. At the very beginning of the SWNT (positions 1 and 2) the G band at 1596 cm^{-1} (FWHM = 17 cm^{-1}) dominates the spectra and is significantly stronger than the G' band at 2619 cm^{-1} (FWHM = 35 cm^{-1}) with an amplitude ratio $G/G' \approx 1.3$ [see Fig. 93.58(b)]. Moving along the SWNT to position 3 and farther to position 4 (separated by 35 nm and 85 nm, respectively), however, the amplitude of the G band decreases with respect to the G' band and the ratio G/G' reduces to ~0.7. Simultaneously, the shape of the G' band changes and its center frequency is shifted to 2610 cm^{-1}, whereas the G band remains at 1596 cm^{-1}. For 1 and 2, the G' band has a Lorentzian shape, while for 3 and 4, two Lorentzian peaks are needed to model its shape. Raman spectra recorded beyond point 4 in Fig. 93.58(a) remain unchanged.

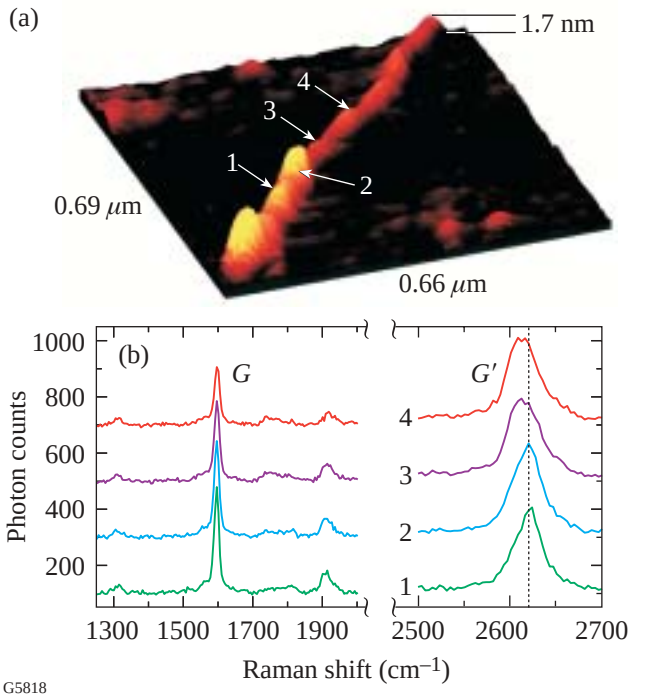

Figure 93.58
(a) Three-dimensional topographic image of a SWNT on glass grown by arc discharge. The three bumps are presumably enclosed Ni/Y catalyst particles and indicate the initial point of growth. (b) Near-field Raman spectra detected at the marked positions 1 to 4 in (a). The distance between positions 2 and 3 is 35 nm. The spectra are offset for clarity.

Variations in the Raman spectrum reflect changes in the molecular structure that can have several origins such as external stress, due to the catalyst particles, or local defects in the tube structure. The observed spectral variations between 2 and 3 can also be explained by a change of the tube structure, described by $(n,m) \rightarrow (n',m')$, which modifies the electronic-state energies of the tube and therefore the resonance enhancement of the Raman bands at a fixed excitation energy. A decrease of the resonance enhancement between positions 2 and 3 would lead to a lower G-band amplitude and could cause a splitting of the G' band into a double peak.[20]

Recent experiments have shown that huge surface enhancement of Raman signals can be accompanied by fluctuating white-light emission.[3,23] According to Ref. 23, huge SERS enhancement and strong white-light emission require chemisorption of the Raman scatterer to the metal surface. Since we maintain a well-defined separation (≈ 1 nm) between tip and sample in our experiments, we do not expect a significant white-light contribution. Moreover, white-light emission is observed for Raman enhancement factors more than ten orders of magnitude stronger than the enhancements determined in our experiments. Indeed, our near-field Raman spectra show no indication for a significant broadband background [see Fig. 93.58(b)]. To exclude any contributions to the image contrast arising from background signals, we recorded for each image pixel the full spectrum and integrated the intensity of the G' band and the G band while subtracting the background. The resulting images were virtually identical to those shown in Fig. 93.56(a). We also note that by comparing the near-field and far-field Raman spectra of SWNT's, we find, within the noise limit, no indication for the gradient-field Raman effect discussed in Ref. 24.

Conclusion

We have demonstrated a method for nanoscale Raman spectroscopy with sub-30-nm spatial resolution. This method extends our abilities to characterize weakly fluorescent structures on the nanoscale. Near-field Raman spectroscopy combined with simultaneous AFM measurements appears to be extremely useful for investigations of carbon nanotubes. This method holds promise for the experimental investigation of special structural nanotube features, such as kinks, intertube junctions, or even tubes loaded with C_{60} molecules.

ACKNOWLEDGMENT

The authors wish to thank M. Beversluis and A. Bouhelier for stimulating discussions. Assistance on the CVD of SWNT's by Dr. T. Rueckes and Dr. B. Segal of Nantero (Woburn, MA) is gratefully acknowledged. This research was supported by NSF through grant BES-0086368.

REFERENCES

1. E. J. Sánchez, L. Novotny, and X. S. Xie, Phys. Rev. Lett. **82**, 4014 (1999).
2. K. Kneipp *et al.*, Phys. Rev. Lett. **78**, 1667 (1997).
3. S. Nie and S. R. Emory, Science **275**, 1102 (1997).
4. J. Wessel, J. Opt. Soc. Am. B **2**, 1538 (1985).
5. C. L. Jahncke, H. D. Hallen, and M. A. Paesler, J. Raman Spectrosc. **27**, 579 (1996).
6. R. M. Stöckle *et al.*, Chem. Phys. Lett. **318**, 131 (2000).
7. N. Hayazawa *et al.*, Chem. Phys. Lett. **335**, 369 (2001).
8. L. T. Nieman, G. M. Krampert, and R. E. Martinez, Rev. Sci. Instrum. **72**, 1691 (2001).
9. N. Hayazawa *et al.*, J. Chem. Phys. **117**, 1296 (2002).
10. A. Jorio *et al.*, Phys. Rev. Lett. **86**, 1118 (2001).
11. Z. Yu and L. Brus, J. Phys. Chem. B **105**, 1123 (2001).
12. G. S. Duesberg *et al.*, Phys. Rev. Lett. **85**, 5436 (2000).
13. J. Maultzsch, S. Reich, and C. Thomsen, Phys. Rev. B **65**, 233402 (2002).
14. K. Kneipp *et al.*, Phys. Rev. Lett. **84**, 3470 (2000).
15. K. Karrai and R. D. Grober, Appl. Phys. Lett. **66**, 1842 (1995).
16. M. J. Vasile, C. Biddick, and H. Huggins, Appl. Phys. Lett. **64**, 575 (1994).
17. L. Novotny, E. J. Sánchez, and X. S. Xie, Ultramicroscopy **71**, 21 (1998).
18. B. Sick, B. Hecht, and L. Novotny, Phys. Rev. Lett. **85**, 4482 (2000).
19. J. H. Hafner, C. L. Cheung, and C. M. Leiber, J. Am. Chem. Soc. **121**, 9750 (1999).
20. A. G. Souza Filho *et al.*, Phys. Rev. B **65**, 085417 (2002).
21. A. Jorio *et al.*, Phys. Rev. Lett. **85**, 2617 (2000).
22. C. Journet *et al.*, Nature **388**, 756 (1997).
23. A. M. Michaels, M. Nirmal, and L. E. Brus, J. Am. Chem. Soc. **121**, 9932 (1999).
24. E. J. Ayars, H. D. Hallen, and C. L. Jahncke, Phys. Rev. Lett. **85**, 4180 (2000).

Publications and Conference Presentations

Publications

S. D. Jacobs, H. M. Pollicove, E. M. Fess, and J. Schoen, "Aspheric Optics Manufacturing for Commercial and Military Systems," in *First Symposium for Explosive Materials, Weapons, and Military Technology* (Military Academy General Mihailo Apostolski, Skopje, Macedonia, 2002), pp. 497–504.

R. K. Kirkwood, J. D. Moody, A. B. Langdon, B. I. Cohen, E. A. Williams, M. R. Dorr, J. A. Hittinger, R. Berger, P. E. Young, L. J. Suter, L. Divol, S. H. Glenzer, O. L. Landen, and W. Seka, "Observation of Saturation of Energy Transfer between Copropagating Beams in a Flowing Plasma," Phys. Rev. Lett. **89**, 215003 (2002).

T. Z. Kosc, K. L. Marshall, S. D. Jacobs, and J. C. Lambropoulous, "Electric-Field-Induced Rotation of Polymer Cholesteric Liquid Crystal Flakes: Mechanisms and Applications," in *Liquid Crystals VI*, edited by I.-C. Khoo (SPIE, Bellingham, WA, 2002), Vol. 4799, pp. 96–101.

C. K. Li, F. H. Séguin, J. A. Frenje, S. Kurebayashi, R. D. Petrasso, D. D. Meyerhofer, J. M. Soures, J. A. Delettrez, V. Yu. Glebov, P. B. Radha, F. J. Marshall, S. P. Regan, S. Roberts, T. C. Sangster, and C. Stoeckl, "Effects of Fuel–Shell Mix Upon Direct-Drive, Spherical Implosions on OMEGA," Phys. Rev. Lett. **89**, 165002 (2002).

S. G. Lukishova, R. W. Boyd, N. Lepeshkin, and K. L. Marshall, "Cumulative Birefringence Effects of Nanosecond Laser Pulses in Dye-Doped Planar Nematic Liquid Crystal Layers," J. Nonlinear Opt. Phys. Mater. **11**, 341 (2002).

S. Papernov and A. W. Schmid, "Correlations Between Embedded Single Gold Nanoparticles in SiO_2 Thin Film and Nanoscale Crater Formation Induced by Pulsed-Laser Radiation," J. Appl. Phys. **92**, 5720 (2002).

G. Sabouret, C. Williams, and R. Sobolewski, "Resistive Switching Dynamics in Current-Biased $YBa_2Cu_3O_{7-x}$ Microbridges Excited by Nanosecond Electrical Pulses," Phys. Rev. B **66**, 132501 (2002).

W. Seka, H. A. Baldis, J. Fuchs, S. P. Regan, D. D. Meyerhofer, C. Stoeckl, B. Yaakobi, R. S. Craxton, and R. W. Short, "Multibeam Stimulated Brillouin Scattering from Hot, Solid-Target Plasmas," Phys. Rev. Lett. **89**, 175002 (2002).

M. D. Skeldon, "Optical Pulse-Shaping System Based on an Electro-Optic Modulator Driven by an Aperture-Coupled-Stripline Electrical-Waveform Generator," J. Opt. Soc. Am. B **19**, 2423 (2002).

C. Stoeckl, V. Yu. Glebov, J. D. Zuegel, D. D. Meyerhofer, and R. A. Lerche, "Wide-Dynamic-Range 'Neutron Bang Time' Detector on OMEGA," Rev. Sci. Instrum. **73**, 3796 (2002).

Forthcoming Publications

A. Babushkin, M. J. Harvey, and M. D. Skeldon, "The Output Signal-to-Noise Ratio of a Nd:YLF Regenerative Amplifier," to be published in Applied Optics.

Y. Geng, S. W. Culligan, A. Trajkovska, J. U. Wallace, and S. H. Chen, "Monodisperse Oligofluorenes Forming Glassy Nematic Films for Polarized Blue Emission," to be published in Chemistry of Materials.

V. Yu. Glebov, C. Stoeckl, T. C. Sangster, D. D. Meyerhofer, P. B. Radha, S. Padalino, L. Baumgart, R. Coburn, and J. Fuschino, "Carbon Activation Diagnostic for Tertiary Neutron Measurements," to be published in Review of Scientific Instruments.

G. N. Gol'tsman, K. Smirnov, P. Kouminov, B. Voronov, N. Kaurova, V. Drakinsky, J. Zhang, A. Verevkin, and R. Sobolewski, "Fabrication of Nanostructured Superconducting Single-Photon Detectors," to be published in IEEE Transactions on Applied Superconductivity.

V. N. Goncharov J. P. Knauer, P. W. McKenty, T. C. Sangster, S. Skupsky, R. Betti, R. L. McCrory, and D. D. Meyerhofer, "Improved Performance of Direct-Drive ICF Target Designs with Adiabat Shaping Using an Intensity Picket," to be published in Physics of Plasmas (invited).

O. V. Gotchev, P. A. Jaanimagi, J. P. Knauer, F. J. Marshall, D. D. Meyerhofer, N. Bassett, and J. B. Oliver, "High-Throughput, High-Resolution, Kirkpatrick–Baez Microscope for Advanced Streaked Imaging of ICF Experiments on OMEGA," to be published in Review of Scientific Instruments.

Q. Guo, X. Teng, S. Rahman, and H. Yang, "Patterned Langmuir–Blodgett Films of Monodisperse Iron Nanoparticles Using Soft Lithographic Technique," to be published in the Journal of the American Chemical Society.

D. L. McCrorey, R. C. Mancini, V. A. Smalyuk, S. P. Regan, and B. Yaakobi, "Spectroscopic Determination of Compressed-Shell Conditions in OMEGA Implosions Based on Ti *K*-Shell Line Absorption Analysis," to be published in Review of Scientific Instruments.

R. L. McCrory, D. D. Meyerhofer, R. Betti, T. R. Boehly, R. S. Craxton, T. J. B. Collins, J. A. Delettrez, R. Epstein, V. Yu. Glebov, V. N. Goncharov, D. R. Harding, R. L. Keck, J. H. Kelly, J. P. Knauer, S. J. Loucks, L. Lund, J. A. Marozas, P. W. McKenty, F. J. Marshall, S. F. B. Morse, P. B. Radha, S. P. Regan, S. Roberts, W. Seka, S. Skupsky, V. A. Smalyuk, C. Sorce, C. Stoeckl, J. M. Soures, R. P. J. Town, B. Yaakobi, J. A. Frenje, C. K. Li, R. D. Petrasso, F. H. Séguin, K. Fletcher, S. Padalino, C. Freeman, and C. Sangster, "Direct-Drive Inertial Confinement Fusion Research at the Laboratory for Laser Energetics," to be published in the proceedings of *Current Trends in International Fusion Research: A Review*.

R. L. McCrory, D. D. Meyerhofer, S. J. Loucks, S. Skupsky, R. E. Bahr, R. Betti, T. R. Boehly, R. S. Craxton, T. J. B. Collins, J. A. Delettrez, W. R. Donaldson, R. Epstein, J. A. Frenje, V. Yu. Glebov, V. N. Goncharov, D. R. Harding, P. A. Jaanimagi, R. L. Keck, J. H. Kelly, T. J. Kessler, J. P. Knauer, C. K. Li, L. Lund, J. A. Marozas, P. W. McKenty, F. J. Marshall, S. F. B. Morse, R. D. Petrasso, P. B. Radha, S. P. Regan, S. Roberts, T. C. Sangster, F. H. Séguin, W. Seka, V. A. Smalyuk, C. Sorce, J. M. Soures, C. Stoeckl, R. P. J. Town, B. Yaakobi, and J. D. Zuegel, "Direct-Drive Inertial Confinement Fusion Research at the Laboratory for Laser Energetics," to be published in Nuclear Fusion.

S. Papernov and A. W. Schmid, "Damage Behavior of SiO_2 Thin Films Containing Gold Nanoparticles Lodged on a Predetermined Distance from the Film Surface," to be published in the *Proceedings of the XXXIV Annual Symposium on Optical Materials for High Power Lasers*.

R. D. Petrasso, F. H. Séguin, J. A. Frenje, C. K. Li, J. R. Rygg, B.-E. Schwartz, S. Kurebayashi, P. B. Radha, C. Stoeckl, J. M. Soures, J. A. Delettrez, V. Yu. Glebov, D. D. Meyerhofer, and T. C. Sangster, "Measuring Implosion Dynamics through ρR Evolution in Inertial Confinement Fusion Experiments," to be published in Physical Review Letters.

F. H. Séguin, J. A. Frenje, C. K. Li, D. G. Hicks, S. Kurebayashi, R. D. Petrasso, S. Roberts, J. M. Soures, D. D. Meyerhofer, T. C. Sangster, C. Sorce, V. Yu. Glebov, C. Stoeckl, T. W. Phillips, R. J. Leeper, K. Fletcher, and S. Padalino, "Spectrometry of Charged Particles from Inertial Confinement Fusion Plasmas," to be published in Review of Scientific Instruments.

V. A. Smalyuk, S. B. Dumanis, F. J. Marshall, J. A. Delettrez, D. D. Meyerhofer, T. C. Sangster, and B. Yaakobi, "Radial Structure of Shell Modulations Near Peak Compression of Spherical Implosions," to be published in Physics of Plasmas.

V. A. Smalyuk, P. B. Radha, J. A. Delettrez, V. Yu. Glebov, V. N. Goncharov, D. D. Meyerhofer, S. P. Regan, S. Roberts, T. C. Sangster, J. M. Soures, C. Stoeckl, J. A. Frenje, C. K. Li, R. D. Petrasso, and F. H. Séguin, "Time-Resolved Areal-Density Measurements with Proton Spectroscopy in Spherical Implosions," to be published in Physical Review Letters.

R. Sobolewski, A. Verevkin, G. N. Gol'tsman, A. Lipatov, and K. Wilsher, "Ultrafast Superconducting Single-Photon Optical Detectors and Their Applications," to be published in IEEE Transactions on Applied Superconductivity.

C. Stoeckl, V. Yu. Glebov, S. Roberts, T. C. Sangster, R. A. Lerche, and C. Sorce, "A TIM-Based Neutron Diagnostic for Cryogenic Experiments on OMEGA," to be published in Review of Scientific Instruments.

A. Sunahara, J. A. Delettrez, C. Stoeckl, R. W. Short, and S. Skupsky, "Time-Dependent Electron-Thermal-Flux Inhibition in Direct-Drive Laser Implosion," to be published in Physical Review Letters.

F.-Y. Tsai, T. N. Blanton, D. R. Harding, and S. H. Chen, "Temperature Dependency of the Properties of Vapor-Deposited Polyimide," to be published in the Journal of Applied Physics.

F.-Y. Tsai, D. R. Harding, S. H. Chen, and T. N. Blanton, "High-Permeability Fluorinated Polyimide Microcapsules by Vapor-Deposition Polymerization," to be published in Polymer.

Y. Xu, M. Khafizov, A. Plecenik, P. Kus, L. Satrapinsky, and R. Sobolewski, "Femtosecond Optical Characterization of MgB_2 Superconducting Thin Films," to be published in IEEE Transactions on Applied Superconductivity.

B. Yaakobi, F. J. Marshall, T. R. Boehly, R. P. J. Town, and D. D. Meyerhofer, "Extended X-Ray Absorption Fine Structure Experiments Using a Laser-Imploded Target as a Radiation Source," to be published in the Journal of the Optical Society of America B.

J. Zhang, W. Slysz, A. Verevkin, O. Okunev, G. Chulkova, A. Korneev, A. Lipatov, G. N. Gol'tsman, and R. Sobolewski, "Response-Time Characterization of NbN Superconducting Single-Photon Detectors," to be published in IEEE Transactions on Applied Superconductivity.

X. Zheng, Y. Xu, R. Sobolewski, R. Adam, M. Mikulics, M. Siegel, and P. Kordos, "Femtosecond Response of a Free-standing LT-GaAs Photoconductive Switch," to be published in Applied Optics.

Conference Presentations

R. L. McCrory, D. D. Meyerhofer, S. J. Loucks, S. Skupsky, R. E. Bahr, R. Betti, T. R. Boehly, R. S. Craxton, T. J. B. Collins, J. A. Delettrez, W. R. Donaldson, R. Epstein, J. A. Frenje, V. Yu. Glebov, V. N. Goncharov, D. R. Harding, P. A. Jaanimagi, R. L. Keck, J. H. Kelly, T. J. Kessler, J. P. Knauer, C. K. Li, L. D. Lund, J. A. Marozas, P. W. McKenty, F. J. Marshall, S. F. B. Morse, R. D. Petrasso, P. B. Radha, S. P. Regan, S. Roberts, T. C. Sangster, F. H. Séguin, W. Seka, V. A. Smalyuk, C. Sorce, J. M. Soures, C. Stoeckl, R. P. J. Town, B. Yaakobi, and J. D. Zuegel, "Progress in Direct-Drive Inertial Confinement Fusion Research at the Laboratory for Laser Energetics," 19th IAEA Fusion Energy Conference, Lyon, France, 14–19 October 2002.

The following presentations were made at the 44th Annual Meeting of the APS Division of Plasma Physics, Orlando, FL, 11–15 November 2002:

K. Anderson, R. Betti, T. J. B. Collins, M. M. Marinak, and S. W. Haan, "Adiabat Shaping of ICF Capsules Using Ramped Pressure Profiles."

R. Betti and K. Anderson, "Theory of Laser-Induced Adiabat Shaping in Inertial Fusion Implosions."

T. R. Boehly, T. J. B. Collins, E. Vianello, D. Jacobs-Perkins, D. D. Meyerhofer, G. W. Collins, P. M. Celliers, D. G. Hicks, and R. Cauble, "Deuterium Equation-of-State Experiments on OMEGA."

T. J. B. Collins, S. Skupsky, V. N. Goncharov, R. Betti, P. W. McKenty, and P. B. Radha, "High-Gain, Direct-Drive Foam Target Designs for the National Ignition Facility."

R. S. Craxton, S. P. Regan, J. A. Delettrez, D. D. Meyerhofer, T. C. Sangster, W. Seka, and B. Yaakobi, "Microdot Expansion Trajectories in Long-Scale-Length Plasmas on OMEGA."

J. A. Delettrez, J. P. Knauer, W. Seka, P. A. Jaanimagi, and C. Stoeckl, "Numerical Investigation of Laser Absorption and Drive Experiments of CH Spherical Shells on the OMEGA Laser."

R. Epstein, T. J. B. Collins, J. A. Delettrez, V. N. Goncharov, P. W. McKenty, P. B. Radha, and S. Skupsky, "Modeling of Fuel–Pusher Mix Effects in 1-D Simulations of Cryogenic, All-DT Ignition Capsule Implosions."

J. A. Frenje, C. K. Li, F. H. Séguin, R. D. Petrasso, J. M. Soures, J. A. Delettrez, V. Yu. Glebov, D. D. Meyerhofer, P. B. Radha, T. C. Sangster, C. Stoeckl, N. Hoffmann, and D. Wilson, "Effects of Fuel–Shell Mix on Direct-Drive Implosions of ^{3}He-Gas-Filled, CD-Layered Plastic Capsules on OMEGA."

T. A. Gardiner, L. Guazzotto, R. Betti, and J. Manickam, "Axisymmetric MHD Equilibria with Arbitrary Flow and Applications to NSTX."

V. Yu. Glebov, C. Stoeckl, T. C. Sangster, J. A. Delettrez, P. W. McKenty, and P. B. Radha, "Neutron Burn History Measurements of D_2 Cryogenic Targets on OMEGA."

V. N. Goncharov, "Improved Performance of Direct-Drive ICF Target Designs with Adiabat Shaping Using an Intensity Picket" (invited).

O. V. Gotchev, V. N. Goncharov, P. A. Jaanimagi, J. P. Knauer, and D. D. Meyerhofer, "Experiments on Dynamic Overpressure Stabilization of Ablative Richtmyer–Meshkov Growth in ICF Targets on OMEGA."

L. Guazzotto and R. Betti, "Two-Dimensional MHD Simulations of Tokamak Plasmas with Poloidal Flow."

I. V. Igumenshchev, V. N. Goncharov, P. W. McKenty, and S. Skupsky, "Simulations of Cryogenic Target Implosions on OMEGA."

J. P. Knauer, V. N. Goncharov, P. W. McKenty, T. C. Sangster, R. Betti, V. Yu. Glebov, F. J. Marshall, P. B. Radha, C. Stoeckl, J. A. Frenje, C. K. Li, R. D. Petrasso, and F. H. Séguin, "Improved Performance of Direct-Drive Implosions with a Laser-Shaped Adiabat."

M. V. Kozlov and C. J. McKinstrie, "SBS in Multiple-Species Plasmas."

S. Kurebayashi, J. R. Rygg, B. E. Schwartz, J. DeCiantis, S. Burke, J. A. Frenje, C. K. Li, F. H. Séguin, R. D. Petrasso, V. Yu. Glebov, J. M. Soures, D. D. Meyerhofer, S. Roberts, T. C. Sangster, C. Stoeckl, N. Hoffmann, and D. Wilson, "Stopping Power and Secondary Nuclear Production in OMEGA Implosions."

C. K. Li, F. H. Séguin, J. A. Frenje, S. Kurebayashi, J. R. Rygg, B. E. Schwartz, R. D. Petrasso, R. L. Keck, J. A. Delettrez, P. W. McKenty, F. J. Marshall, D. D. Meyerhofer, P. B. Radha, T. C. Sangster, J. M. Soures, and C. Stoeckl, "Capsule Areal-Density Asymmetries and Time Evolution Inferred from 14.7-MeV Proton Line Structure in OMEGA D^{3}He Implosions" (invited).

J. A. Marozas and P. B. Radha, "A SSD Model for Arbitrary Pulse Shapes Used in the Multidimensional Hydrodynamic Code *DRACO*."

F. J. Marshall, P. W. McKenty, T. J. Kessler, R. Forties, J. H. Kelly, and L. J. Waxer, "Optimized Direct-Drive Uniformity."

A. V. Maximov, J. Myatt, and R. W. Short, "Modeling of Laser–Plasma Interaction Near the Critical Density."

P. W. McKenty, L. M. Elasky, D. R. Harding, F. J. Marshall, D. D. Meyerhofer, P. B. Radha, T. C. Sangster, S. Skupsky, R. L. McCrory, J. A. Frenje, C. K. Li, R. D. Petrasso, and F. H. Séguin, "Numerical Investigation into the Sensitivity of OMEGA Cryogenic Capsule Implosions to Low-Order-Mode Ice Perturbations."

D. D. Meyerhofer, J. A. Delettrez, D. R. Harding, J. D. Kilkenny, S. J. Loucks, R. L. McCrory, P. W. McKenty, S. F. B. Morse, T. C. Sangster, S. Skupsky, and C. Stoeckl, "Direct-Drive Fast-Ignition Research at LLE."

J. Myatt, A. V. Maximov, and R. W. Short, "Realistic Simulations of Stimulated Brillouin Scattering in Long-Scale-Length, Direct-Drive Experiments on OMEGA."

R. D. Petrasso, J. A. Frenje, F. H. Séguin, C. K. Li, B. E. Schwartz, C. Stoeckl, P. B. Radha, J. A. Delettrez, D. D. Meyerhofer, S. Roberts, T. C. Sangster, and J. M. Soures, "Proton and Alpha Core Imaging of OMEGA D^{3}He Implosions."

P. B. Radha, T. J. B. Collins, J. A. Delettrez, R. Epstein, V. Yu. Glebov, V. N. Goncharov, J. A. Marozas, P. W. McKenty, D. D. Meyerhofer, T. C. Sangster, C. Stoeckl, S. Skupsky, J. M. Soures, V. A. Smalyuk, J. A. Frenje, C. K. Li, R. D. Petrasso, F. H. Séguin, and R. P. J. Town, "The Effect of Laser Imprint on Target Performance in Direct-Drive Implosions on OMEGA."

S. P. Regan, J. A. Delettrez, F. J. Marshall, J. M. Soures, V. A. Smalyuk, B. Yaakobi, R. Epstein, V. Yu. Glebov, P. A. Jaanimagi, D. D. Meyerhofer, P. B. Radha, T. C. Sangster, W. Seka, S. Skupsky, C. Stoeckl, D. A. Haynes, Jr., J. A. Frenje, C. K. Li, R. D. Petrasso, and F. H. Séguin, "Experimental Investigation of Fuel–Pusher Mix in Direct-Drive Implosions on OMEGA."

J. R. Rygg, S. Kurebayashi, B. E. Schwartz, J. DeCiantis, S. Burke, J. A. Frenje, C. K. Li, F. H. Séguin, R. D. Petrasso, J. A. Delettrez, V. Yu. Glebov, V. N. Goncharov, D. D. Meyerhofer, P. B. Radha, S. Roberts, T. C. Sangster, J. M. Soures, C. Stoeckl, N. Hoffmann, and D. Wilson, "Time Evolution of OMEGA Direct-Drive D^3He Capsule Implosions Inferred from Charged-Particle Spectra."

T. C. Sangster, J. A. Delettrez, R. Epstein, V. Yu. Glebov, D. R. Harding, J. P. Knauer, R. L. Keck, S. J. Loucks, L. D. Lund, R. L. McCrory, P. W. McKenty, F. J. Marshall, D. D. Meyerhofer, S. F. B. Morse, S. P. Regan, P. B. Radha, S. Roberts, W. Seka, S. Skupsky, V. A. Smalyuk, C. Sorce, J. M. Soures, R. P. J. Town, J. A. Frenje, C. K. Li, R. D. Petrasso, F. H. Séguin, K. A. Fletcher, S. Padalino, C. Freeman, N. Izumi, J. A. Koch, R. A. Lerche, M. J. Moran, T. W. Phillips, and G. J. Schmid, "Direct-Drive Cryogenic Target Implosion Performance on OMEGA" (invited).

B. E. Schwartz, F. H. Séguin, J. A. Frenje, R. D. Petrasso, C. K. Li, P. B. Radha, D. D. Meyerhofer, S. Roberts, T. C. Sangster, J. M. Soures, and C. Culligan, "Proton and Alpha Core Imaging Spectroscopy of Direct-Drive OMEGA Implosions."

F. H. Séguin, R. D. Petrasso, J. A. Frenje, C. K. Li, J. R. Rygg, C. Stoeckl, P. B. Radha, J. A. Delettrez, V. Yu. Glebov, D. D. Meyerhofer, T. C. Sangster, and J. M. Soures, "Time Evolution and Asymmetries of OMEGA Direct-Drive D^3He Capsule Implosions Inferred from 3.0- and 14.7-MeV Protons and 3.6-MeV Alphas."

W. Seka, R. S. Craxton, J. Myatt, A. V. Maximov, D. D. Meyerhofer, S. P. Regan, R. W. Short, A. Simon, C. Stoeckl, R. E. Bahr, and H. Baldis, "SBS in Long-Scale-Length Plasmas for Direct-Drive ICF: Comparing Experiments with Simulations."

R. W. Short, "A Linear Model of Anomalous Stimulated Raman Scattering and Electron Acoustic Waves in Laser-Produced Plasmas."

A. Simon and C. Stoeckl, "A Model of Hot-Electron Signals with Overlapping Pump Beams."

V. A. Smalyuk, J. A. Delettrez, V. Yu. Glebov, V. N. Goncharov, J. P. Knauer, F. J. Marshall, D. D. Meyerhofer, P. B. Radha, S. P. Regan, S. Roberts, T. C. Sangster, S. Skupsky, J. M. Soures, C. Stoeckl, R. P. J. Town, B. Yaakobi, J. A. Frenje, C. K. Li, R. D. Petrasso, F. H. Séguin, D. L. McCrorey, and R. C. Mancini, "Hydrodynamic Growth of Shell Modulations in the Deceleration Phase of Spherical Direct-Drive Implosions" (invited).

J. M. Soures, F. J. Marshall, J. A. Delettrez, V. Yu. Glebov, D. D. Meyerhofer, S. Roberts, T. C. Sangster, J. A. Frenje, C. K. Li, and R. D. Petrasso, "Offset, Direct-Drive, D_2-Filled CH Capsules."

C. Stoeckl, R. E. Bahr, R. S. Craxton, S. P. Regan, W. Seka, and B. Yaakobi, "Multiple-Beam Effects on the Fast-Electron Generation due to the Two-Plasmon-Decay Instability."

B. Yaakobi, T. R. Boehly, F. J. Marshall, D. D. Meyerhofer, R. Epstein, B. A. Remington, and S. M. Pollaine, "EXAFS Detection of Shock-Compressed Titanium."

The following presentations were made at the 6th Workshop on Fast Ignition of Fusion Targets, St. Pete Beach, FL, 16–19 November 2002:

J. A. Delettrez, S. Skupsky, C. Stoeckl, and P. B. Radha, "Transport of Relativistic Electrons for Modeling Fast Ignition in the 2-D Hydrocode *DRACO*."

J. Myatt, A. V. Maximov, and R. W. Short, "Fast Electron Transport in Dense Plasmas in the Context of Fast-Ignition Studies at LLE."

C. Stoeckl, J. A. Delettrez, A. V. Maximov, J. Myatt, P. W. McKenty, S. F. B. Morse, L. J. Waxer, T. C. Sangster, D. D. Meyerhofer, and J. D. Kilkenny, "Integrated Fast-Ignitor Experiments on the Proposed OMEGA EP Facility at LLE."

UNIVERSITY OF
ROCHESTER